PERSISTENT NEUROPATHOGENESIS AND THE ROLE OF MYELOID EXTRACELLULAR VESICLES IN A SHIV.D/MACAQUE MODEL OF HUMAN IMMUNODEFICIENCY VIRUS

A Dissertation
Submitted to
the Temple University Graduate Board

In Partial Fulfillment
of the Requirements for the Degree
DOCTOR OF PHILOSOPHY

---

by
Rachel Podgorski
August 2024

Examining Committee Members:

Tricia Burdo, Advisory Chair, Microbiology, Immunology and Inflammation
Rafal Kaminski, Microbiology, Immunology and Inflammation
Slava Rom, Pathology and Laboratory Medicine
Ilker Sariyer, Microbiology, Immunology and Inflammation
Katharine Bar, External Reader, University of Pennsylvania

ABSTRACT

While the success of combination antiretroviral therapy (ART) has extended the lifespan of people with human immunodeficiency virus (HIV)(PWH), approximately half of PWH on suppressive ART will experience HIV-associated neurological dysfunction. While ART has decreased the incidence of severe neurological disease and dementia in PWH, the incidence of milder neurological and cognitive complications remains stable. Despite the frequency of HIV neurological disease, contributing factors and inflammatory pathogenesis are difficult to observe in PWH over time. Extracellular vesicles (EVs) constitute an understudied method of intercellular communication and molecule delivery in viral infections. EVs carry inflammatory mediators to areas of the periphery during ART suppression but are understudied in the brain. In this dissertation, we use a biologically relevant simian-human immunodeficiency virus (SHIV)-infected non-human primate (NHP) model of HIV persistence in the central nervous system (CNS) to investigate the formation of a myeloid viral reservoir, inflammation during ART-mediated viral suppression, and the roles of myeloid EVs in persistent SHIV neuropathogenesis.

In Chapter 2, we characterized viral and immune persistence in the CNS using SHIV.D, a novel model of HIV-1 in rhesus macaques (RM). Here, we demonstrate viral replication in the brain and neuropathogenesis after ART in RM using novel macrophage-tropic transmitted/founder (TF) SHIV.D.191859. Using quantitative immunohistochemistry (IHC) and DNA/RNAscope, we demonstrated myeloid-mediated neuroinflammation, viral replication, and proviral DNA in the brain in all animals. These findings were replicated in a second cohort of RM necropsied after 6 months of suppressive

ART. We concluded that TF SHIV.D models HIV-1 CNS replication, pathogenesis, and persistence on ART in rhesus macaques, and is a biologically relevant model to study HIV neuropathogenesis.

In Chapter 3, we investigated EVs in a SHIV.D/RM model of HIV. To determine the potential roles of different cell-derived EV populations in SHIV/HIV neuropathogenesis, we developed a method to investigate changes in the cellular origin of EVs *in vivo* in RM. EVs that are released by neural and glial cells into the blood circulatory system can serve as biomarkers for injury and illness as well as give insight into CNS dysfunction and other disease processes in a non-invasive manner. Here, we present a bead-free multiparameter conventional flow cytometry method to phenotype, characterize, and determine cellular origin of plasma extracellular vesicles. Using RM plasma and two four-parameter panels, we identified the following subsets of plasma EVs: tetraspanin CD81+, CD11b+ macrophage-derived, CD14+ monocyte-derived, TMEM119+ microglia-derived, CD171+ neuron-derived, CD3+ T cell-derived, and CD31+ endothelium-derived EVs. EVs were isolated from RM plasma before infection with SHIV.D, during acute viremia, and after ART suppression. EV flow cytometry on these samples revealed a significant increase in TMEM119+ microglial EVs and CD171+ neuronal EVs in RM plasma during viremia and ART suppression.

In Chapter 4, we investigate myeloid-specific EVs in an *in vitro* SHIV.D/RM model. Using primary RM monocyte-derived macrophages (MDM), we determined that MDMs increased EV production after SHIV.D infection. Whole proteomic analysis was conducted on EVs from SHIV-infected and uninfected MDM. Gene ontology pathway

analysis and gene set enrichment analysis reveal pathways associated with overrepresented proteins in myeloid EVs. Finally, differential abundance analysis demonstrated that myeloid EVs isolated from SHIV.D-infected MDMs carried significantly increased levels of neuropathogenic and inflammatory proteins.

Altogether, these studies improve our understanding of SHIV.D viral persistence and persistent neuropathogenesis in the RM brain as a model for HIV-1 chronic neuropathogenesis and describe the contribution of myeloid EVs to neurological disease during SHIV/HIV infection.

ACKNOWLEDGEMENTS

I would first like to thank my mentor, Dr. Tricia Burdo. Both your scientific expertise and encouragement have been instrumental in my development as a confident and independent scientist. The guidance and support you have given me throughout the course of my PhD has been invaluable, and I am grateful for the opportunity to have been your student. I would like to acknowledge my dissertation advisory committee: Dr. Rafal Kaminski, Dr. Slava Rom, and Dr. Ilker Sariyer. Your feedback and advice have made me a better scientist, and I am thankful for all the consideration you have put into my research and training as a scientist. Additionally, I thank our longtime collaborator and my external reader, Dr. Katharine Bar, for your support over the years.

I would also like to acknowledge our collaborators and funding sources. Studies in this dissertation were primarily supported by T32 MH079785 and R01 MH128155 and conducted in collaboration with the Bar laboratory at the University of Pennsylvania, Tulane National Primate Research Center, the LKSOM Flow Cytometry Core Facility, Children's Hospital of Pennsylvania-University of Pennsylvania Proteomics Core, Charles River Laboratories, and Bioqual, Inc.

Next, I would like to thank the current and former Burdo lab members and my colleagues in the Center for NeuroVirology and Gene Editing. In particular, Rebecca Warfield, Jake Robinson, Maurizio Caocci, Maddy Cohen, Stephen Baak, Grayson Sanchez, Tara Gabor, Chelsea Chiappetta, and more. I am grateful to everyone who took the time to teach me new techniques, helped me with experiments, and had fun with me along the way. Among lab members and other members of the PhD program, I have made

lifelong friends at LKSOM, and I'm grateful to have shared this grueling, rewarding, and often silly experience with you all.

Finally, I would like to express my most sincere gratitude to my family and friends. I could never have accomplished this without a lifetime of support from my parents, Carolyn and Ed Podgorski. To my fiancé, Henry - thank you for being my biggest cheerleader, encouraging me always, and celebrating every win with me no matter how small. I also thank my brother Jason, my close friends, my future parents-in-law, my extended family, and my late grandparents. My successes would not have been possible without the support of my those around me along the way.

TABLE OF CONTENTS

LIST OF TABLES

LIST OF FIGURES

LIST OF ABBREVIATIONS

Abbreviation	
AGC	Automatic gain control
AIDS	Acquired immune deficiency syndrome
ALIX	ALG-2 interacting protein X
ANOVA	Analysis of variance
ANXA5	Annexin A5
APC	Allophycocyanin
ART	Antiretroviral therapy
ATI	Analytical treatment interruption
BBB	Blood-brain barrier
BP	Biological process
BR	Broad range
BSA	Bovine serum albumin
BUV	Brilliant ultraviolet
caDNA	Cell-associated DNA
caRNA	Cell-associated RNA
CC	Cellular component
CCL2	C-C chemokine ligand 2 (monocyte chemoattractant protein 1)
CCR5	C-C chemokine receptor 5
sCD14	Soluble CD14
sCD163	Soluble CD163

CM	Cynomolgus macaque
CNS	Central nervous system
CSF	Cerebrospinal fluid
CXCL10	Interferon gamma-induced protein 10
CXCR4	C-X-C chemokine receptor 4
Cy7	Cyanine 7
DAB	3,3'-Diaminobenzidine
DAPI	4',6-diamidino-2-phenylindole
DDA	Data dependent acquisition
dH_2O	Distilled water
DIA	Data independent acquisition
DMEM	Dulbecco's Modified Eagle Medium
DNA	Deoxyribonucleic acid
DPI	Days post-infection
dsDNA	Double-stranded DNA
DTG	Dolutegravir
EDTA	Ethylenediaminetetraacetic acid
EpCAM	Epithelial cellular adhesion molecule
EPF	Endpoint fluorescence
EV	Extracellular vesicle
FACS	Fluorescence-activated cell sorting
FBS	Fetal bovine serum

FC	Fold change
FFPE	Formalin-fixed paraffin-embedded
FLOT1	Flotillin 1
FMO	Fluorescence minus one
FSC	Forward scatter
FTC	Emtricitabine
G(3)	Ghost(3) reporter cells
GFAP	Glial fibrillary acidic protein
GFP	Green fluorescent protein
GM130	Golgi matrix protein 130
GO	Gene ontology
gp120	Glycoprotein 120
gp41	Glycoprotein 41
GSEA	Gene set enrichment analysis
HIV	Human immunodeficiency virus
HMGN3	High mobility nucleosome-binding domain-containing protein 3
HPLC	High performance liquid chromatography
HRP	Horseradish peroxidase
IBA1	Ionized calcium binding adaptor molecule 1
ICAM1	Intercellular adhesion molecule 1
ICC	Immunocytochemistry
IDO1	Indoleamine 2,3-dioxygenase 1

IDT	Integrated DNA Technologies
IGFB1	Insulin-like growth factor binding protein 1
IHC	Immunohistochemistry
IPDA	Intact proviral DNA assay
iRT	Indexed retention time
ISH	*In situ* hybridization
LC	Liquid chromatography
LCN2	Lipocalin-2
LOQ	Limit of quantification
L1CAM	L1 cell adhesion molecule
M-CSF	Macrophage colony stimulating factor
MDM	Monocyte-derived macrophage
MEV	Macrophage extracellular vesicle
MF	Molecular function
MFI	Mean fluorescence intensity
miRNA	MicroRNA
MOI	Multiplicity of infection
MS	Mass spectrometry
NBL1	Neuroblastoma suppressor of tumorigenicity 1
NEB	New England Biolabs
NFL	Neurofilament light chain
NHP	Non-human primate

NHPRR	Non-human Primate Reagent Resource
NNRTI	Non-nucleoside reverse transcriptase inhibitor
NRTI	Nucleoside reverse transcriptase inhibitor
NTA	Nanoparticle tracking analysis
PBMC	Peripheral blood mononuclear cell
PBS	Phosphate-buffered saline
PBST	PBS + 0.1%-0.05% Tween-20
PCA	Principal component analysis
PCR	Polymerase chain reaction
PE	Phycoerythrin
PEV	Plasma extracellular vesicle
PFA	Paraformaldehyde
PWH	People with HIV
PM	Pigtailed macaque
PMT	Photomultiplier tube
PNS	Peripheral nervous system
qPCR	Quantitative polymerase chain reaction
QA	Quality analysis
QC	Quality control
QVOA	Quantitative viral outgrowth assay
RM	Rhesus macaque
RNA	Ribonucleic acid

ROS	Reactive oxygen species
RP	Reverse phase
RPM	Revolutions per minute
RPMI	Roswell Park Memorial Institute medium
RSLC	Rapid separation liquid chromatography
RT	Room temperature
RT-qPCR	Reverse transcription quantitative polymerase chain reaction
SBI	System Biosciences
SDS	Sodium dodecyl sulfate
SSC	Side scatter
SE	Spectral enabled
SHIV	Simian-human immunodeficiency virus
SHIV.D	SHIV clade D transmitted/founder variant 191859
SIV	Simian immunodeficiency virus
SIVE	SIV encephalitis
TC	Tissue culture
TCEP	Tris(2-carboxyethyl)phosphine
TDF	Tenofovir disoproxil fumarate
TEAB	Tetraethylammonium bromide
TERT	Telomerase reverse transcriptase
TF	Transmitted/founder
TFA	Trifluoroacetic acid

TIMD4	T cell immunoglobulin and mucin domain containing 4
TMEM119	Transmembrane protein 119
TNF-α	Tumor necrosis factor alpha
TNPRC	Tulane National Primate Research Center
TSG101	Tumor susceptibility gene 101
UPLC	Ultra performance liquid chromatography
VL	Viral load
vRNA	Viral RNA
WPI	Weeks post infection

CHAPTER 1

REVIEW OF THE LITERATURE

Human Immunodeficiency Virus

Human immunodeficiency virus (HIV) is a dual single-stranded ribonucleic acid (RNA) retrovirus specific to humans (1). The two types, HIV-1 and HIV-2, evolved separately from different clades of simian immunodeficiency virus (SIV) affecting chimpanzees and sooty mangabeys, respectively (2). Of the subspecies, HIV-1 is more virulent and responsible for over 95% of HIV infection worldwide (3). HIV-1 can be further divided into groups M, N, O, and P, of which M has the highest global prevalence (3). From group M, HIV-1 is divided into clades. Each clade is distinct in both geographic distribution and frequency of HIV clinical manifestations and HIV-associated comorbidities (4,5). HIV-1 M clade B is the most common HIV subtype in the Americas, and clade D is most frequently associated with neurocognitive decline (4,5).

Each HIV virion encodes genes for accessory proteins and three structural polyproteins: *gag,* which encodes the capsid, nucleocapsid, and matrix proteins; *pol*, which encodes genes for the enzymes reverse transcriptase, integrase, and protease; and *env*, from which the envelope glycoproteins are derived (1). Envelope glycoprotein gp120 binds to CD4 on the host cell, which initiates HIV's cellular entry. Inside the cell, HIV reverse transcriptase transcribes its single-stranded RNA into deoxyribonucleic acid (DNA), which is transported inside the nucleus and then integrated into the host cell's genome as provirus (1). Replication-competent provirus integrated into long-lived cell types in the host form

the latent viral reservoir in antiretroviral therapy (ART)-suppressed people with HIV (PWH) (6).

Neurological Manifestations and Neuropathology of HIV in the ART Era

Since the approval of the first antiretroviral drug for HIV in 1987, combination ART, global ART coverage, and ART adherence have improved sharply. As of 2020, 87% of PWH worldwide who know their status are accessing ART (7). Of these people, 90% have suppressed viral loads (7). Subsequently, the incidence of severe neurological disease such as HIV-associated dementia and HIV encephalitis have decreased significantly (8–10). However, PWH on long-term ART continue to develop neurological complications of HIV despite suppressed plasma viral loads (8–11). The reported incidence of HIV-associated neurological dysfunction in PWH on suppressive ART varies between 30-70% (11–17). Neurological and cognitive symptoms found in ART-treated PWH include impairment of executive function, memory, and motor skills, mood disorders, neuropathic pain, tremors, and seizures (18–21). One retrospective cohort study identified distal sensory neuropathy and neurocognitive dysfunction as the most prevalent HIV-associated neurological disorders among ART-treated PWH (22).

HIV-1 pathogenesis the central nervous system (CNS) is driven by infection of myeloid lineage cells (23,24). HIV-1 seeding of the CNS is mediated by the transmigration of infected macrophages, CD14+/CD16+ monocytes, and CD4+ T lymphocytes across the blood-brain barrier (24–28). Resident CNS macrophages and microglia are susceptible to HIV infection and harbor proviral DNA and low levels of replicating viral RNA during ART-induced plasma viral suppression (27,28). These long-lived myeloid cell types form

the viral reservoir in the CNS, which persists during ART suppression and can rebound into active viral replication if treatment is interrupted (29).

Though many PWH experience neurological dysfunction, their specific symptoms and disease processes that lead to neurological or cognitive decline often vary. The most severe neurological complications of HIV, macrophage-mediated encephalitis and HIV-associated dementia, are rarely found in PWH now, but sometimes in PWH experiencing ART interruption or non-adherence (8,19,20). Macrophage-mediated HIV encephalitis is characterized by plasma and cerebrospinal fluid (CSF) viremia, macrophage infiltration into the CNS, the presence of multinucleated giant cells, and elevated markers of neuropathology and myeloid cell activation including neurofilament light chain (NFL), sCD14, neopterin, TNF-α, CCL2, and sCD163 in the CSF and plasma (19,20,30,31). In ART-adherent PWH with low CD4+ T cell nadir before ART initiation or opportunistic co-infections, T cell-mediated encephalitis is a prevalent complication (20). T cell-mediated encephalitis can be driven by CD4+, CD8+, or a combination of both T cell types infiltrating the perivascular space or parenchyma (19,20). In this clinical phenotype, neurological dysfunction is sometimes the result of lymphocyte-driven immune hyperactivation following ART initiation (20,32–34). A CNS viral escape phenotype is most often associated with PWH who are ART-treated with imperfect adherence, have a drug-resistant virus, or take ART with poor CNS penetration (20). CNS viral escape, characterized by elevated viral load (VL) in the CSF but not plasma, presents with varied neurological symptoms, including sensory neuropathies, neurocognitive decline, and seizures (20). In symptomatic CSF viral escape, high CSF neopterin, white blood cells,

NFL, and CD14+/CD16+ inflammatory monocytes are common (19). In asymptomatic or pre-symptomatic CSF viral escape, elevated CXCL10 is often found in the plasma and CSF (19). HIV protein-associated encephalopathy is found in PWH who are ART-adherent with undetectable viral loads in both the CSF and plasma (20). In this disease phenotype, the continuous translation of integrated viral protein genes perpetuates neuroinflammation and increased cell death in virally suppressed PWH. Neuronal loss, amyloid-beta accumulation, and Tau deposits are also common (20). The heterogeneity of neuroHIV disease mechanisms and phenotypes necessitate further research. Biologically relevant animal models that recapitulate the diverse neurological outcomes of ART-controlled HIV CNS infection are critical to understanding its pathology and reservoir dynamics and the development and evaluation of curative strategies.

Non-human Primate Models for HIV Research

The prototypical and most widely used animal models for HIV research are SIV infection models of NHP. SIV is an ancient and ubiquitous retrovirus of African NHP including chimpanzees, macaques, sooty mangabeys, and drills (35,36). As SIV is a precursor virus of HIV, they share nearly identical genome structures (2). Like HIV, SIV is a retrovirus which encodes the three essential polyproteins *gag, pol,* and *env* as well as accessory proteins (37). SIV provirus also integrates into the host cell's genome, forming a viral reservoir (37). In their natural hosts, SIVs rarely cause disease (35,38). However, some SIV clones can cause acquired immunodeficiency syndrome (AIDS)-like disease in NHP other than the virus's native host species (39,40). Pathogenic macaque SIV strains SIVmac251 and SIVmac239 were first isolated from rhesus macaques *(Macaca mulatta)*

at the New England Regional Primate Research Center in 1985 (41). When experimentally infected with clones of SIVmac239, rhesus macaques (RM) exhibit significant plasma viremia, loss of CD4+ T lymphocytes, and typically develop AIDS-like disease within one to two years (35,39). SIVmac251 causes similar pathogenesis, with most intravenously infected RM developing severe diseases including muscle wasting and contracting opportunistic infections within one year (39,42). SIVmac239/251 also causes HIV-1-like pathogenesis in other Old World monkey species, including cynomolgus macaques (CM, *Macaca fascicularis*) and pigtailed macaques (PM, *Macaca nemestrina*) (43–45). To date, RM continue to be the most widely used NHP model species for HIV research (46–49). SIV viruses in all common NHP model species are suppressible with combination ART (50). Today, the most frequently used ART drugs in NHP studies are integrase inhibitor dolutegravir (DTG) and nucleoside reverse transcriptase inhibitors (NRTI) tenofovir disoproxil fumarate (TDF) and emtricitabine (FTC) (51,52). This cocktail matches the first line treatment guidelines for PWH, which consists of two NRTIs and an integrase inhibitor (53).

SIVmac239 and 251 utilize the CD4 cellular receptor and C-C chemokine receptor 5 (CCR5) co-receptor, and are able to infect and replicate *in vitro* in RM CD4+/CCR5+ cells (54–56). However, SIVmac239 is primarily lymphocyte-tropic, while SIVmac251 is able to productively replicate in both macrophages and lymphocytes (57–60). Because the majority of HIV-1 neuropathogenesis is mediated my myeloid lineage cells, a virus's ability to enter and replicate efficiently in macrophages and other myeloid cells is critical for a CNS-tropic NHP model of HIV disease (23,24,27,28). While many SIV viral clones

and isolates are used for HIV modeling in NHP, fewer demonstrate biologically accurate and reproducible neurotropism and can be used as models for HIV neuropathogenesis.

SIV and SHIV Models of HIV Central Nervous System Disease

Due to its pathogenicity in RM, myeloid tropism, and response to ART, the SIVmac251/RM model is often used to investigate HIV neuropathogenesis and neurological dysfunction (Table 1.1) (41,61–63). CD8+ T cell depletion is often performed in conjunction with SIVmac251 infection, as this results in more rapid progression of SIV encephalitis (SIVE) with high incidence and degree of peripheral neuropathy (64,65). In some cases, serial passage of SIVmac239 through RM results in neurovirulent infection. The viral clones isolated from these RM, such as SIVmac239-R17 and -17E, were often used in early models of HIV CNS disease (Table 1.1) (66–68).

To model the co-occurrence of immunosuppression and HIV neuroinvasion often seen in PWH who progress to AIDS, a dual-SIV infection model using both an immunosuppressive derivative of SIVmac17E and neurovirulent SIV ΔB67 in PM was developed (Table 1.1) (69). This model led to rapid onset encephalitis with CNS lesions, macrophage and lymphocyte infiltration, multinucleated giant cell formation, and CSF viremia in RM (69). When treated with suppressive ART, PM experience signs of immune hyperactivation, T-cell mediated encephalitis, and periodic CSF viral escape with persistent peripheral nervous system (PNS) damage (70–72).

Table 1.1. Neurotropic SIV/SHIVs frequently used for neuroHIV modeling.

Virus	HIV-1 M clade	Tropism	NHP model species	Virus properties or construction	CNS involvement
SIVmac239 R71/17E	N/A	Dual	RM	Serially passaged SIVmac239 isolated from RM experiencing neurological disease (66).	Microglial activation, neuron loss, some SIV encephalitis (67,68).
SIVmac251	N/A	Dual	CM, PM, RM	Isolated from symptomatic RM (41). Often used in conjunction with CD8+ depletion.	Replicates in RM brain and causes gliosis, perivascular infiltration, and glial nodules during early infection (61). Some low-level viral replication and viral DNA in the brain in ART suppressed RM (62,63).
SIVmac17E + SIV ΔB67	N/A	Dual	PM	SIVmac17E-Fr: neurovirulent SIVmac17E-Br *env, nef,* 3' LTR, SIVmac239 backbone; SIV ΔB67: primary RM isolate (69).	Lymphocyte-dominant encephalitis and episodic CSF viral rebound during ART, persistent PNS damage (70,72).
SIVsm804E-CL757	N/A	Dual	RM	SIVsm804E clone isolated from brain of RM with neuroAIDS (73).	Slower progression of CNS disease typical of HIV progression, parenchymal macrophage infection, CD4+ T cell infiltration (74).
SHIV KU-1/2	B	CXCR4	RM	HIV-1 *env, tat, rev, vpu,* SIVmac239 backbone (75).	Demyelinating lesions, syncytia, viral replication in the brain, some gradual encephalitis, tremors (76,77)

Table 1.1. Continued.

Virus	HIV-1 M clade	Tropism	NHP model species	Virus properties or construction	CNS involvement
SHIV-1157ipd3N4	C	CCR5	RM	HIV-1 *env* isolated from a PWH, SIVmac239 backbone with additional NF-κB binding site to increase replication capacity, serially passaged through RM (78).	Nonaccelerated T cell-mediated inflammation and infection in the CNS and meninges without microglial activation or myeloid infiltrate in viremic RM (79).
SHIV SF162P3	B	CCR5, but demonstrates CXCR4 co-receptor switch *in vivo*	RM	HIV-1 *env, tat, rev* isolated from a PWH experiencing neurological disease, SIVmac239 backbone, serially passaged through RM.	Macrophage-mediated lesions, myeloid cell infiltration and syncytia formation, encephalitis (80).
SHIV.C.CH505	C	CCR5	RM	TF HIV-1 *env* with mutated residue 375 for enhanced CD4 binding, SIVmac766 backbone (81).	Early viral integration in brain regions associated with cognition and motor function, upregulation of neuroinflammatory gene transcripts (82).

Note. SIV and SHIV viruses that reproducibly infect the brain and result in neuropathogenesis in different macaque species are listed, along with each model virus's clade (SHIV only), co-receptor usage, NHP species, viral properties, construction, and CNS involvement. ART: antiretroviral therapy, CM: cynomolgus macaque (*Macaca fascicularis*), CNS: central nervous system, CSF: cerebrospinal fluid, HIV: Human Immunodeficiency Virus, NHP: nonhuman primate, PWH: people with HIV, PM: pigtailed macaque (*Macaca nemestrina*), PNS: peripheral nervous system, RM: rhesus macaque (*Macaca mulatta*), SHIV: simian-human immunodeficiency virus, SIV: simian immunodeficiency virus, TF: transmitted/founder.

Recently, slow-progression SIV models that represent chronic, ART-treated HIV pathogenesis in the brain have become more prevalent (Table 1.1). SIVsm804E-CL757, a clone of SIVsm804E isolated from the brain of a macaque with simian AIDS, demonstrates gradual progression of CNS disease in RM frequently leading to encephalitis (73). SIVsm804E-CL757 replicates in parenchymal macrophages and causes CD4+ T cell infiltration to sites of infection in the CNS (74).

Chimeric simian-human immunodeficiency viruses (SHIVs) are engineered viruses in which an HIV gene replaces an equivalent SIV gene. SHIV-based models have been used since 1992 to investigate HIV pathogenesis and evaluate drug targets and potential treatment strategies in NHP (83). In most SHIVs, the HIV *env* gene, which encodes envelope surface glycoproteins gp120 and gp41, replaces SIV *env* for use in glycoprotein-targeting vaccine trials and neutralizing antibody studies (83,84). SHIV KU-1, a CXCR4-tropic first-generation SHIV used for CNS pathogenesis study, is neurovirulent in Chinese RM, causing macrophage-mediated lesions, syncytia formation, and gradual encephalitis (Table 1.1) (77,85). A serially passaged derivative, SHIV KU-2, demonstrates demyelinating lesions, syncytia formation, and tremors in some RM (75,76,84,86,87). Other early SHIVs include R5 clade C SHIV-1157ipd3N4, which causes nonaccelerated neuroinflammation in RM, and R5 clade B SHIV SF162P3, which demonstrates CXCR4 co-receptor switch and macrophage-mediated encephalitis in ART-naive RM (78–80).

However, limitations of early SHIVs hindered their ability to reproducibly model HIV-1 and its neuropathogenesis in NHP. Early SHIV/RM models exhibited deficient autologous tier 2 antibody responses, low viral set points, and limited chronic phase

replication and pathogenesis (84,88–90). Additionally, many SHIV/NHP models developed specific CXCR4 tropism, leading to rapid depletion of CXCR4+/CCR5- naïve T cells (81,84,90). Newer SHIV/NHP models have improved upon these issues. Recently developed SHIVs can maintain CCR5 tropism, consistently induce autologous antibody response, and recapitulate the immunopathogenesis and early viral kinetics of HIV-1 (84,89). Transmitted/founder (TF) SHIVs with modified *env* residue 375, part of the CD4 binding domain, have been further shown to reliably model HIV-1 infection, CNS persistence, and latency in RM while maintaining TF viral dynamics and replication fitness (81,82,84,89,91,92). SHIV.C.CH505, which contains a TF clade C HIV-1 *env* with a modified *env*375, was shown to integrate into brain regions associated with cognition and motor function during acute infection in RM and exhibit increased transcription of genes associated with neuroinflammation (82).

SHIV.D as a Model of HIV CNS Persistence

SHIV.D.191859 is a TF virus with an *env* gene identified from an acutely infected Ugandan woman in 2008. The isolated clade D HIV-1 virus is CCR5-tropic, with the ability to replicate in both CD4+ T cells and macrophages (93). SHIV.D.191859 encodes this HIV-1 *env* within a SIVmac766 backbone, with the substitution of a bulky, hydrophobic residue at *env* position 375, part of the CD4 binding domain, to enhance binding to rhesus CD4 molecules and replication in RM cells (Figure 1.1) (81). SHIV.D.191859 recapitulates many features of HIV-1 pathogenesis, including mucosal and intravenous transmission, consistent viral kinetics, and CD4 depletion over time (81,84).

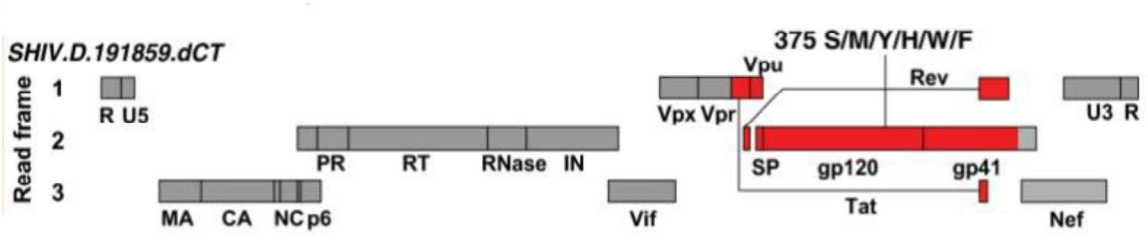

Figure 1.1. SHIV.D.191859 construction. HIV-1 D.191859 gp160 (*tat, rev, vpu, env* [red]) with exchanged Methionine/Tyrosine/Histidine/Tryptophan/Phenylalanine at residue 375 replaces the equivalent region in a SIVmac766 backbone (grey).

Historically, infection with clade D HIV is associated with more severe neuropathogenesis and higher prevalence of HIV-associated neurocognitive decline than clades B, C and A, all of which have published information on their relationship to HIV-associated neurocognitive disorders (4,94). The desirable viral kinetics and macrophage tropism of this SHIV, and the reported neuropathogenesis of clade D HIV-1 (93,95), provide unique opportunities for TF SHIV.D.191859 as a neuropathogenic NHP model.

Previous research evaluated SHIV.D.191859 for its potential to model HIV-1 for latency in the periphery (89). Six RMs were infected with SHIV.D, treated with suppressive ART (tenofovir DF, emtricitabine, dolutegravir) for 24 weeks, and subjected to analytical treatment interruption (ATI) (89). Quantification of cellular viral RNA (caRNA) and cell-associated proviral DNA (caDNA) from PBMCs during chronic infection and at several post-ART timepoints revealed stable levels of caDNA pre- and post-ART, as well as caRNA, rebound to pre-ART levels after ATI (89). CD4+ T cell quantification revealed depletion in unsuppressed animals (89). In comparison to SIVmac239 infection of RMs, the lower levels of viremia during peak and early infection characteristic of SHIV.D infection better models HIV-1 in humans (89). The vast majority

of SHIV.D-infected RMs achieved viral suppression with ART in two to four weeks (89). This is advantageous over chronic SIVmac239 infection, which often takes many months to achieve suppression on ART (89). Importantly, SHIV.D maintains CCR5 tropism, which is associated with the progression of AIDS-like disease in RMs (81,89). These characteristics make SHIV.D a promising candidate virus for an NHP model of HIV that forms a viral reservoir in the brain that persists and causes chronic neuropathogenesis during ART-mediated viral suppression.

Due to the multifactorial and etiologically complex nature of HIV neurological dysfunction, animal models of the CNS complications seen in HIV are preferred over *ex vivo* and *in vitro* research alone. NHP models that accurately represent different manifestations of HIV CNS complications are critical for research on curative strategies, therapeutics, and prevention of severe neuropathology. As ART drugs and global adherence continue to improve, long-term ART NHP models of HIV are critical to advance research on HIV CNS dysfunction as a chronic disease. SIV and SHIV encephalitis models are frequently accurate representations of ART-untreated macrophage-mediated HIV encephalitis, but fewer models represent the immune and pathological signatures of modern ART-treated mild CNS pathogenesis. As research on neurological manifestations of ART-treated HIV continues, development of chronic SIV/SHIV CNS models and characterization of existing neurotropic models under long-term ART is imperative to advance our understanding of the CNS viral reservoir and neurological comorbidities.

Extracellular Vesicles: Biogenesis, Characteristics, and Uptake

Extracellular vesicles (EVs) are membrane-bound nanoparticles released by all cell types (96). Exosomes, microvesicles, and apoptotic bodies are the three general categories of EVs, classified by their size and mode of release (97–99). Exosomes are smaller EVs approximately 50-200nm, formed from the inward budding of multivesicular bodies from endosomal membranes after fusion with the cells' plasma membrane (97,100). While microvesicles are typically larger EVs, their size can range widely from 50nm-1000nm (96,98). Microvesicles are formed by outward budding of the cell's plasma membrane (98). Apoptotic bodies, are the largest variety at 1000-5000nm in diameter, formed by membrane blebbing during programmed cell death (99,101). Classical markers of endosome-derived exosomes include tetraspanins CD9, CD81 and CD63 as well as heat shock proteins, flotillin-1 (FLOT1) tumor susceptibility gene 101 (TSG101) and ALG-2 interacting protein X (ALIX) (100,102,103). While the biogenesis of microvesicles differs from that of traditional exosomes, they too possess tetraspanins and are enriched for many of the same proteins, such as TSG101, from plasma membrane budding (100,103–105). Although apoptotic bodies also form from the plasma membrane, they are significantly larger than exosomes and small microvesicles and generally lack tetraspanins and other classical EV markers (99,106). Unlike exosomes and microvesicles, apoptotic bodies contain organelles and other cellular components, making their proteomic profile indistinguishable from cell lysate (105). Due to their similarities in size, cargo, enriched proteins, tetraspanins and other membrane markers, it is impossible to differentiate exosomes and small

microvesicles in EV preparations (102). Therefore, it is most accurate to refer to all circulating sub-micron, tetraspanin-positive, membrane-bound nanoparticles as EVs.

As membrane protein-expressing vesicles, EVs are important players in intercellular communication. EV cargo can contain proteins, lipids, and nucleic acids (DNA fragments, messenger RNA, microRNA, and non-coding RNA) (102,103,107). When cells produce EVs, they are released into the extracellular space. EVs can be found in all bodily fluids and be circulated through the body (99,107). They have also been demonstrated to cross the CNS blood-brain barrier (BBB) (108). Intercellular signaling through EVs can occur through multiple biological processes. EVs can communicate phenotype-changing information to target cells through interactions at the cell surface, without internalization of the vesicles or internal delivery of their cargo (109). There is evidence that recipient cells can take up heterogenous EVs through a variety of mechanisms, including macropinocytosis, phagocytosis, membrane fusion, lipid raft mediated endocytosis, and receptor-ligand mediated endocytosis (110). Following uptake, EVs co-localize with receptor cell endosomes and lysosomes, and most likely release their cargo into the cytosol through EV membrane degradation mediated by fusion with the endosome or lysosome (110–112). Some research demonstrates that EVs can interact with specific cell types. One study exposing urologic cancer cell-derived EVs to cancerous and noncancerous cells of different tissue types resulted in more efficient EV update by cancerous cells (113). Another study demonstrated that EVs produced by cortical neurons after synapse activation were endocytosed exclusively by neurons, and did not interact with glial cells (114). Due to their ability to retain membrane proteins and cargo from their cell

of origin, dissemination throughout the body, and specific nature of intercellular signaling, EVs are a valuable source of cellular information as biomarkers or effectors of physiological and pathological processes *in vivo.*

EVs in CNS Disease and HIV

EVs play important roles in the biology and pathology of many different diseases. The roles of EVs in the pathogenesis of CNS disease have been of particular interest due to the persistent and complex causative nature of neurodegeneration and neuroinflammation. Brain-derived EVs are also found in the blood and CSF, providing a window into ongoing neuropathological processes in patients and animal models of diseases over time. Early exosome research found that pathogenic misfolded prion proteins can be packaged into EVs, and these EVs can propagate prion disease in a naïve animal host (115,116). Soon after, it was discovered that EVs serve as both a mediator of pathogenesis in Alzheimer's disease as well as a biomarker of early disease (117,118). EVs containing amyloid-β, amyloid precursor protein, and tau transport these proteins across the brain and initiate new accumulations (117,119,120). In addition to perpetuating pathogenesis, brain-derived EVs in the CSF and plasma are also valuable biomarkers for early Alzheimer's disease (118,121–123). To date, EVs have been characterized as mediators of pathogenesis and sources of biomarkers in several other neurodegenerative diseases, including Parkinson's disease, Huntington's disease, and amyotrophic lateral sclerosis, though many of their mechanisms of pathogenesis have yet to be discovered (124,125).

Recently, the functions of EVs in HIV pathogenesis have been explored. EVs have a unique relationship with viral infections, as viruses can co-opt EV biogenesis pathways for virion production in the host cell, mimicking intra- and intercellular trafficking and communication (126,127). In HIV infection, the virus hijacks the host's exosome production machinery, the Endosomal Sorting Complex Required for Transport (ESCRT) pathway, for virion budding (127–129) The functions and utility of EVs are of particular interest in the neurological pathogenesis of HIV. Some EVs have been identified as drivers of neuropathogenesis during HIV infection. Astrocyte-derived EVs containing HIV *nef* are taken up by neurons in a co-culture model, decreasing neuronal action potentials (130). EVs from HIV-infected macrophages transport viral particles and inflammatory cytokines to nearby uninfected cells (131,132). Proteomic profiling of EV cargo from ART-suppressed PWH reveal an upregulation of inflammatory interferon-gamma and interleukin 1-α (133). Targeted protein analysis of plasma neuron-derived EV cargo demonstrate differential expression of several proteins between PWH with and without cognitive impairment (122,134,135). These genes that are upregulated in PWH experiencing cognitive impairment are of note as potential biomarkers. A mass spectrometry study comparing CSF EV cargo from PWH with and without cognitive impairment found higher abundance of genes associated with stress response and inflammation by gene ontology in PWH experiencing neurological symptoms (136). In addition to viral and host proteins, EVs from HIV-infected cells contain significantly different microRNA (miRNA) profiles (132). EVs isolated from HIV-infected macrophages *in vitro* have several differentially upregulated miRNAs compared to their

uninfected counterparts, including pro-inflammatory miR-29a (137). In a study profiling EV-associated miRNAs from ART-naïve PWH, two miRNAs associated with inflammatory pathogenesis were identified (138). Lastly, multiple studies have demonstrated an increase in cellular TNF-α production *in vitro* after treatment with EVs from HIV-infected cells (139–141).

There is a strong connection between EVs and inflammation in the context of HIV infection, but cell-specific EV production and host protein cargo over the course of a NHP model of HIV infection has not been explored. Investigating circulating EVs in a NHP model of ART-suppressed HIV provides the unique opportunity to study changes in EV populations and their cargo in RM before infection and throughout viremia and ART viral suppression.

Hypothesis and Specific Aims

In summary, HIV neurological dysfunction and cognitive decline persist in 50% of PWH on ART. A modern biologically and clinically relevant animal model of ART-treated HIV in the brain is necessary to elucidate the persistent neuropathogenesis that occurs during ART suppression. Novel TF SHIV.D accurately models HIV-1 transmission dynamics in RM, consistent CCR5 tropism, and persistence during ART suppression, showing promise as a potential model of HIV neurological persistence. Finally, EVs have been demonstrated to promote pathologic changes and neuroinflammation during CNS injury and disease states. Brain-derived EVs can cross the BBB into the peripheral blood and can be investigated longitudinally over time in an animal model of HIV neurological persistence. Therefore, we **hypothesize** that SHIV.D forms a brain reservoir and causes

persistent neuropathogenesis in rhesus macaques, which is mediated by myeloid-derived extracellular vesicles. This hypothesis is tested in the following two aims.

Specific Aim 1: Examine the persistence of the myeloid reservoir in the brain and its associated neuropathogenesis using TF SHIV.D in rhesus macaques. This aim was accomplished by two objectives: 1) Utilize quantitative immunohistochemistry (IHC) and *in situ* hybridization (ISH) to detect and quantify replicating viral RNA, proviral DNA, and myeloid and lymphoid cell markers in the brain, and 2) Determine CNS cell types containing replicating and latent virus using multi-target IHC/ISH co-staining.

Specific Aim 2: Examine changes in myeloid-derived extracellular vesicle production and cargo during SHIV.D infection and ART-mediated viral suppression. This aim was accomplished by three objectives: 1) Isolate EVs from SHIV.D infected myeloid cells *in vitro* and SHIV.D infected RM plasma to compare differences in size and concentration, 2) Develop a cellular antigen EV flow cytometry method to determine differential cell-specific EV production before infection, during acute viremia, and during ART suppression, and 3) Utilize whole proteome profiling to analyze differences in EV cargo from SHIV.D infected and uninfected myeloid cells.

CHAPTER 2

TRANSMITTED/FOUNDER SHIV.D REPLICATES IN THE BRAIN, CAUSES NEUROPATHOGENESIS, AND PERSISTS ON COMBINATION ANTIRETROVIRAL THERAPY IN RHESUS MACAQUES

Adapted from Podgorski et al, Retrovirology. 2023 Aug 10;20(1):13. DOI: 10.1186/s12977-023-00628-5. (92).

Chapter Abstract

Long-lived myeloid cell types play a critical role in HIV-1 latency and cellular dysfunction even during ART suppression (142–145). However, HIV persistence and reservoirs in the CNS remain understudied. SIV/ SHIV infection of NHP is a biologically relevant model to investigate HIV-1 persistence in the CNS, but the rapid pathogenic progression of previous SIV and SHIV viruses has limitations in modeling HIV-1 (46,146). Earlier studies utilizing SHIV/NHP model systems in the CNS were focused on SHIV/HIV encephalitis and did not investigate the persistent effects of SHIV infection in the CNS through ART suppression (75,79,147–149). Furthermore, earlier models did not include TF HIV-1 envelope-containing viruses. To better understand the chronic progression of HIV-1 neuropathogenesis on suppressive ART, a non-encephalitic CNS infection NHP model is necessary (88). Here, we characterize the neuropathogenesis of macrophage-tropic TF SHIV.D.191859 infection in RM to elucidate the dynamics of HIV pathogenesis and persistence in the brain during ART. Quantitative immunohistochemistry (IHC) and DNA/RNAscope in situ hybridization (ISH) were performed on three brain regions from six SHIV.D-infected RMs; two necropsied while viremic, two during analytical treatment

interruptions, and two on suppressive ART. We demonstrated myeloid-mediated neuroinflammation, viral replication, and proviral DNA in the brain in all animals. These results demonstrate that TF SHIV.D models native HIV-1 CNS replication, pathogenesis, and persistence on ART in rhesus macaques.

Materials and Methods

Non-Human Primates and Ethics

Archived tissue samples from female RM infected with SHIV.D (Figure 1.1) were obtained from the Tulane National Primate Research Center (TNPRC) and the University of Pennsylvania. Additional brain tissue samples from male RM infected with SHIV.D were obtained from Bioqual, Inc. (Rockville, MD). All RM were maintained in accordance with the rules and regulations of the Committee on the Care and Use of Laboratory Animal Resources. All experiments were approved by the Tulane/Bioqual Animal Care and Use Committee. Monkeys were housed in pairs to promote the psychological well-being of non-human primates. Enrichment included manipulable items in the cages (durable and destructible objects), perches or swings, various food supplements (fruit, vegetables, primate treats), foraging or task-oriented feeding methods and human interaction with caretakers and research staff as dictated by The United States Animal Welfare Act. Enrichment devices are rotated on a weekly basis and include toys, mirrors, radios, TV/VCRs, foraging boards, and a variety of complex foraging devices. Animals were fed a normal monkey chow. Animal care staff monitored the health and well-being of the animals daily with physical examinations performed weekly. All possible measures were taken to minimize discomfort of the animals. Anesthesia and analgesics were used and

administered under the direction of a licensed veterinarian. All procedures were performed under ketamine or telazol anesthesia. Analgesics such as buprenorphine and lidocaine were used preemptively and following each potentially painful procedure. All animals were sacrificed according to humane endpoints consistent with the recommendations of the American Veterinary Medical Association (AVMA) Guidelines for the Euthanasia of Animals.

In the study from which RM were retrospectively investigated, the protocol was for animals to be challenged intravaginally, then if not productively infected after 4 attempts, to be challenged intravenously. Thus, RM from the same protocol were infected with SHIV.D vaginally (4) and intravenously (2). As described (81), plasma viral kinetics and reservoir dynamics were similar despite the challenge route. RMs were maintained at TNPRC according to the Association for Assessment and Accreditation of Laboratory Animal Care standards. All experiments were approved by the Tulane Animal Care and Use Committee. All macaques were negative for SIV controller alleles Mamu-A*01, B*08, and B*17 with the exception of DE33, which was A*01 positive (89).

In the study from which 5 RM treated with ART for 6 months were examined, Indian RM were housed at Bioqual, Inc. (Rockville, MD) in accordance with the Association for Assessment and Accreditation of Laboratory Animal Care standards. RMs were infected with 1 x 10^6 infectious units (IU) of SHIV.D intravenously. Following 10 weeks of viremia, all 10 RMs were initiated on combination ART of tenofovir (TDF; 5.1mg/kg), emtricitabine (FTC; 40mg/kg) and dolutegravir (DTG; 2.5mg/kg) subcutaneously and maintained until necropsy at 6 months port-ART. Following perfusion

and formalin fixation at necropsy, brain cortex lobes were isolated and embedded in paraffin blocks for all RM.

Immunohistochemistry

Formalin-fixed paraffin-embedded (FFPE) tissue blocks of the occipital, temporal, and frontal lobes were obtained from Tulane National Primate Research Center (TNRPC). FFPE blocks of the basal ganglia, brainstem, and occipital, temporal, frontal, and parietal lobes were obtained from Bioqual, Inc. Tissue blocks were cut to 5 microns and placed on charged slides. Slides were deparaffinized in xylene for 2x 10 minutes and rehydrated using an ethanol gradient for 10 minutes in each concentration (100%, 90%, 70%). Antigen retrieval was performed by heating slides in Antigen Unmasking Solution, citrate buffer (Vector) diluted in water at 92°C for 20 minutes, then cooled to room temperature (RT) for 20 minutes. Following heat pre-treatment antigen retrieval, sections were washed in water (5 min), then PBST (0.05% Tween 20) for 5 minutes. Sections were then incubated with Bloxall Endogenous Peroxidase and Alkaline Phosphatase Blocking Solution (Vector) for 10 minutes in a humidity chamber at RT. After 2x 5 min PBST wash, sections were incubated with Protein Block, serum-free (Dako) for 30 minutes at RT. Primary antibodies were diluted in antibody diluent (Dako) and incubated at 4°C overnight (Table 2.1).

Table 2.1: Immunohistochemistry antibodies and specifications.

Primary antibody	**Source**	**Concentration**	**Antigen retrieval concentration**	**Secondary antibody**	**Source**
CD3	Agilent (A0452)	1:800	1:100	HRP labelled Anti-Rabbit	Dako EnVision+ system (K4003)
CD68	Agilent (M0814)	1:400	1:200	HRP labelled Anti-Mouse	Dako EnVision+ system (K4001)
MAC387	Agilent (M0747)	1:100	None	HRP labelled Anti-Mouse	Dako EnVision+ system (K4001)
IBA1	Millipore Sigma (MABN92)	1:500	1:100	HRP labelled Anti-Mouse	Dako EnVision+ system (K4001)

HRP: horseradish peroxidase

After 2x 5min PBST washes, sections were incubated with appropriate HRP conjugated secondary antibody (Dako) for 30 minutes in dark at RT (Table 2.1). After 2x 5 min PBST wash, antigens were detected by DAB chromogen development (1 drop DAB chromogen per 1mL DAB+ substrate buffer (Dako)) and counterstained with hematoxylin for 30 seconds. Sections were dehydrated using an ethanol gradient for 2x 2 mins each concentration (70%, 90%, 100%) and 2x 5 minutes xylene. Coverslips were mounted using permanent mounting media. Slides were imaged using Keyence BZ-X700 microscope and positively stained cell counts were quantified using accompanying Batch Analysis Software. Cell count was quantified using Batch Analysis Software and averaged from 10 nonoverlapping 20X images per brain section of each RM. Total average values for each cell type in each RM were calculated by taking the arithmetic mean from all representative images from all three brain sections studied (10 per brain region). Graphs were generated using GraphPad Prism 8.2 software.

In Situ Hybridization

SHIV.D RNA and DNA were visualized using RNAscope and DNAscope in situ hybridization according to the specifications of the manufacturer (ACD Bio). The probe utilized for RNAscope (ACD) was a SIVmac anti-sense RNA probe. RNAscope probes do not bind to double-stranded DNA and only bind to single-stranded anti-sense RNA. Formalin-fixed paraffin-embedded (FFPE) tissue blocks of the occipital, temporal, and frontal lobes were obtained from Tulane National Primate Research Center (TNRPC). FFPE blocks of the basal ganglia, brainstem, and occipital, temporal, frontal, and parietal lobes were obtained from Bioqual, Inc. Tissue blocks were cut to 5 microns and placed on charged slides. Slides were deparaffinized in xylene for 10 minutes, washed 2x 2 minutes in 100% ethanol, and air dried. Sections were boiled for 15 minutes in 1X Target Retrieval solution (ACD Bio) and removed to water. Tissue sections were treated with hydrogen peroxide for 10 minutes at RT, then protease for 30 minutes in a humidity chamber at 40°C. Custom probes targeting SHIV.D RNA and DNA (sense strand) were designed with ACD Bio. RNA and DNA probes were hybridized for 2 hours in a humidity chamber at 40°C. RNA and DNA were detected by amplification and chromogenic development using RNAscope 2.5 High Definition – Red Assay kit (ACD Bio). Tissue sections were counterstained with hematoxylin for 30 seconds, washed in water, then dried in a 60° dry oven for 15 minutes. Slides were cleaned with xylene and coverslips were mounted using permanent mounting media. Slides were imaged using Keyence BZ-X700 microscope and the RNA area was quantified using accompanying Batch Analysis Software. The area of positive signal (RNA) or the number of nuclei containing positive signal (DNA) was

quantified using Batch Analysis Software and averaged from 10 nonoverlapping 20X images per brain section of each RM. Total average values for each nucleic acid in each RM were calculated by taking the arithmetic mean from all representative images from all three brain sections studied (10 per brain region). Graphs were generated using GraphPad Prism 8.2 software.

Dual Target IHC/ISH

FFPE brain tissue section slides were deparaffinized in xylene for 2x 10 minutes, rehydrated using an ethanol gradient for 2x 2 minutes in each concentration (100%, 90%, 70%), then washed in water. For brightfield microscopy staining, antigen retrieval was performed by heating slides in Antigen Unmasking Solution, citrate buffer (Vector) diluted in water at 92°C for 20 minutes, then cooled to room temperature (RT) for 20 minutes. Following heat pre-treatment antigen retrieval, sections were washed in water (5 min), then PBST (0.05% Tween 20) for 5 minutes. Sections were then incubated with Bloxall Endogenous Peroxidase and Alkaline Phosphatase Blocking Solution (Vector) for 10 minutes in a humidity chamber at RT. After 2x 5 minutes wash with 1X RNAscope Wash Buffer (ACD Bio), RNA probes were hybridized for 2 hours in humidity chamber at 40°C. RNA amplification was performed using RNAscope 2.5 High Definition – Red Assay kit (ACD Bio) according to the specifications of the manufacturer. After 2x 5 min PBST wash, sections were incubated with Protein Block, serum-free (Dako) for 30 minutes at RT. Primary antibodies were diluted in Antibody diluent (Dako) at 4°C overnight. After 3x 10min PBST wash, sections were incubated with appropriate HRP conjugated secondary antibody (Dako) for 30 minutes in dark at RT. After 2x 5 min PBST wash, antigens were

detected by DAB chromogen development (1 drop DAB chromogen per 1mL DAB+ substrate buffer [Dako]) and counterstained with hematoxylin for 30 seconds. For fluorescent staining, antigen retrieval, blocking, and HRP-tagged fluorophore development were performed using the Opal manual 4-color IHC kit (Akoya Biosciences) according to the manufacturer's protocol. RNA amplification and subsequent IHC was performed as described above, followed by DAPI counterstaining (Akoya). Slides were washed in water and dried in 60°C dry oven for 15 minutes. Slides were cleaned with xylene and coverslips were mounted using permanent mounting media. Slides were imaged using Keyence BZ-X700 microscope.

Results

SHIV.D Infection in Rhesus Macaques

Six female RMs were infected with SHIV.D intravaginally or intravenously as previously described (Table 2.2) (89). A viral set point of $>10^3$ viral copies/mL (c/mL) was established for at least 24 weeks. ART (daily, subcutaneous emtricitabine, tenofovir disoproxil fumarate, and dolutegravir) was administered for 24 weeks, followed by ATI. Two RMs (FR55, GA67) were restarted on ART following ATI. Based on the ART status, immunopathogenesis, and viremia, the RMs were divided into three groups: 1. progression (n= 2), where RMs experienced plasma viremia > 106 c/mL and were euthanized for clinical deterioration, 2. off ART (n= 2), where RMs underwent necropsy off ART without overt signs or symptoms of simian acquired immunodeficiency syndrome (AIDS), and 3. on ART (n= 2), where both RMs were necropsied on ART with suppressed viremia without signs or symptoms of simian AIDS.

Table 2.2. TF SHIV.D infection and pathological findings at necropsy.

RM	Treatment group	Mode of infection	Plasma VL at necropsy	Months post infection	Reason for euthanasia	Notable CNS pathology	Notable peripheral pathology
DE33	Progression	intravaginal	10^6 c/mL	18	clinical deterioration	Nothing of significance.	Lymphoid hyperplasia of bone marrow [3-4]. Chronic erosive inflammation of ileocecal valve [3]. Lymphoid hyperplasia of pancreas [2]. Lymphoid hyperplasia of tonsil, lymph node [4]. Nodular hyperplasia of kidney [3]. Cytoplasmic vacuolization of hepatic parenchymal cells [4]. Nodular hyperplasia of lymphoid tissue of lung [1].
EJ94	Progression	intravaginal	10^7 c/mL	39	clinical deterioration	Vacuolar degeneration, vacuolar lesions with few lymphocytes.	Chronic inflammation of lung with edema and epithelial hyperplasia [4]. Syncytial giant cells in lung [3]. Chronic inflammation of liver [1]. Diffuse lymphoid hyperplasia of lymph node [2]. Severe endometriosis [4].

Table 2.2. Continued.

RM	Treatment group	Mode of infection	Plasma VL at necropsy	Months post infection	Reason for euthanasia	Notable CNS pathology	Notable peripheral pathology
FE43	off ART (ATI)	intravaginal	10^4 c/mL	40	tissue collection	Multiple small inflammatory foci in occipital lobe, subcortical white matter, and meninges [1].	Chronic inflammation of lung, liver, and interstitial tissue of kidney [1]. Diffuse lymphoid hyperplasia of lymph node and splenic lymphatic follicle [2-3].
FT42	off ART (ATI)	intravaginal	<83 c/mL	36	tissue collection	Predominately perivascular inflammation of frontal cortex, temporal lobe, and thalamus [1].	Perivascular inflammation of lung [2]. Chronic inflammation of stomach [3]. Perivascular inflammation of ileum and cecum [1].
FR55	on ART	intravenous	<83 c/mL	45	clinical deterioration	Nothing of significance.	Focal granulomatous inflammation and histiocytosis of lymph node [2]. Mycobacterium avium mediated inflammation and necrosis of lymph node [4]. M. avium mediated granulomatous inflammation of stomach, jejunum, and colon [2-3].
GA67	on ART	intravenous	<83 c/mL	35	tissue collection	Nothing of significance.	Nothing of significance.

Note. Pathology finding determination and grading performed by a TNPRC veterinary pathologist. Pathology grading degrees: [1] = minimal; [2] = mild; [3] = moderate; [4] = severe. ART: antiretroviral therapy, ATI: analytical treatment interruption, CNS: central nervous system, RM: rhesus macaque, VL: viral load.

CNS and peripheral pathological findings at necropsy were recorded and scored.

Three RM had notable CNS pathological findings at the time of necropsy. EJ94 (progression) exhibited vacuolar degeneration and vacuolar lesions in the occipital lobe. FE43 (off ART) had small inflammatory foci in the occipital lobe, subcortical white matter, and meninges. FT42 (off ART) had perivascular inflammation in the frontal cortex, temporal lobe, and thalamus (Table 2.2).

SHIV.D Infection is Associated With Inflammatory Myeloid Cells in the CNS

To characterize the degree of inflammation in the brain of the SHIV.D infected RMs, occipital, temporal, and frontal cortex sections were immunostained with antibodies against CD68 for resident tissue macrophages, MAC387 for recently infiltrated monocyte-derived macrophages, and CD3 for T lymphocytes and expression of each was quantified (Figure 2.1A). Inflammatory lesions containing CD68+ and MAC387+ cells were seen in RMs from the progression group, and an accumulation of CD68+ macrophages was found in the off-ART group. Vacuolar lesions containing CD68+ macrophages and multinucleated giant cells were observed in Progression RM. Infiltration of MAC387+ monocyte-derived macrophages continued in the animals in the on-ART group. However, small inflammatory foci and perivascular inflammation persisted in the CNS of off-ART and on-ART RMs, including FT42, a spontaneous controller of plasma viremia. The highest levels of all quantified immune cell markers were found in the progression group (Figure 2.1B). The mean number of CD68+ cells in the progression group was 46.6 (DE33) and 230.6 cells/mm^2 (EJ94); in the off-ART group, 65.4 (FE43) and 31.1 cells/mm^2 (FT42) and in the on-ART group, 39.7 (FR55) and 19.6 cells/mm^2 (GA67). The mean number of

MAC387+ cells in the progression group was 5.33 (DE33) and 13.3 cells/mm^2 (EJ94). In the off-ART group, there were 1.52 (FE43) and 3.13 MAC387+ cells/mm^2 (FT42), and in the on-ART group, 1.27 (FR55) and 1.02 MAC387+ cells/mm^2 (GA67). The mean number of CD3+ T cells in the progression group was 44.7 (DE33) and 50.9 cells/mm^2 (EJ94). In the off-ART group, there were 5.60 (FE43) and 4.31 CD3+ cells/mm^2 (FT42). In the on-ART group, the mean was 31.0 (FR55) and 33.3 CD3+ cells/mm^2 (GA67).

Viral RNA and DNA Persist in the CNS After ART suppression

Viral DNA and RNAscope, a highly specific and sensitive next generation *in situ* hybridization (ISH) technique, was performed on FFPE occipital, temporal, and frontal cortex sections and quantified (Figure 2.2). RNAscope and DNAscope have the ability to detect single virions and transcripts, and resulting RNA- and DNA-positive signal can be used to quantify viral nucleic acids and differentiate between active viral replication and low-level viral RNA transcription (150). Punctate, nuclear RNA signal represents viral particles or low-level transcription of viral RNA, while large areas of high intensity signal amplification represent active viral replication (150). Using RNAscope, high levels of viral RNA were found in animals in the progression group, with some localizing to vacuolar lesions. Lower levels of viral RNA persisted in the CNS in animals from the off-ART and on-ART cohorts. Using a probe targeting the sense strand of SHIV.D DNA, proviral DNA was detected inside the nuclei of cells in all three treatment groups (Figure 2.2). Both replicating SHIV.D RNA and proviral DNA were found in the CNS of RM GA67 after 6 months of ART suppression.

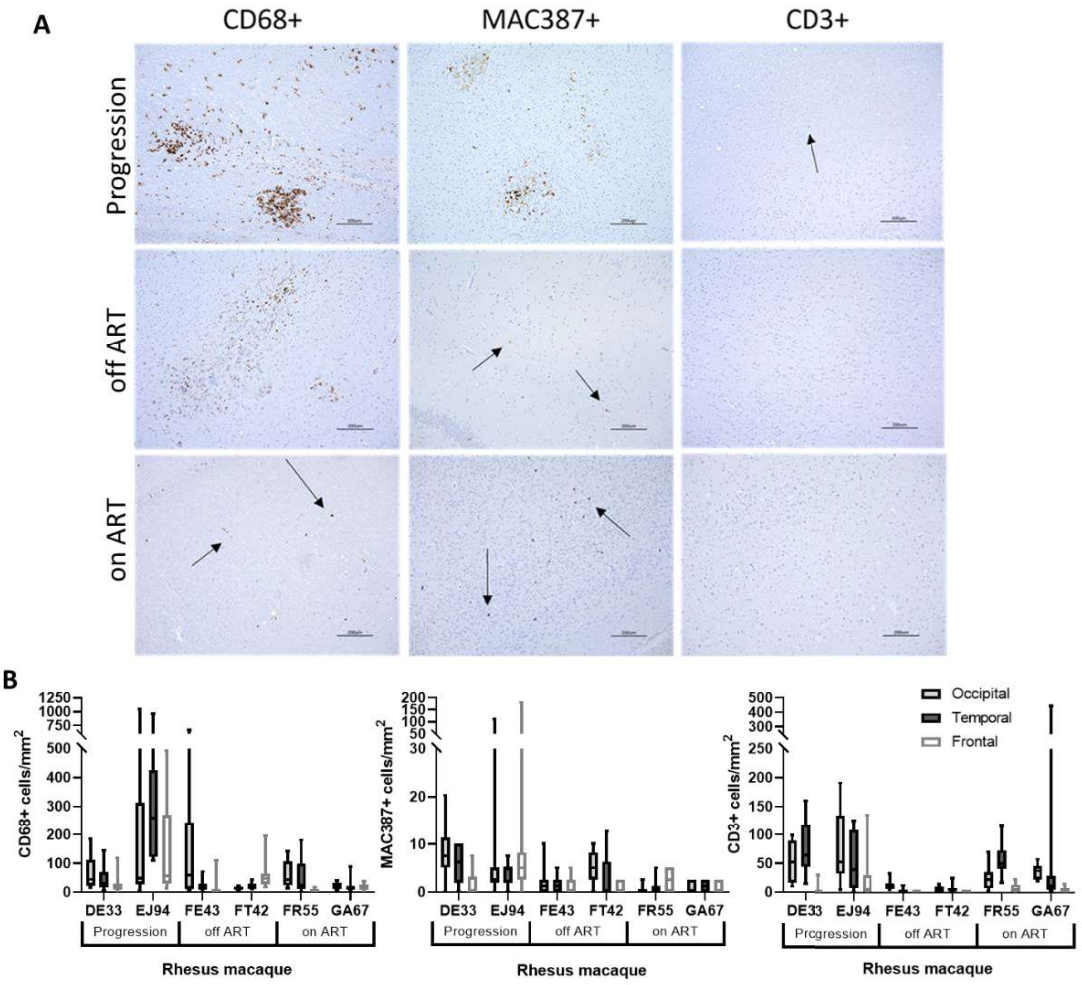

Figure 2.1: Quantitative immunohistochemistry of immune cell markers in TF SHIV RM brain tissue. Immunohistochemistry (IHC) staining of CD68+, MAC387+, and CD3 + cells in brain tissue of progression, off-ART, and ART suppressed RMs (A). Representative images from occipital, temporal, and frontal lobes at 10X magnification are shown. Scale bar = 200μm. Target cells were quantified using Keyence BZ-X700 Microscope and accompanying Batch Analysis Software to determine the average number of IHC stained cells from 10 nonoverlapping 20X images per brain section of each RM (B). 20X frame area = 393,880μm². Box and whisker plots are presented as mean values of counts ± quartiles, with whiskers representing the range.

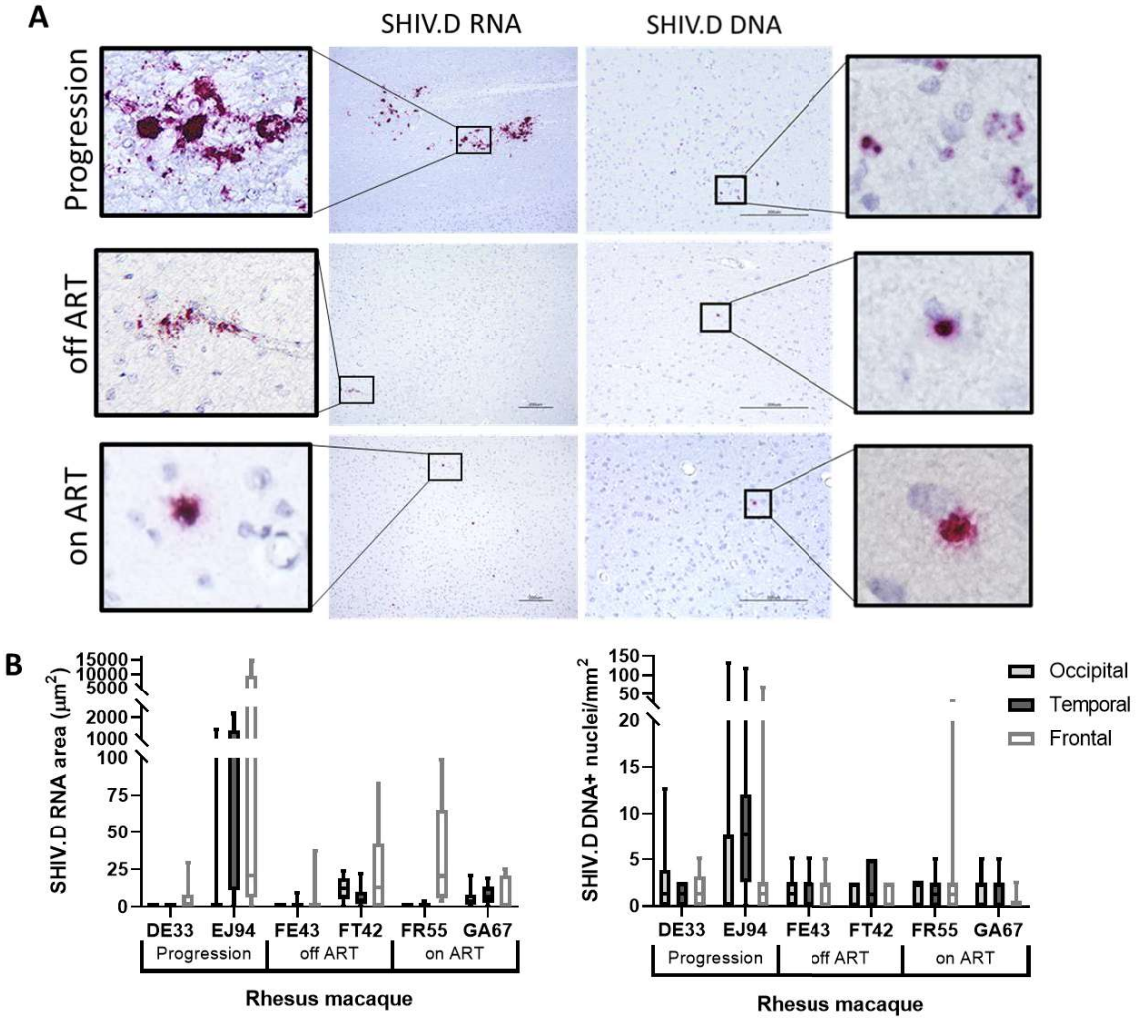

Figure 2.2: Quantitative viral RNA and DNA in situ hybridization in TF SHIV.D RM brain tissue. RNAscope (left) and DNAscope (right) in situ hybridization (ISH) of replicating viral RNA and proviral DNA in brain tissue of progression, off-ART, and ART suppressed RM (A). Representative images from occipital, temporal, and frontal lobes are shown at 10X (RNA) and 20X (DNA) magnification. Inserts = 40X magnification. Scale bar = 200µm. The area of SHIV.D RNA positive signal (µm^2) or the number of nuclei containing proviral DNA/mm^2 were quantified using Keyence BZ-X700 Microscope and accompanying Batch Analysis Software to determine the average area of positive signal (RNA) or the mean number of SHIV.D DNA-containing nuclei (DNA) from 10 nonoverlapping 20X images per brain section of each RM (B). 20X frame area = 393,880µm². Box and whisker plots are presented as mean values of counts ± quartiles, with whiskers representing the range.

The mean SHIV.D RNA positive signal area in the progression group was 2.13 and 2368.7 μm^2 for DE33 and EJ94, respectively. In the off-ART group, the mean area of RNA positive signal was 3.20 (FE43) and 33.3 μm^2 (FT42). In the on-ART group, the mean area of the SIV RNA positive signal was 12.6 (FR55) and 21.3 μm^2 (GA67). The mean number of SHIV.D DNA+ nuclei in the progression group were 1.95 (DE33) and 13.7 cells/mm^2 (EJ94). In the off-ART group, the mean number of SHIV.D DNA+ cells were 1.35 (FE43) and 1.27 cells/mm^2 (FT42). In the on-ART group, the number of viral DNA+ cells were 2.37 (FR55) and 0.846 cells/mm^2 (GA67).

SHIV.D Replicates in Myeloid Cells During ART Suppression

Dual target IHC/RNAscope co-staining was performed on occipital and temporal cortex sections (Figure 2.3). Colocalization between IBA1+ (brown) microglia and macrophages and SHIV.D RNA (red) was frequent and present in all three treatment groups, including RM GA67 after 6 months ART suppression (Figure 2.3). In Progression RM (Figure 2.3A), syncytia and clusters of microglial cells and SHIV.D+ RNA were observed at the site of vacuolar lesions. Colocalization between CD3+ T cells and SHIV.D RNA was not prevalent (Figure 2.4). This demonstrates persistent SHIV.D viral replication inside CNS myeloid cells in the CNS during ART suppression.

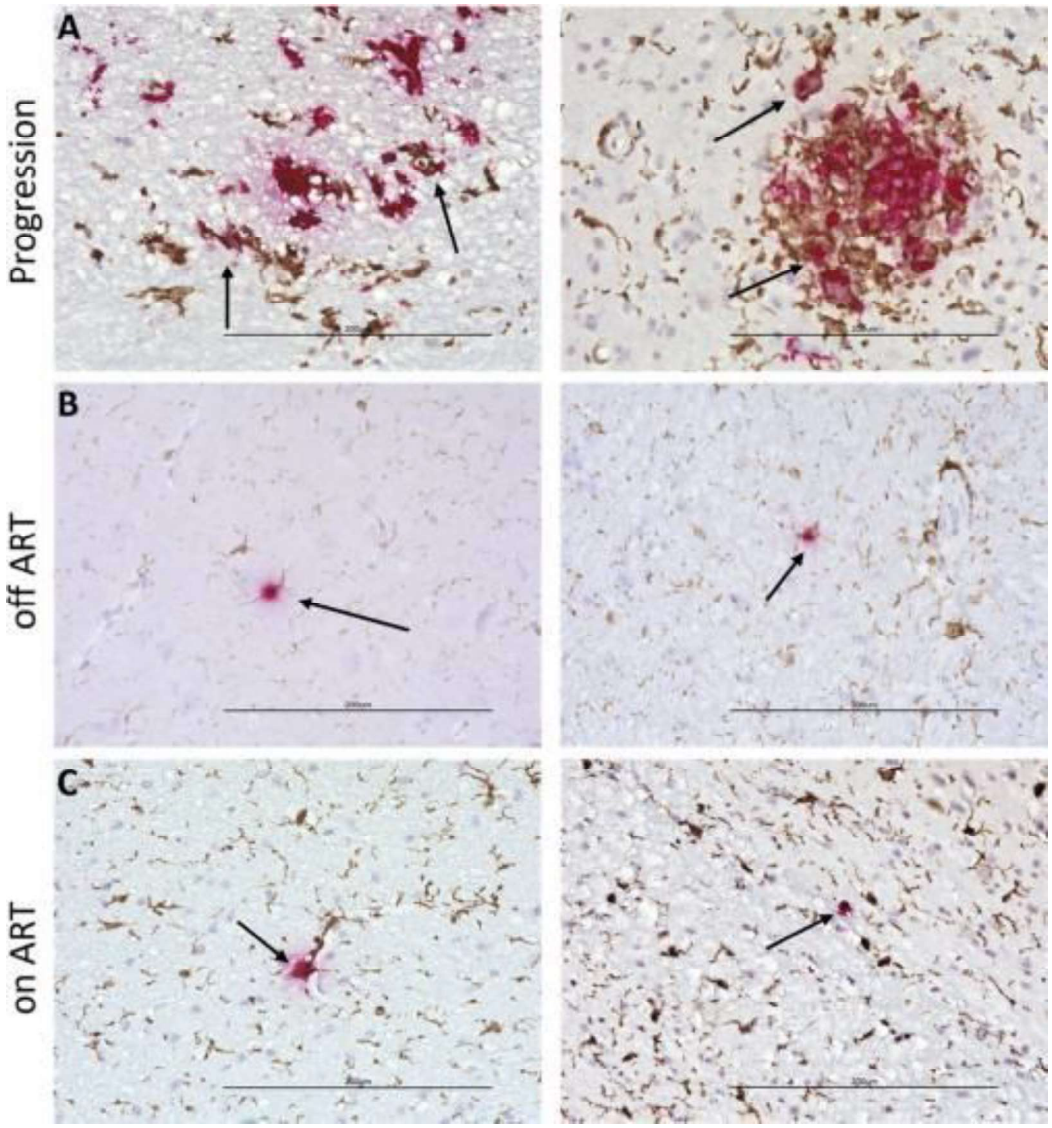

Figure 2.3: TF SHIV.D replicates and persists in myeloid cells. Dual RNAscope ISH (red) and IBA1 IHC (brown) reveal RNA/IBA1 + microglia/macrophage co-localization (arrows) in viremic RM EJ94 (A) and at low levels during ATI in off ART RM FE43 and FT42 (B) and ART suppression in on-ART RM GA67 and FR55 (C). Representative images are 40X magnification. Scale bar = 200μm.

SHIV.D DNA and Myeloid-Mediated Inflammation Persist in the RM Brain After 6 Months ART

Based on pilot study data, a robust study to investigate SHIV.D in the CNS on long-term ART in 10 RM was initiated. Five RM were necropsied after 6 months suppressive ART. IHC-based quantification of inflammation and virus was repeated in the brains of these RM. In this cohort, basal ganglia, brainstem, and parietal lobe were included for IHC/ISH staining.

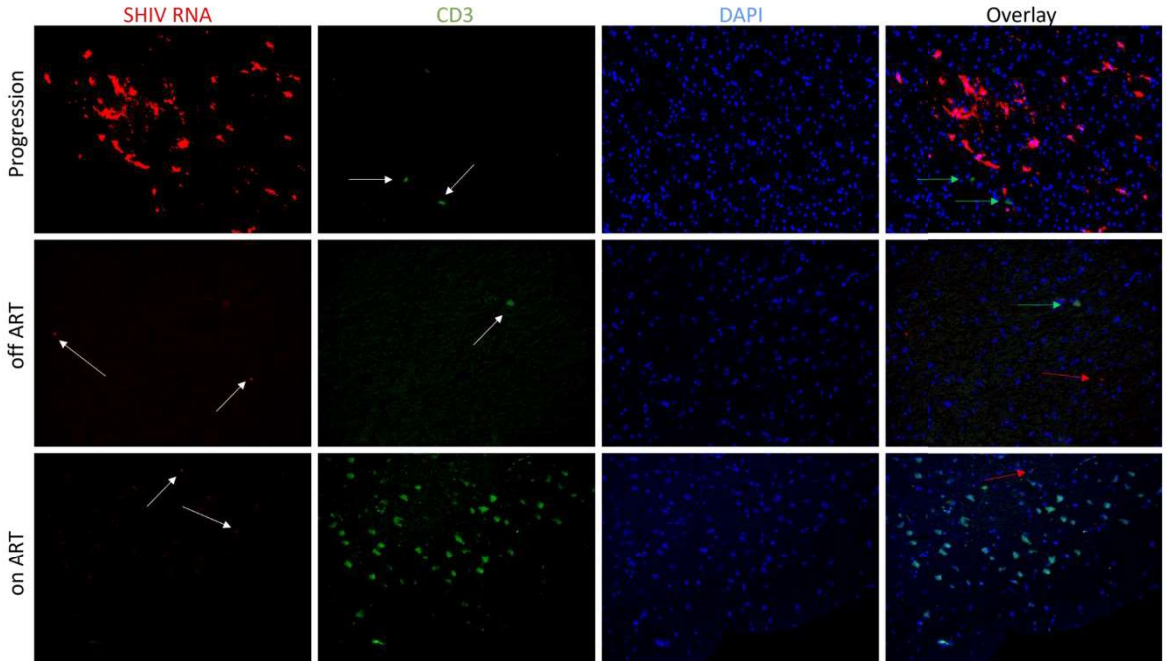

Figure 2.4. SHIV RNA/CD3 dual stain shows lack of colocalization. Opal (Akoya) multiplex immunohistochemistry for CD3 (green), SHIV.D RNA (red), and DAPI (blue) targets was performed on brain tissue sections from Progression, off ART, and on ART RM. Co-localization between SHIV.D RNA and CD3+ was rarely observed.

After 6 months ART, there is decreased replicating viral RNA and CD3+ T cells compared with pilot study Progression RM (Figure 2.5A, E). MAC387+ monocyte-derived macrophages are found at lower levels after 6 months ART compared to viremic RM but continue to infiltrate in all 6 brain regions studied (Figure 2.5D). SHIV.D DNA and CD68+ myeloid cells persist at similar levels to Progression RM after 6 months suppressive ART (Figure 2.5B-C).

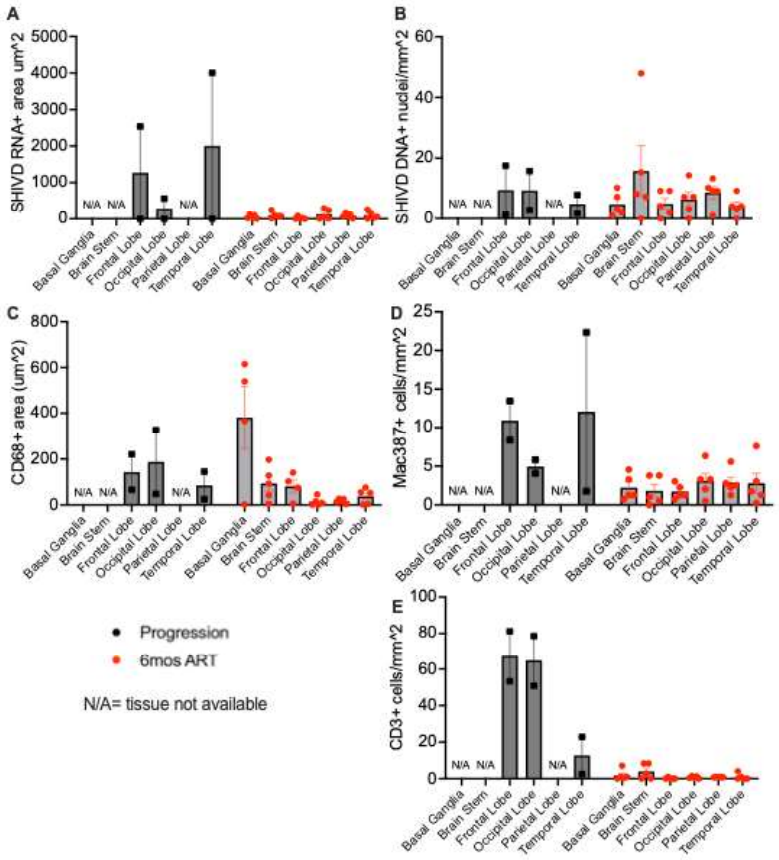

Figure 2.5: Quantification of RNA/DNAscope and IHC staining of brain sections after 6 months suppressive ART. (A) SHIV.D RNA+ area (μm^2) (B) SHIV.D DNA+ nuclei/mm^2, (C) CD68+ area (μm^2). (D) MAC387+ cells/mm^2. (E) CD3+ cells/mm^2. Black: Progression RM (n=2, SHIV.D-infected, viremic), red: SHIV.D-infected RM on ART for 6 months (n=5).

Interim Discussion

A NHP model of HIV persistence in the CNS is critical to elucidate viral reservoir dynamics and studying viral pathogenesis and persistence in the brain. Because human brain samples are scarce and available only in rare clinical scenarios requiring biopsy or postmortem, NHP models are crucial to studying the progression of HIV-associated disease in the CNS. Most SIV/NHP models are associated with rapid progression of disease and onset of SIV encephalitis (46,74). Early SHIV/NHP models with less overt encephalitis failed to consistently maintain CD4 and CCR5 tropism, limiting their biological relevance in the CNS (81,84,90). A body of work now demonstrates the relevance of SHIVs encoding TF HIV-1 *env* genes, as they mirror viral kinetics, lymphoid pathogenesis, and induction of authentic HIV-specific adaptive immune responses (81,88,90,151). Previous research determined that TF SHIV.D.191859, specifically, recapitulates additional components of HIV-1 infection, including ongoing viremia without frequent spontaneous control, and rapid suppression of viremia with ART with viral persistence in the periphery and lymphoid reservoirs (89). Here, we demonstrate that TF SHIV.D actively replicates in the brain, causes neuropathogenesis, and persists in the CNS through antiretroviral therapy in rhesus macaques.

Using RNAscope *in situ* hybridization, we demonstrate that SHIV.D replicates in the CNS during viremia, but also at low levels during ATI and ART suppression. Large, high-intensity areas of RNAscope signal indicating active viral replication were identified in RM in all three treatment groups (150). Though SHIV.D is dual-tropic and known to efficiently infect CD4+ T cells *in vitro* and systemically (81,84), we found replicating virus

predominantly in myeloid cells in the CNS. This is consistent with CNS HIV-1 infection in humans, where macrophages, microglia, and monocytes are the primary infected cell types in the brain (23,27,28,152–155). Additionally, TF SHIV.D replication persists at low levels in the CNS despite undetectable plasma viremia. This emulates HIV-1 CNS pathogenesis in humans, potentially due to the inefficacy of ART drugs crossing the blood-brain barrier (156–158), and solidifies the need for robust CNS persistence research with a biologically relevant animal model.

Using DNAscope, we found proviral SHIV.D DNA in multiple brain regions in animals both on and off ART. Previous SHIVs and SIV/RM model systems have been unable to replicate continuous CCR5 tropism in RMs, limiting infection and pathogenesis in the brain (81,84,88,89,159,160). This further validates the potential for use of TF SHIV.D in latency and curative research in the CNS reservoir.

Using immunohistochemistry, we found myeloid-mediated inflammation, inflammatory foci, and vacuolar lesions and degeneration in the CNS of TF SHIV.D progression animals. Multinucleated giant cells and clusters of microglial cells at the site of lesions were also observed in some RM. Interestingly, lower levels of inflammation persisted in the off-ART RMs and ART-suppressed RMs even in the absence of viral RNA or DNA. Further research to investigate potential mechanisms of persistent inflammation not localized in areas of high levels of SHIV.D replication is in progress.

This study has several limitations. The sample size (n= 6, 2 per group) was small, which hindered statistical analyses. However, additional studies using this animal model to examine CNS pathogenesis are underway. The CNS samples were from a small

retrospective study of banked brain tissues. Since we have demonstrated that TF SHIV.D is a biologically relevant model for HIV pathogenesis in the CNS, additional studies with larger RM cohorts are underway. Secondly, the number of available archived tissue samples was limited, and no fresh frozen brain tissue was available. Finally, cerebrospinal fluid (CSF) samples were not obtained in these animals, so no CSF viral loads could be obtained. CSF viral load levels would have been of particular interest for RM FT42, which spontaneously controlled plasma viremia, but which nonetheless maintained CNS viral replication.

In an ongoing study with a larger cohort of RMs infected with TF SHIV.D (n=10), further investigation will elucidate viral kinetics, reservoir dynamics, and mechanisms of persistent pathogenesis in the CNS. Of this cohort, five RM have been necropsied after 6 months ART suppression and were included in this study. Results of quantitative IHC and ISH revealed that myeloid-mediated inflammation and levels of proviral DNA persist in the brains of RM after 6 months ART. This research demonstrates that the TF SHIV.D/RM model is valuable for investigating the dynamics of HIV neuropathogenesis and persistence in the CNS reservoir.

CHAPTER 3

NANOSCALE FLOW CYTOMETRY REVEALS INCREASED CIRCULATING MICROGLIAL AND NEURONAL EXTRACELLULAR VESICLES DURING SHIV.D INFECTION AND ART SUPPRESSION

Chapter Abstract

EVs have marked biological and clinical significance as both functional mediators of disease pathogenesis and clinical biomarkers. Blood plasma EVs are non-invasive to obtain and give valuable insight into several difficult to assess pathologic processes, including neurodegeneration and neurological dysfunction, traumatic brain injury, cancer, and viral infections (121,123,161–165). However, robust methods that phenotype circulating plasma EVs, differentiate them by cell type of origin, and allow for simultaneous detection of multiple parameters are lacking. Here, we investigate the relative abundance of circulating plasma EV (PEV) populations in a SHIV.D/RM model of HIV neuropathogenesis.

PEV from 10 RM infected with SHIV.D were isolated before infection, during acute viremia, and during ART suppression. Using two four-parameter panels, we can quantify the relative amounts of the following subsets of plasma EVs: tetraspanin CD81+, CD11b+ macrophage-derived, CD14+ monocyte-derived, TMEM119+ microglia-derived, CD171+ neuron-derived, CD3+ T cell-derived, and CD31+ endothelium-derived EVs. This multiplex technique allows for quantification of multiple subsets of EVs in one sample as well as identification of EVs expressing multiple combinations of our proteins of interest. Applying this method to RM plasma samples allows investigation of specific cell-

derived EV populations in an animal model of HIV infection over time. Comparing fluorescence intensity of each marker on CD81+ EVs revealed an increase in CD171+ neuron-derived EVs and TMEM119+ microglia-derived EVs during acute viremia that was sustained or further increased, respectively, during ART-mediated viral suppression. These findings enhance our understanding of EV production during HIV/SHIV infection and demonstrate that they may play an important functional role during persistent HIV neuropathogenesis during ART treatment. The ability to study brain- and immune cell-derived EV populations in the plasma increases our understanding of EV functions and behavior in the brain during HIV infection, advance our capabilities for biomarker research, and provide insight into potential neuropathogenesis or neurological disease processes as they are occurring in a living organism.

Materials and Methods

Rhesus Macaques

RM were maintained at Bioqual, Inc. (Rockville, MD) according to the Association for Assessment and Accreditation of Laboratory Animal Care standards and all experiments were approved by the Bioqual, Inc. Institutional Animal Care and Use Committee. RM were sedated with ketamine HCl at 10mg/kg body weight for blood draws and SHIV inoculation. Peripheral blood was drawn into EDTA anticoagulant-containing tubes (purple top). RMs were intravenously infected with high titer SHIV.D.191859 challenge stock. After plasma viral load (VL) set point was established, daily subcutaneous combination ART (TDF 5.1mg/kg, FTC 40mg/kg, and DTG 2.5mg/kg) administration began 10 weeks post infection. Blood was collected before infection and at several points

over the course of acute infection and ART-mediated viral suppression (Figure 3.1A). Plasma and CSF viral loads were quantified using RT-qPCR by the Nonhuman Primate Virology Core Laboratory at Duke University (Figure 3.1B-C).

Plasma EV Isolation

Blood samples were gently inverted 6-8 times then centrifuged at 2000rpm for 20 minutes at room temperature (RT) to separate plasma layer. Plasma was aliquoted into microcentrifuge tubes (1mL/tube) and centrifuged at 17000g for 5 minutes to remove platelets and cellular debris (Figure 2). Platelet-poor plasma samples were transferred to new microcentrifuge tubes and stored at -80°C. Plasma from each RM (n=10) at three timepoints (pre-infection, during acute viremia at 11 days post-infection (DPI), and during ART-mediated viral suppression at 167 DPI) were used for analysis. Platelet-free plasma was incubated with Thrombin (System Biosciences) at a ratio of 500µL plasma:4µL Thrombin for 5 minutes at room temperature and centrifuged at 10000rpm for 5 minutes to remove fibrin and fibrinogen. EVs were precipitated from 250µL fibrin-free plasma by incubation with 63µL ExoQuick (System Biosciences) for 30 minutes at 4°C followed by centrifugation at 1500g for 30 minutes at 4°C. Pelleted EVs were resuspended in 400µL sterile phosphate-buffered saline (PBS; Corning) and filtered through 0.22µm microcentrifuge tube fitted filters (Millipore Sigma) by centrifugation at 1000g for 10 minutes at RT. Purified EV preparations at this step were used for characterization by ZetaView nanoparticle tracking analysis (NTA), EV marker antibody array, and transmission electron microscopy (TEM).

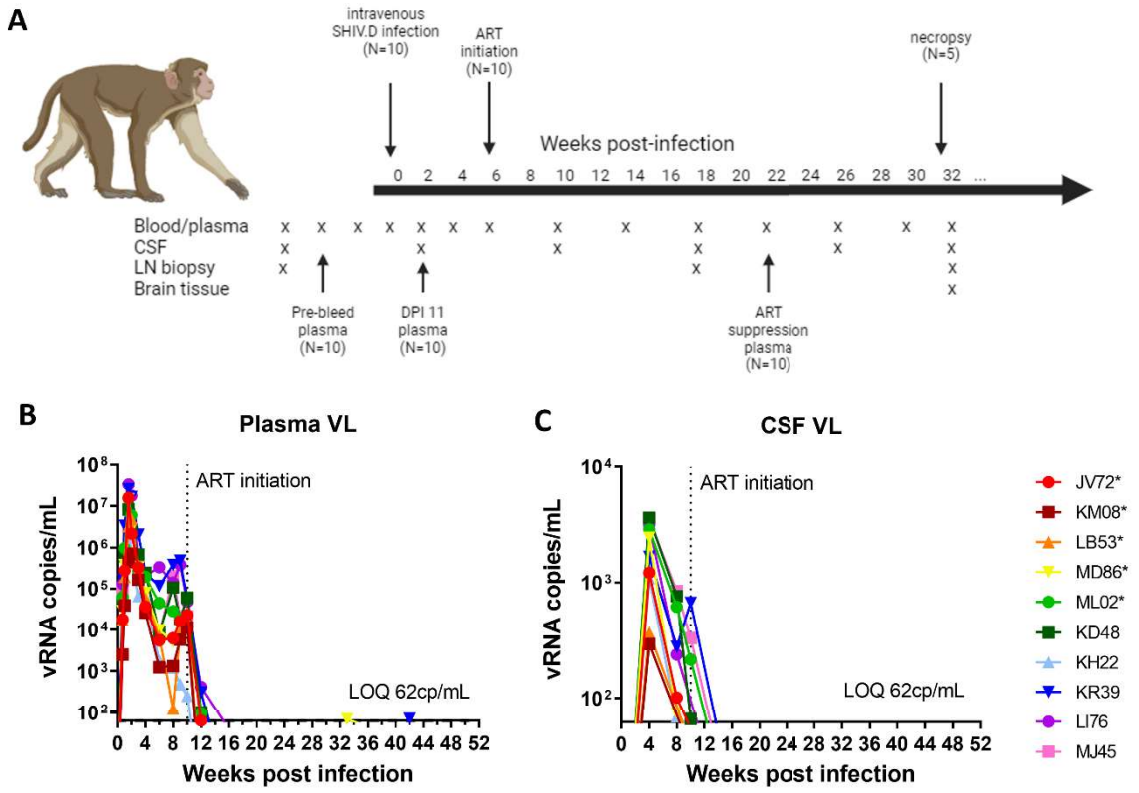

Figure 3.1. SHIV.D infection timeline and viral loads in RM cohort. 10 RM were infected with high titer SHIV.D intravenously. (A) Blood, CSF, LN, and brain tissue samples were taken at timepoints identified. Pre-bleed plasma, DPI 11 plasma, and ART suppression plasma from identified timepoints were used for nanoparticle tracking analysis (NTA) and flow cytometry. (B) and (C) ART administration began 12 weeks post infection, leading to suppression of detectable viral load in the plasma and CSF. Abbreviations: antiretroviral therapy (ART), cerebrospinal fluid (CSF), day post infection (DPI), limit of quantification (LOQ), lymph node (LN), viral load (VL), viral RNA (vRNA).

ZetaView Nanoparticle Tracking Analysis (NTA)

The size distribution and concentration of RM (n=10) plasma EVs from pre-infection to acute viremia (DPI 11) was measured using ZetaView nanoparticle tracker and analysis software (version 8.05.12 SP2; Particle Metrix). The instrument was calibrated before analysis using 100nm polystyrene standard particles (Life Technologies) for autoalignment and cleaned with sterile PBS and distilled water (dH_2O). EV suspensions were diluted to optimal NTA concentration (50-300 particles/frame) in sterile PBS and 2mL of each sample was injected into the instrument for recording. Between each sample recording, the instrument was flushed with PBS until <5 particles were detected. NTA video was captured at sensitivity = 85, shutter speed = 100, and frame rate = 30f/s. 12 positions were traced for analysis.

EV Marker Detection Arrays

EVs were pelleted from pooled platelet-poor, defibrinated, and filtered RM plasma using by incubation with ExoQuick (SBI) followed by centrifugation as previously described. Pellet lysis was performed using Exo-Check Exosome Antibody Array lysis buffer (SBI). Following EV pellet lysis, protein concentration was measured on a BioTek Cytation 1 microplate reader (Agilent) using Pierce 660nm Protein Assay Reagent (Thermo Scientific). 50µg protein lysate was incubated with Exo-Check Exosome Antibody Arrays (SBI) according to the manufacturer's instructions. Array containing antibodies against EV markers CD81, CD63, epithelial cellular adhesion molecule (EpCAM), annexin A5 (ANXA5), TSG101, FLOT1, intercellular adhesion molecule-1 (ICAM1), and ALIX were developed with SuperSignal™ West Femto Maximum Sensitivity Substrate (Thermo

Fisher) for 5 minutes at room temperature and imaged using an iBright FL1000 imaging system (Invitrogen). Golgi matrix protein GM130 was included as a negative control for cellular contaminants.

Electron Microscopy

EVs were isolated RM plasma as previously described, then fixed with 2% glutaraldehyde (Electron Microscopy Sciences) in PBS. Negative staining transmission electron microscopy (TEM) imaging was performed by Charles River Laboratories (Durham, NC).

Antibodies and Targets

The goal of our research was to develop a method to quantify EVs from different cell types of origin in the plasma. We used one common tetraspanin marker for plasma EVs (CD81) and specific markers for six cell subsets (macrophages, lymphocytes, neurons, microglia, monocytes, and endothelial cells) to determine EV origin (Table 3.1). The anti-human monoclonal antibodies used in this study were CD11b-BUV 737 (clone ICRF44, Thermo Fisher Scientific, Waltham MA), CD14-Pacific Blue (clone M5E2) and CD31-BUV 395 (clone WM59) (BD Biosciences, Franklin Lakes, NJ), CD171/L1CAM-AlexaFluor 488 (clone 2702C, Novus Biologicals, Centennial, CO), CD3-APC-Cy7 (clone OKT3) and CD81-PE-Cy7 (clone 5A6) (Biolegend, San Diego, CA) and TMEM119-AlexaFluor 700 (clone 1023426, R&D Systems, Minneapolis, MN) (Table 3.1). Marker clones were chosen for known NHP reactivity using the Non-human Primate Reagent Resource reactivity database (NHPRR).

Table 3.1: Antibodies used, their targets, and specifications.

Antibody	Target	Amount per test	Fluoro-chrome	Supplier	Catalog #	Clone
CD11b	macrophage-EVs	5µL	BUV 737	Thermo	367-0118-42	ICRF44
CD14	monocyte-EVs	2.5µL	Pacific Blue	BD	558121	M5E2
CD171	neuron-EVs	5µL	AlexaFluor 488	Novus	FAB7773G	2702C
CD3	T lymphocyte-EVs	5µL	APC-Cy7	Biolegend	317342	OKT3
CD31	endothelium-EVs	5µL	BUV 395	BD	565290	WM59
CD81	EVs (tetraspanin)	5µL	PE-Cy7	Biolegend	349512	5A6
TMEM119	microglia-EVs	5µL	AlexaFluor 700	R&D	FAB10313N	1023426

APC: allophycocyanin, BD: BD Biosciences, BUV: brilliant ultraviolet, Cy7: cyanine 7, PE: phycoerythrin, R&D: R&D Systems, TMEM119: transmembrane protein 119.

Instrumentation

A BD FACSymphony A5 Spectral Enabled (SE) flow cytometer (BD Biosciences) was used to conduct the analysis. The instrument is equipped with 5 lasers: blue (488nm excitation, 150mW power), red (637nm, 140mW), violet (405nm, 200mW), yellow-green (561nm, 150mW), and ultraviolet (355nm, 60mW), as well as 28 filters configured as 6B-3R-8V8UV-5YG, and square photomultiplier tubes (PMT) optimized for cascade array.

EV Flow Cytometry

Filtered EV suspensions prepared as previously described were incubated with 5µL human Fc seroblock (Biorad) for 10 minutes at RT, transferred to sterile round-bottom polystyrene tubes (Falcon), then stained with antibodies for 30 minutes at 4°C protected from light. Following antibody incubation, 400µL EV suspensions were fixed with 125µL 4% paraformaldehyde (PFA) in PBS for a final concentration of 1% PFA. With each set of

samples, a sterile PBS only control, negative EV control, pre-blocking EV control, sterile PBS 1% PFA with antibody cocktail control, single stain controls, and fluorescence minus one (FMO) controls were run in accordance with recommendations made by the MIFlowCyt-EV reporting framework (166,167). A membrane disruption control of unstained EVs lysed with 1% Triton X-100 (Thermo Fisher) for one hour was also used (168).

Data Acquisition

To ensure data resolution and avoid background noise, BD FACSymphony A5 SE was put through vigorous cleaning and system preparation. For each session, specialized BD Detergent Solution was run through the instrument for 15 minutes followed by 15 minutes of autoclaved deionized water. The sheath fluid in the system was thoroughly replaced with autoclaved deionized water obtained from Millipore Milli-Q Direct 16 water purification system. A PureFlo® Capsule filter (ZenPure Americas) was added to the fluidics line. Autoclaved deionized water was run through the instrument for one hour to minimize bubble formation. Daily calibration was conducted with BD Cytometer Set-up and Tracking beads. The cytometer detection threshold was optimized and set to 250. This cleaning and calibration procedure was performed for every data acquisition run, and the instrument was flushed by a sterile PBS run between controls and samples. Data, including mean fluorescence intensity (MFI) of EV sub-populations, were calculated using FlowJo_v10.9.0. Graphics were generated by FlowJo or created in BioRender.com.

Statistical Analysis

Comparisons and statistical analyses were performed using GraphPad Prism V9.4.1. To analyze NTA data, results were first tested for normal (Gaussian) distribution using the D'Agostino-Pearson test ($P < 0.05$) (169). All NTA data sets assumed normal distribution. Descriptive statistics were calculated for each group, and parametric paired t-tests were run to compare groups. To compare EV sub-population MFI between groups, all experimental data sets were again tested for normality using the D'Agostino-Pearson test. Of the six parameters texted, two assumed a Gaussian distribution (CD171, TMEM119), and four did not (CD11b, CD14, CD3, CD31). In data sets that did assume a normal distribution, repeated measures one-way ANOVA were run, followed by post-hoc paired t-tests (Dunnett's multiple comparisons tests) compared to the pre-infection control group. In data sets that were not distributed normally, Friedman one-way repeated measure analysis of variance tests was run, followed by Dunn's multiple comparisons tests. All graphs display individual values with no exclusion of outliers. In bar graphs, the bar represents the mean value with error bars representing the standard error of the mean.

Results

Characterization of RM Plasma EVs

Isolation of RM plasma EVs (PEV) was validated by ZetaView NTA, EV marker antibody array, and TEM (Figure 3.2).

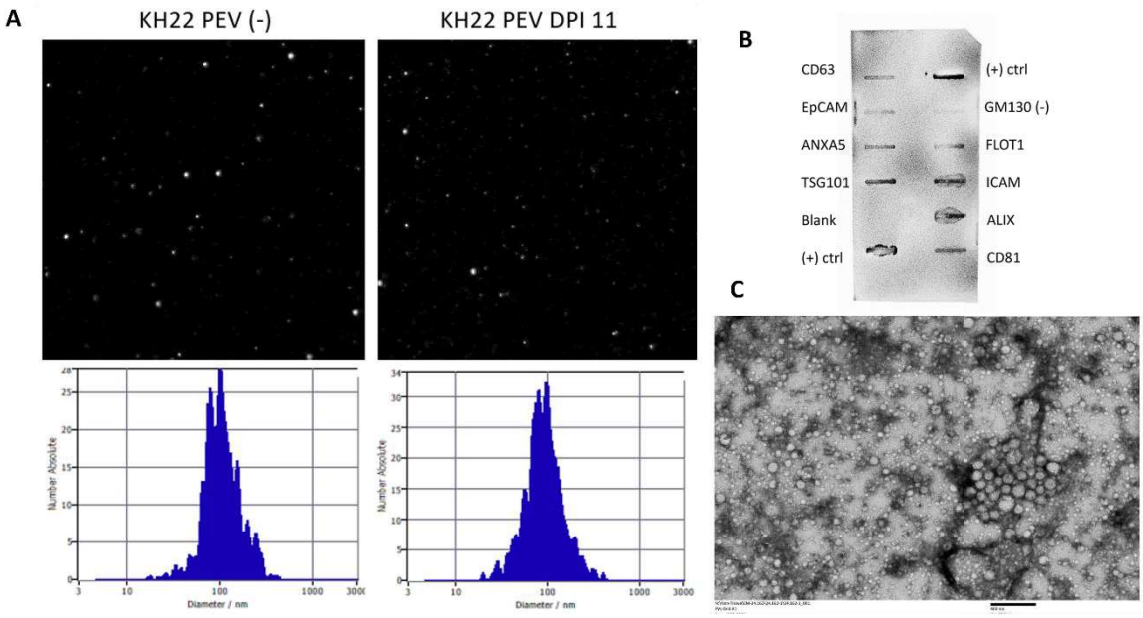

Figure 3.2. Characterization of RM PEV. (A) Representative NTA images from RM KH22 uninfected and DPI 11 PEV (above) and histograms of EV diameter (below). (B) EV marker array incubated with pooled EV lysate demonstrates sample enrichment with EV markers. (C) 12000X magnification image of PEV by TEM. Scale bar = 400nm.

NTA revealed the presence of appropriately sized nanoparticles (Figure 3.2A). Pooled RM PEVs express markers CD63, EpCAM, ANXA5, TSG101, FLOT1, ICAM, ALIX, and CD81 at higher intensity than cellular protein control GM130 (Figure 3.2B). TEM imaging revealed presence of vesicles ranging in size approximately from 50-200nm (Figure 3.2C). Using NTA, total PEVs showed no significant difference in concentration or size between RM plasma before infection and SHIV.D viremia at day post infection (DPI) 11 (Figure 3.3). The mean PEV concentrations were 6.73e10 EVs/mL plasma in uninfected RM and 4.75e10 EVs/mL plasma in infected samples.

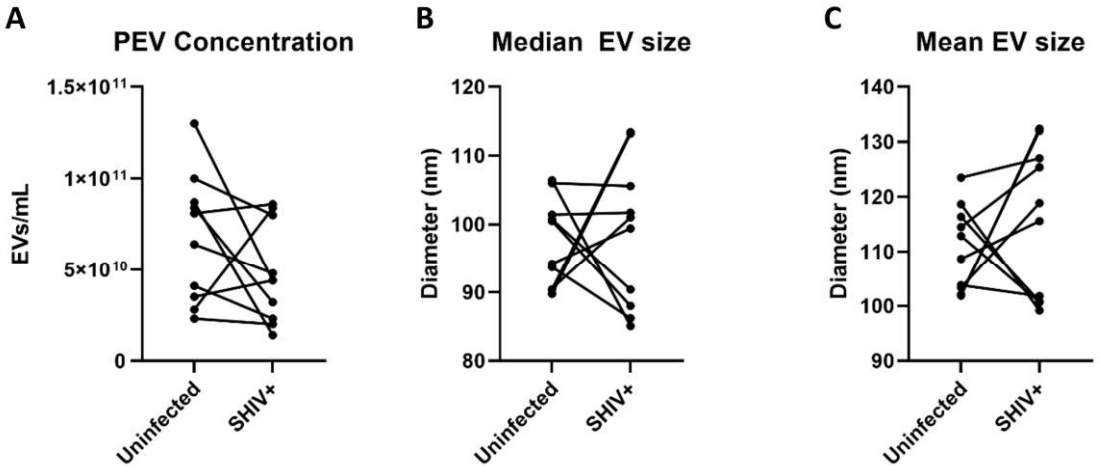

Figure 3.3. Total circulating PEV production and size are not changed by SHIV.D infection. NTA concentration (A) and median (B) and mean (C) diameter measurement was taken from PEV isolated from 10 RM before infection and during acute viremia at DPI 11. PEV: plasma extracellular vesicle.

The average (arithmetic mean) of median PEV diameter was 97.37nm in uninfected RM and 98.40nm in viremic RM. Average mean PEV diameter was 110.6nm in uninfected RM and 115.4nm in viremic RM (Figure 3.2A, Figure 3.3).

EV Flow Cytometry Workflow, Validation, and Gating Strategies

To analyze changes in specific cell-derived EV populations in the plasma over time, we developed a novel nanoscale multiplex conventional flow cytometry method capable of analyzing circulating EVs by markers of cellular origin (Figure 3.4).

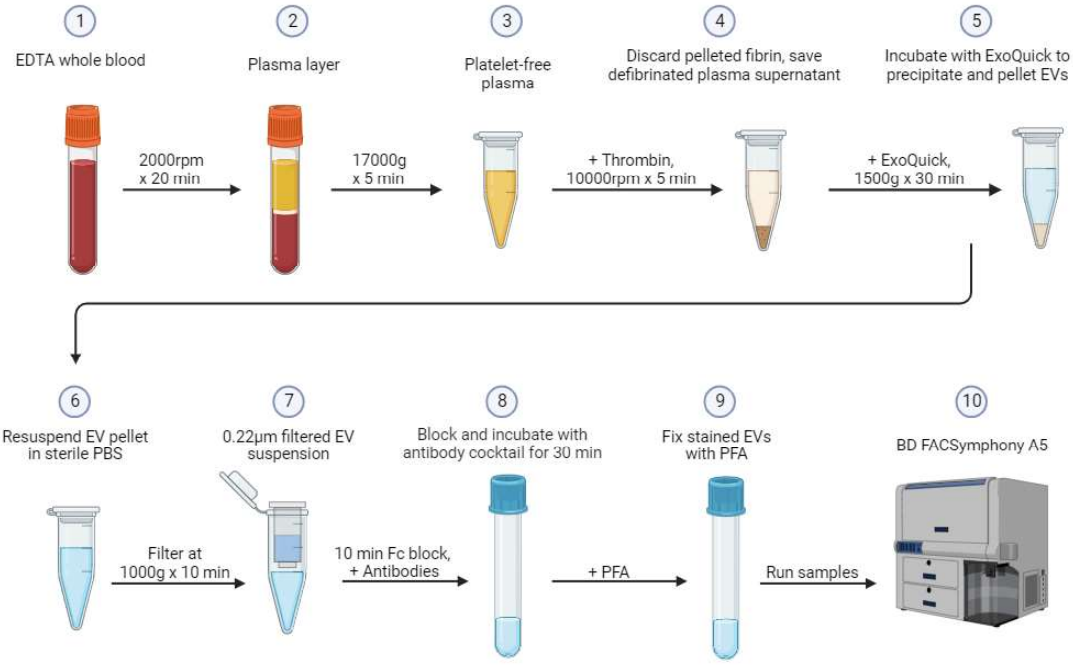

Figure 3.4. PEV flow cytometry workflow. 10mL EDTA anticoagulant-treated whole blood samples are centrifuged at 2000rpm for 20 minutes at room temperature to separate the plasma layer. 1mL aliquots of cell-free plasma is transferred into microcentrifuge tubes and centrifuged at 17000g for 5 minutes at room temperature (RT) to obtain cell debris-free, platelet-free plasma. For each sample, 335µL plasma is incubated with 2.68µL Thrombin (SBI) for 5 minutes at RT, then centrifuged at 10000rpm for 5 minutes at RT to pellet fibrin. 250µL fibrin-free plasma is transferred to a fresh microcentrifuge tube and incubated with 67µL ExoQuick (SBI) for 30 minutes at 4°C to precipitate EVs. After incubation, the plasma/ExoQuick mixture is centrifuged at 1500g for 30 minutes at 4°C to pellet EVs. The EV pellet is resuspended in 400µL sterile PBS and pipetted into a 0.22µm (220nm) filter chamber fitted in a microcentrifuge collection tube. The EV suspension is filtered by centrifugation at 1000g for 10 minutes at RT. Following centrifugation, the filters are discarded and 5µL Fc blocking solution is added to the EV suspension and incubated for 10 minutes at RT. After blocking, the EV suspension is transferred to a 5mL round-bottom polystyrene tube. The appropriate antibody cocktails are added to each sample and incubated for 30 minutes at 4°C, protected from light. 125µL 4% paraformaldehyde (PFA) in PBS is added to each sample for fixation to reach a total PFA concentration of 1%. Fixed, stained EV samples are analyzed on a BD FACSymphony A5 flow cytometer.

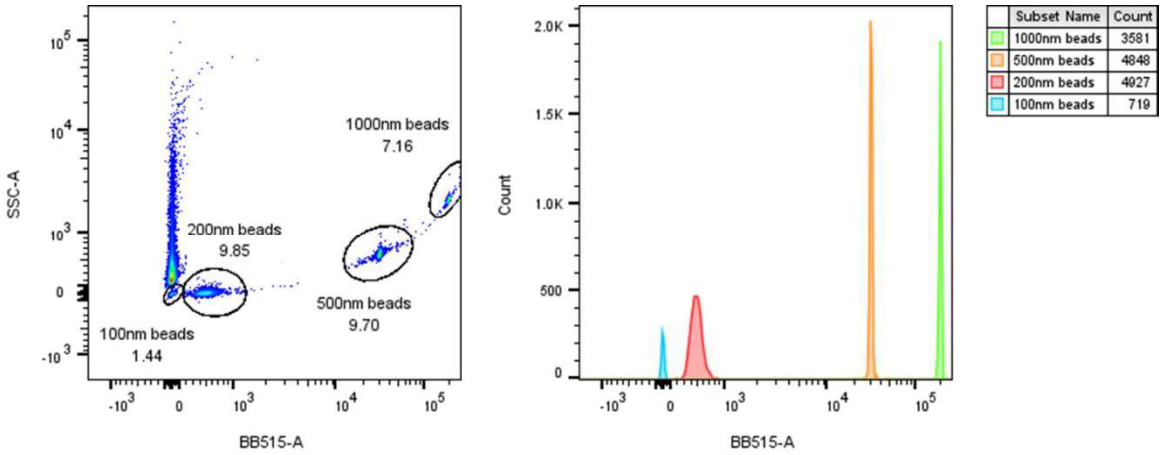

Figure 3.5. Sub-micron reference bead detection and SSC. 100nm, 200nm, 500nm, and 1000nm particle size reference bead populations were located by fluorescence intensity on the BB515 filter and side scatter area (SSC). Reference bead populations are shown in elliptical gates with the percentage of total events in each population (left). Total event counts by fluorescence intensity of each bead population are shown as 100nm: blue, 200nm: red, 500nm: orange, 1000nm: green (right). Event count peaks by fluorescence intensity and total subpopulation counts were calculated using FlowJo 10.9.0.

To calibrate, validate, and optimize this technique, several controls were used (166,170). FITC-conjugated sub-micron particle size reference beads (100nm, 200nm, 500nm, and 1000nm; Thermo Fisher Scientific) were used to approximate EV side scatter (SSC) and optimize flow rate and detection threshold (Figure 3.5). Reference bead size SSC can only be approximated, as polystyrene beads have different refractivity and complexity than EVs. Unstained EVs were used to generate EV forward scatter (FSC) and SSC gates, and a suspension of the antibody cocktail in PBS 1% PFA was run to ensure antibody aggregates were not creating false positive events (Figure 3.6). Additionally, a preparation of PEVs was treated with Triton X-100 detergent to lyse EV membranes.

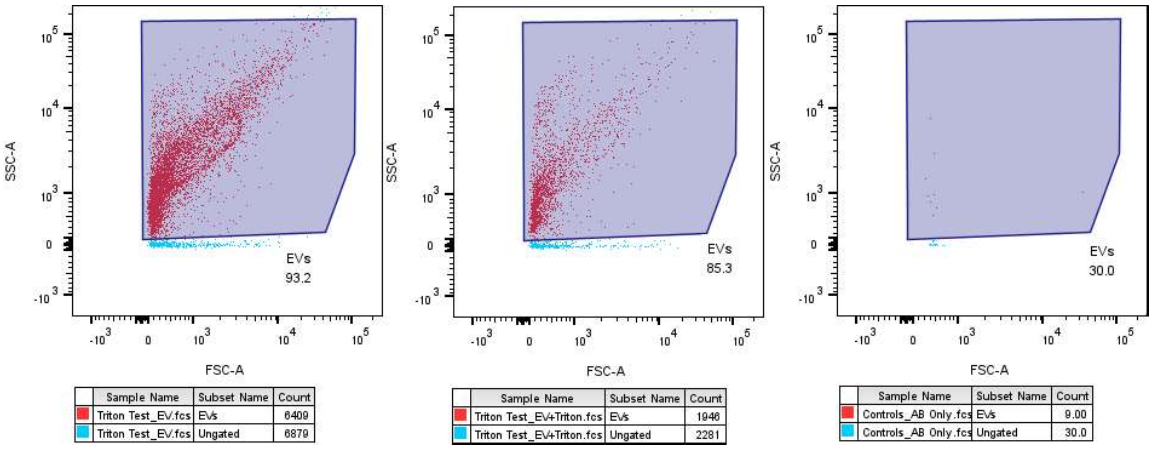

Figure 3.6. SSC/FSC gating on unstained EV control, lysed control, and antibody only control. An unstained EV control sample was used to determine baseline side scatter area/forward scatter area (SSC/FSC) gating (left). An unstained EV control treated with 1% Triton X-100 detergent to lyse EV membranes was recorded (center) and demonstrated a 70% reduction in EV events. A control sample containing only the antibody cocktail (Panel A + Panel B antibodies) suspended in sterile PBS 1% PFA was used to ensure antibody aggregates were not being recorded as false positive events (right). Events with appropriate EV SSC/FSC fall inside "EVs" subset gate (blue shading) and appear as red dots. Events outside "EVs" subset gate appear as blue dots and were excluded from compensation and analysis. The percentage of events falling inside EV gate is denoted in bottom right corners. Event counts, gating, and figure generation were performed using FlowJo 10.9.0.

When acquired for 5 minutes, the Triton X-100-treated sample demonstrated a 70% reduction in events compared to an untreated sample, which is consistent with the literature(168,171). Positive CD81+ gating was determined by comparing fluorescent intensity between FMO control and compensation control (Figure 3.7). For each parameter, the mean fluorescence intensity (MFI) of each channel was used to determine the relative abundance of CD81+ EVs expressing each marker. Each sample used for FMO and compensation controls was obtained from the same RM at the same timepoint to avoid the natural variation in EV profiles that occurs between animals and over time.

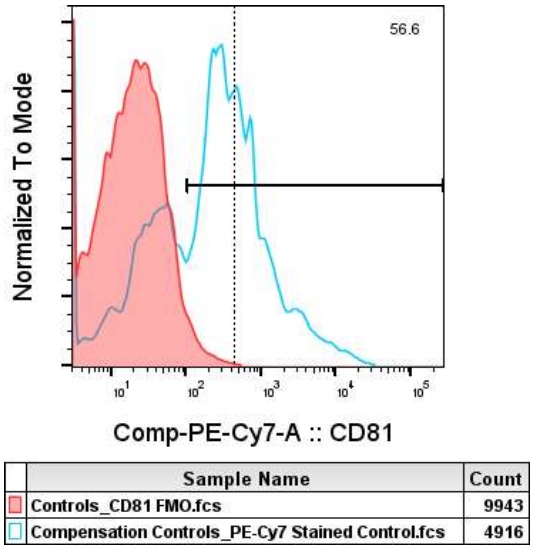

Figure 3.7. CD81+ EV gating. After setting EV side scatter area (SSC) and forward scatter area (FSC) gates, CD81+ positive signal gating (black horizontal line) was determined using single color compensation controls (blue outline) and FMO controls (red shading) in FlowJo 10.9.0. Percentage of CD81+ positive events in the compensation control sample is denoted in the top right corner (56.6% CD81+). Mean fluorescence intensity (MFI) of the positive subpopulation is represented by a vertical black dotted line.

Panels and Compensation Matrices

Two panels were developed to minimize signal spillover and increase detection of rare events (Table 3.2). Each panel contained three markers of cellular origin and one EV marker (tetraspanin CD81). RM plasma EVs isolated as described in Figure 3.4 were used for each single-color compensation control and fluorescence minus one (FMO) control. Single color compensation controls were used to optimize voltages and set compensation matrix parameters (Table 3.3). FMO controls, which contain each antibody in the panel except one, were used in conjunction with compensation controls to determine positive and negative gating. For each compensation control, 5,000 events were recorded. For each FMO control, 10,000 events were recorded.

Table 3.2. EV cellular origin marker panels A and B.

PANEL A			
Antibody	**Target**	**Fluorochrome**	**Channel**
CD11b	macrophage-EVs	BUV737	BUV737
CD14	monocyte-EVs	Pacific Blue	BV421
CD81	EVs (tetraspanin)	PE-Cy7	PE-Cy7
TMEM119	microglia-EVs	AlexaFluor 700	Alexa 700
PANEL B			
Antibody	**Target**	**Fluorochrome**	**Channel**
CD171	neuron-EVs	AlexaFluor 488	BB515
CD3	T lymphocyte-EVs	APC-Cy7	APC-Cy7
CD31	endothelium-EVs	BUV395	BUV395
CD81	EVs (tetraspanin)	PE-Cy7	PE-Cy7

Note. Two panels with minimal spectral spillover were developed using Spectra Viewer by FluoroFinder.com. APC: allophycocyanin, BUV: brilliant ultraviolet, Cy7: cyanine 7, PE: phycoerythrin, TMEM119: transmembrane protein 119.

Table 3.3. Compensation matrices of panels A and B.

Panel A					**Panel B**				
	AlexaFluor 700	BUV737	Pacific Blue	PE-Cy7		APC-Cy7	AlexaFluor 488	BUV395	PE-Cy7
AlexaFluor 700	X	12.881	1.009	0.716	APC-Cy7	X	0.089	0.052	33.244
BUV737	12.933	X	0.3053	0.085	AlexaFluor 488	0	X	1.89	0
Pacific Blue	0	0.172	X	0	BUV395	0	0.265	X	0
PE-Cy7	0.228	10.61	-0.4	X	PE-Cy7	12.218	13.392	20.305	X

Note. Compensation matrices were obtained using single color compensation EV sample controls for each parameter. Spectral overlap between fluorochromes was calculated using FlowJo 10.9.0. APC: allophycocyanin, BUV: brilliant ultraviolet, Cy7: cyanine 7, PE: phycoerythrin.

Microglia- and Neuron-Derived EVs are Significantly Increased During Viremia and ART Suppression

Plasma samples from RM before infection with SHIV.D, during viremia, and during ART induced viral suppression (Table 3.4) were prepared for each flow cytometry panel and sample acquisition and analyses were performed as described above. By repeated measures one-way ANOVA, we found that CD171+ neuron-derived EVs (P=0.01) and TMEM119 microglia-derived EVs (P=0.008) were significantly different between the three groups (Figure 3.8). Post-hoc paired t-tests revealed that neuronal CD171+ EVs are significantly increased in both viremic RM (P = 0.03, mean MFI = 1535) and ART-suppressed RM (P = 0.04, mean MFI = 1167) compared to those of RM before infection (mean MFI = 624.5).

Table 3.4. RM plasma samples used for EV isolation and analysis.

Group A (uninfected)	**Group B (acute viremia)**	**Group C (ART suppression)**
KM08 PRE-BLEED	KM08 DPI-11	KM08 DPI-167
JV72 PRE-BLEED	JV72 DPI-11	JV72 DPI-167
ML02 PRE-BLEED	ML02 DPI-11	ML02 DPI-167
MD86 PRE-BLEED	MD86 DPI-11	MD86 DPI-167
LB53 PRE-BLEED	LB53 DPI-11	LB53 DPI-167
KR39 PRE-BLEED	KR39 DPI-11	KR39 DPI-167
KH22 PRE-BLEED	KH22 DPI-11	KH22 DPI-167
KD48 PRE-BLEED	KD48 DPI-11	KD48 DPI-167
LI76 PRE-BLEED	LI76 DPI-11	LI76 DPI-167
MJ45 PRE-BLEED	MJ45 DPI-11	MJ45 DPI-167

ART: antiretroviral therapy, DPI: day post infection, EV: extracellular vesicle, RM: rhesus macaque.

Post-hoc paired t-tests comparing TMEM119+ microglial EV MFI also demonstrated a significant increase in viremic RM ($P < 0.05$, mean MFI = 285.6) and ART-suppressed RM ($P = 0.004$, mean MFI = 290.8) compared to pre-infection RM (mean MFI = 229.0). There were no differences between TMEM119+ or CD171+ EVs between viremic and ART suppression, so even with controlled ART these EV populations were elevated. While the average CD171 MFI between groups was highest in the viremic RM, average TMEM119 MFI was highest in the ART-suppressed RM. Though not statistically significant, CD11b pan myeloid/macrophage-derived EVs and CD3 T cell-derived EVs also showed an increase in average MFI during viremia and ART suppression compared to their pre-infection control samples (Figure 3.8).

Interim Discussion

Analysis of SHIV.D RM PEVs

Our significant findings of sustained increases in circulating neuron and microglia derived EVs during ART suppression are the first of their kind, due to the distinctive ability to investigate EV production before infection and over time in an NHP model of HIV. These findings reinforce the importance of EVs in HIV infection but lead to further questions about their roles. From these data alone, it is unknown if the increase in circulating microglial and neuronal EVs are due to an increase in their production, an intentional increase in their release into the periphery, or a result of BBB injury and increased permeability. Nevertheless, each of these possibilities demonstrate that EVs act as either a mediator of disease via cargo release or cell signaling, or a biomarker of ongoing neuropathogenesis.

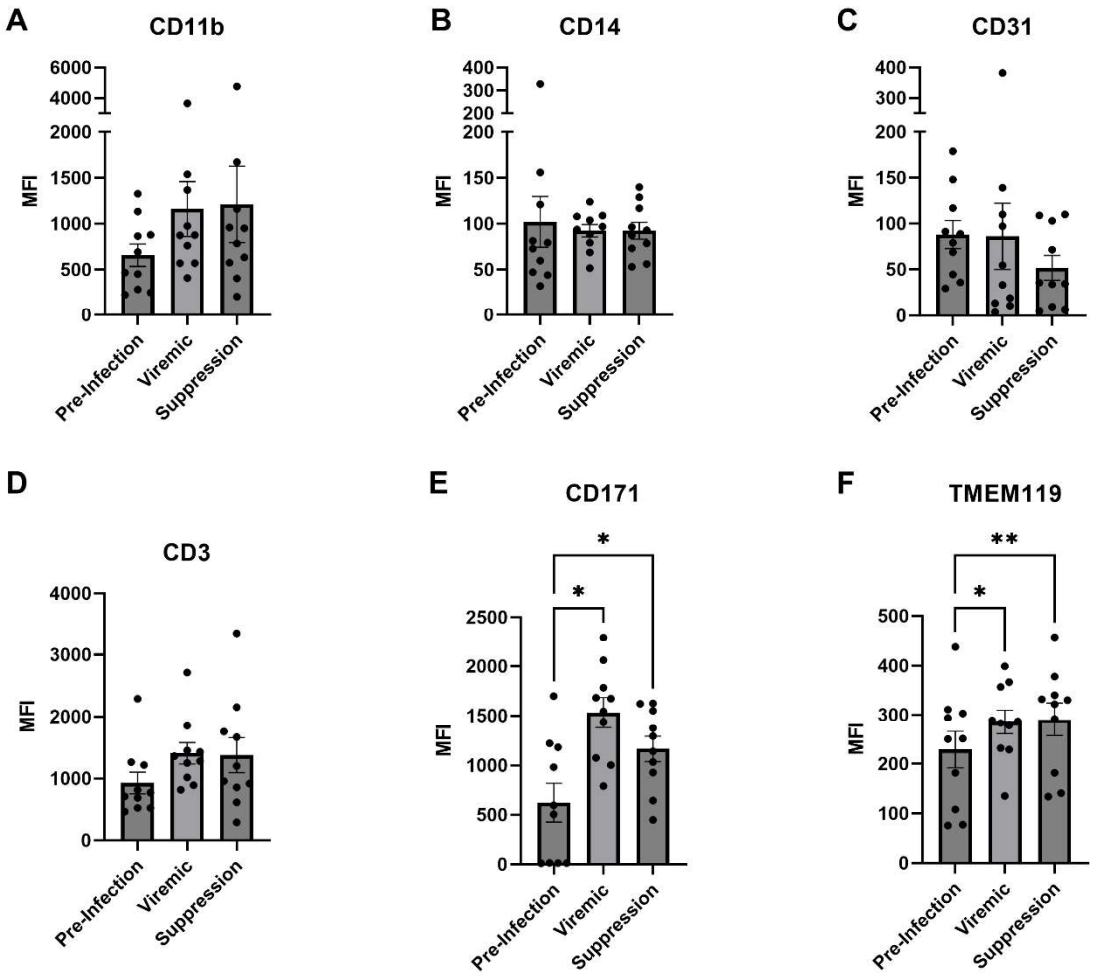

Figure 3.8. Neuronal and Microglial EVs are increased during viremia and ART suppression. (A) CD11b channel MFI of CD81+ EVs, (B) CD14 MFI, (C) CD31 MFI, (D) CD3 MFI, (E) CD171 channel MFI is significantly different between groups (ANOVA, P=0.01). MFI of viremic and ART-suppressed PEVs are both significantly increased compared to pre-infection (Tukey's multiple comparisons test). (F) TMEM119 channel MFI is significantly different between groups (ANOVA, P=0.008). MFI of viremic and ART-suppressed PEVs are both significantly increased compared to pre-infection (Tukey's multiple comparisons test). *= P<0.05, **=P<0.01. Repeated measures one-way ANOVA followed by post-hoc paired t-tests (Tukey's multiple comparisons). MFI: Mean fluorescence intensity.

Previous research has compared CD171+ neuron-derived EVs from PWH with and without cognitive impairments, and found no change in the number of EVs between these groups (172). However, the cargo of neuronal EVs has been demonstrated to contain proteins associated with neurodegeneration, inflammation, and neuronal injury (122,134,135,172). Our matched analysis of cell-specific EVs throughout the course of infection and treatment in the same RM is a more robust technique than unpaired analysis, but further research is necessary to determine if the sustained increase in neuronal and microglial EVs during ART suppression will be recapitulated in a larger study size, or in PWH. Interestingly, 4/10 uninfected RM produced no detectable CD171+ neuronal EVs. Of all parameters and groups tested, these were the only undetectable markers. This unique finding reinforces the importance of neuron-derived EVs in neurodegenerative disease states and demonstrates basis for further investigation into neuron-derived EVs and their cargo during HIV/SHIV infection and ART suppression.

Unlike CD171/L1CAM+ EVs, TMEM119+ microglial derived EVs are infrequently studied, and their relationship to HIV infection is novel. One study found a significant increase in circulating TMEM119+/CD14+ dual-positive EVs in rats after stroke (173). When TMEM119+/CD14+ dual-positive EVs were analyzed in our experiment, we found no difference between the groups. The significant increase in TMEM119+ EVs during acute infection and additional increase during ART suppression is a novel finding and indicates that microglial and other myeloid-derived EVs should be further investigated in the contexts of HIV and chronic neurological dysfunction.

Statistical analysis of each flow cytometry parameter data set revealed outliers by the ROUT method for outlier identification. Because the nature of these outliers is unknown, they were not excluded from the analysis. This decision likely decreased the statistical power of some analyses by increasing the variation between readings. The two statistically significant parameters by ANOVA, CD171+ and TMEM119+ EVs, had no outliers identified by the ROUT method.

There are limitations to this study. First, the use of RM tissue limited our choice of anti-human antibodies, and anti-monkey antibodies are limited. Some anti-human antibodies do not cross react with NHP receptors or lack sensitivity and were excluded from this study. Some more rare plasma EV populations, such as astrocyte-derived GFAP+ EVs, were lower than the quantity needed for accurate compensation and were excluded from this study. Finally, while the time- and cost-effective ExoQuick polymer-based EV precipitation method used has been reported to capture the greatest number of EVs in a sample compared with other isolation methods, it is also reported to result in lipoprotein and other small protein contamination in the EV sample (174). This is consistent with the detectible debris found in our Triton X-100 lysed control sample. Lastly, the use of CD81 as a "backbone" EV marker likely excluded many EVs from analysis, as not all EVs express all tetraspanins. CD81 was selected as our backbone EV marker because it was the most prevalent tetraspanin in our RM plasma EV samples, is expressed on more subsets of brain and immune cell derived EVs compared to CD63 and CD9, and is not frequently expressed by platelet-derived EVs (175,176). An EV-specific backbone filter is critical in flow cytometric analysis of plasma EVs, as lipoproteins are a common contaminant of EV

precipitations. Though lipoproteins can mimic EVs on NTA and unstained EV flow cytometry, they do not express tetraspanins and can be reliably excluded when gated on CD81+ (177,178).

EV Flow Cytometry

This is a novel application using a conventional flow cytometer/cell sorter to perform multiplex flow cytometry on bead-free sub-micron extracellular vesicles. Bead-free multiplex EV flow cytometry allows for quantification and analysis of multiple EV surface antigens at once. Additionally, multiple populations of EVs derived from specific cells of origin can be quantified using a single aliquot of plasma. EV-associated tetraspanins CD81 and CD63 are both readily detected using this method, but CD81 was more prevalent in our RM plasma EV samples and therefore was selected to use in both panels as internal control to maintain consistency. Additionally, CD81 is expressed on more subsets of brain and immune cell derived EVs, and is not commonly expressed on platelet-derived EVs (175,176). The markers of cellular origin were detected at expected frequencies relative to cell type of origin abundance and activity, and rare events such as CD171/L1CAM+ neuron-derived EVs are also detectable in the plasma (179).

At present, the majority of EV flow cytometry methods rely on capturing EVs on antibody- or streptavidin-coated beads to increase particle size for easier detection by conventional flow cytometers, or the use of laboratory-made or highly specialized nano-cytometry instruments optimized for detecting sub-micron particles (167,180–184). However, there are several limitations to these methods. Accurate EV quantification and phenotyping is impeded when multiple EVs are captured on a single bead (167,183). Total

capture of all EVs in a sample is hindered by tetraspanin CD63, CD9, or CD81 antibody-conjugated bead capture, as all EVs do not uniformly express these markers (175,185,186). Lastly, quantifiable single EV analysis of multiple surface markers is not possible with traditional bead-based EV flow cytometry. Bead-free EV flow cytometry offers several advantages. It is both time- and cost-effective and utilizes traditional commercially available antibodies for flow cytometry. It allows for detection and quantification of both tetraspanin EV markers and multiple membrane proteins in multiplex panels. Additionally, it increases the number of potentially detectable analytes in a single biofluid aliquot, critical for precious human samples and scarce small animal samples.

The aim of this study was to design a protocol that can be used to quantify subpopulations of different cell-derived EVs in the plasma that could give insight into difficult-to-assess disease processes, such as brain-derived EVs. For this reason, our parameters focus on brain and immune cell-derived EV surface markers. This protocol improves upon existing methods by combining plasma separation and defibrination, polymer-based EV precipitation, and nanoparticle filtration to enrich and purify the EV fraction. Through these enhancements, we detected a greater percentage of each EV subpopulation than similar methods. This protocol was developed in accordance with guidelines recommended by both the minimum information for studies of EVs (MISEV) framework and the minimum information about a flow cytometry experiment standard in an EV-specific framework (MIFlowCyt-EV) (166,170).

In summary, this is a novel and sensitive technique for multi-parameter plasma EV flow cytometry on a conventional flow cytometer. This protocol is useful for quantification

of several unique subsets of specific cell-derived EVs that are clinically and scientifically relevant during disease and injury. Though the samples in this study were macaque in origin, all antibodies and reagents used target human antigens, and we anticipate that this protocol will be effective using human PEVs as well. It is also scalable and adjustable to different organisms and EV populations of interest and allows subset sorting and downstream analysis. Finally, our results demonstrate that circulating brain-derived EV populations hold promise as biomarkers or mediators of sustained neuropathogenesis during treated HIV infection.

CHAPTER 4

MYELOID-DERIVED EXTRACELLULAR VESICLES ARE OVERPRODUCED DURING SHIV.D INFECTION AND CARRY PROTEIN MEDIATORS OF NEUROPATHOGENESIS

Chapter Abstract

Extracellular vesicles (EVs) have been identified as mediators of pathogenesis in several neurological diseases, including HIV-associated neurological dysfunction. Some populations, like CD171+ neuron-derived EVs, have been examined for cargo that may serve as biomarkers for HIV neuropathogenesis or drivers of CNS inflammation and toxicity. However, the protein cargo of myeloid EVs in HIV infection has not been described. In Chapter 3, we demonstrated that microglial EVs were significantly increased in the plasma of viremic RM infected with SHIV.D, and further increased during ART suppression. Here, we investigate myeloid EV production *in vitro* and conduct proteomic analysis on the cargo of EVs produced by uninfected or SHIV-infected monocyte-derived macrophages (MDM). We found that MDM significantly increased EV production after SHIV.D infection. From bioinformatics analysis of proteomics data, we found several significant changes in the protein profiles of SHIV-infected and uninfected MDM EVs. MEVs from SHIV+ cells carry protein mediators of inflammation, neuronal injury, and HIV pathogenesis including lipocalin-2 (LCN2), T Cell Immunoglobulin and Mucin Domain Containing 4 (TIMD4), insulin-like growth factor binding protein 1 (IGFB1), and indoleamine 2,3-dioxygenase 1 (IDO1) (187–195). Gene ontology and gene set enrichment analysis revealed the biological pathways overrepresented in EV-associated proteins.

Taken together, we found evidence that MEVs from SHIV+ myeloid cells perpetuate neuropathogenesis.

Materials and Methods

Primary Macrophage Culture and SHIV.D Infection

SHIV.D.191859 was cloned and viral stock was generated as previously described (81,90,91,196). Infectivity of the viral stock was calculated by serial stock dilution and infection of Ghost(3) reporter cells, which express GFP upon HIV/SIV-Tat activation of transcription, followed by GFP flow cytometry using Guava easyCyte (197). RM peripheral blood mononuclear cells (PBMCs) were isolated from EDTA whole blood using a Ficoll (Cytiva) gradient and plated in RPMI medium (Gibco) + 10% exosome-depleted FBS (Gibco) + gentamicin (Corning) across 6-well plates at a density of 1 million cells/mL. After 24hrs in culture, differentiation into monocyte-derived macrophages (MDM) was stimulated with 50ng/mL recombinant human macrophage colony stimulating factor (M-CSF [R&D Systems]). Half media changes with M-CSF were performed on days 4 and 7 after plating. On day 8, cells were washed 2X with PBS (Corning) and adherent macrophages were infected with SHIV.D.191859 viral stock at an MOI of 0.1-1.0 for 24 hours. Following 24 hours incubation with virus, infection media was removed, cells were washed 2X with PBS, and 2mL fresh working media (RPMI with 10% exosome-depleted FBS, gentamicin, and M-CSF) was added per well. Working media changes were performed every 24-48 hours after initial infection. Cell culture supernatant from each media change was centrifuged for 5 minutes at 1500rpm to remove cells and cellular debris, then stored at -80°C for downstream EV or vRNA isolation.

Immunocytochemistry

To validate differentiation of primary PBMC into mature myeloid cells, immunocytochemistry (ICC) for pan-macrophage marker CD68 was performed. Primary MDMs were fixed in-well with 4% PFA in PBS for 30 minutes at RT, then washed 3X with PBS. Following fixation, cells were permeabilized with PBST (0.1% Tween-20 [Fisher]) + 0.1% Triton-X100 (Acros Organics) for 15 minutes, then washed 3X 2 minutes with PBST. Blocking was performed with PBST + 2% BSA (Fisher) + 5% FBS (Gibco) for 30 minutes. Cells were incubated with anti-CD68 primary antibody (Dako M0814, 1:50) or mouse IgG negative isotype control (Dako, 1:50) diluted in blocking solution overnight at 4°C. Cells were then washed 3X 5 minutes with PBST and incubated with anti-mouse secondary antibody (Invitrogen A32744, 1:1000) for one hour at RT. Following secondary incubation, cells were washed 3X 5 minutes in PBST, then stained with DAPI (Akoya Biosciences, 1 drop:1mL PBST). Residual antibody, tween, and salts were removed with 2X 5 minutes PBS wash followed by 2X 5 minutes H_2O wash. Cover slips were fixed to plates using ProLong Gold Antifade Mountant (Fisher) for storage at 4°C and cells were imaged using Keyence BZ-X700 microscope.

qPCR and RT-qPCR

Productive SHIV.D infection of primary RM MDMs *in vitro* was validated by quantitative polymerase chain reaction (qPCR) of SHIV.D proviral DNA and reverse-transcription qPCR (RT-qPCR) of viral RNA isolated from cell culture supernatant. Double stranded DNA was isolated from pelleted MDMs using DNA miniprep kit (Zymo) and quantified using Qubit dsDNA BR Assay (Invitrogen). Viral RNA was isolated from

cell-free supernatant using QIAmp Viral RNA mini kit (Qiagen). Eluate was treated with RNase-free DNase I (Qiagen) for 10 minutes at 37°C, then heat inactivated for 15 minutes at 70°C. Following DNase treatment, RNA was purified using the Monarch RNA Cleanup kit (NEB). Purified RNA eluate was quantified by Nanodrop. Primers and probes were designed using Integrated DNA Technologies PrimerQuest tool (IDT) for RM housekeeping gene telomerase reverse transcriptase (*tert*) and SHIV.D *pol, gag,* and *env* and checked for specificity, dimers, and hairpins using MFEprimer 3.1 (iGeneTech). Primer and probe sequences used for SHIV.D are as follows (Table 4.1). qPCR was performed using Luna Universal qPCR Master Mix (New England Biolabs [NEB]) according to the manufacturer's recommendations at the following cycling conditions: 1 minute denaturation at 95°C, 40 cycles of denaturation (15 seconds at 95°C) and extension (30 seconds at 60°C), followed by plate reading.

Table 4.1. Primers and probes for SHIV.D/RM qPCR and RT-qPCR.

Target	**Forward primer**	**Reverse primer**	**Probe**
RM-*tert*	5'-GAG CTG AGA TTG TGC CCT TG-3'	5'-CCA TTT GCT CTC TGC TC-3'	5'-/5HEX/CCA GCA CAG ATC CTG GTC CCG T/3BHQ-1/-3'
SHIV-*pol*	5'-CAC TTA CCA GTT GAG AGG GAT G-3'	5'-CTT ACT AGT GGT GGT GTT GAG ATA A-3'	5'-/56-FAM/ACC TGC CAA /ZEN/TAG TCT GTC CAC CAC /3IABkFQ/-3'
SHIV-*gag*	5'-GAA AGC CTG TTG GAG AAC AAA G-3'	5'-CCA GAT GAC GCA GAC AGT ATT A-3'	5'-/56-FAM/TAG CTC CAT /ZEN/TAG TGC CAA CAG GCT /3IABkFQ/-3'
SHIV-*env*	5'-CCA CCA AGG CAA AGA GAA GA-3'	5'-CTT CCT GCT GTT CCC AAG AA-3'	5'-/56-FAM/AGA GCA ATA /ZEN/GGA CTA GGA GCC CTG T/3IABkFQ/-3'

RT-qPCR was performed using Luna Universal One-Step RT-qPCR Kit (NEB) according to the manufacturer's recommendations at the following cycling conditions: 10 minutes reverse transcription at 55°C, 1 minute denaturation at 95°C, 40 cycles of denaturation (10 seconds at 95°C) and extension (30 seconds at 60°C), followed by plate reading. qPCR and RT-qPCR reactions were run on a Roche LightCycler 96 and analyzed on LC96 v. 1.1.0.1320.

MDM EV Isolation

EVs were isolated from the cell culture supernatant of primary myeloid cells *in vitro.* Supernatant was collected and centrifuged as described above. Cell free supernatant was incubated with ExoQuick-TC (SBI) at a ratio of 5mL supernatant:1mL ExoQuick overnight at 4°C. Following incubation, EV/ExoQuick mixtures were centrifuged for 10 minutes at 3000g to pellet EVs for downstream applications. Centrifugation was repeated if necessary to remove residual ExoQuick and cell culture media.

EV Infectivity Assay

Ghost (3) (G [3]) reporter cells, which express GFP upon HIV/SIV-Tat activation of transcription, were cultured for 5 days in selection media (DMEM [Gibco] 10% FBS [Gibco] with puromycin, Hygromycin B [Invitrogen], and G418 geneticin [Gibco]) and maintained in DMEM supplemented with 10% FBS (Gibco) and gentamicin (Corning). Primary MDMs were differentiated and infected as previously described. EVs were isolated from uninfected MDM and SHIV+ MDM and counted using ZetaView NTA. EVs suspended in sterile PBS were added to plated G (3) cells in maintenance media at a concentration of 500 EVs/cell in triplicate. As a positive control, G (3) cells were infected

with SHIV.D at an MOI of 0.5 in triplicate. After 24hr, G (3) cells were collected for flow cytometry and DNA lysis. For GFP flow cytometry, cells were pelleted and resuspended in PBS with 2% PFA. GFP+ cells were counted using Guava easyCyte. Cell pellets were lysed for SHIV DNA qPCR and DNA extraction was performed using DNA miniprep kit (Zymo). Double stranded DNA was quantified using Qubit dsDNA BR Assay (Invitrogen). qPCR was performed and analyzed as described above.

ZetaView Nanoparticle Tracking

Isolated EV size distribution and concentration was measured using ZetaView nanoparticle tracker and analysis software (version 8.05.12 SP2; Particle Metrix). The instrument was calibrated before analysis using 100nm polystyrene standard particles (Life Technologies) for autoalignment and cleaned with sterile PBS and dH_2O. EV suspensions were diluted to optimal NTA concentration (50-300 particles/frame) in sterile PBS and 2mL of each sample was injected into the instrument for recording. Between each sample recording, the instrument was flushed with PBS until <5 particles were detected. NTA video was captured at sensitivity = 85, shutter speed = 100, and frame rate = 30f/s. 12 positions were traced for analysis. To account for increased cell death and decreased proliferation in the SHIV.D-infected cells, total EV concentration/mL was normalized for all samples by dividing EV concentration/mL by the qPCR endpoint fluorescence of housekeeping gene RM *tert* cellular DNA (198).

EV Marker Detection Arrays

Macrophage EVs (MEV) were pelleted using ExoQuick-TC as previously described and lysed using Exo-Check Exosome Antibody Array lysis buffer (SBI).

Following lysis, protein concentration was measured on a BioTek Cytation 1 microplate reader (Agilent) using Pierce 660nm Protein Assay Reagent (Thermo Scientific). 50µg protein lysate was incubated with Exo-Check Exosome Antibody Arrays (SBI) according to the manufacturer's instructions. Arrays were developed with SuperSignal™ West Femto Maximum Sensitivity Substrate (Thermo Fisher) for 5 minutes at room temperature and imaged using an iBright FL1000 imaging system (Invitrogen).

Statistics and Analyses

Comparisons and statistical analyses were performed using GraphPad Prism V9.4.1. For MEV NTA data set, the N value was insufficient to determine normal distribution by the D'Agostino-Pearson test. Therefore, nonparametric Wilcoxon matched-pairs signed rank tests were used to compare groups. Descriptive statistics were also calculated for each group. NTA graphs display individual values. In bar graphs representing PCR and flow cytometry data, the bar represents the mean value of technical replicates. Error bars represent the standard error of the mean.

Protein Extraction for Mass Spectrometry

Protein extraction for mass spectrometry (MS), MS, and subsequent bioinformatics analysis was performed by the University of Pennsylvania/Children's Hospital of Philadelphia Proteomics Core (Philadelphia, PA). EV pellets were solubilized in 50µL of extraction buffer containing 5% sodium dodecyl sulfate (SDS, Affymetrix), 50mM TEAB (pH 8.5, Sigma), and protease inhibitor cocktail (Roche complete, EDTA free). To shear DNA and ensure complete solubilization, samples were sonicated for 10 minutes at 20°C in a Covaris R230 focused-ultrasonicator with the following settings: Dithering: Y=3.0,

Speed=20.0, peak incidence power: 360.0, duty factor: 30, cycles per burst: 200. Samples were centrifuged at 3000g for 10 minutes to clarify lysate. Protein concentration was determined by intrinsic tryptophan fluorescence, excited at 280nm and read at 350nm, against an in-house generated E. coli lysate standard curve on a Synergy H1 microplate reader (BioTek).

In-Solution Digestion

10µg of each sample was digested per the S-Trap Micro (Protifi) manufacturer's protocol (199). Briefly, proteins were reduced in 5mM TCEP (Thermo), alkylated in 20mM iodoacetamide (Sigma), then acidified with phosphoric acid (Aldrich) to a final concentration of 1.2%. Samples were diluted with 90% methanol (Fisher) in 100 mM TEAB, then loaded onto an S-trap column and washed three times with 90% methanol in 100 mM TEAB. A 1:10 ratio (enzyme: protein) of Trypsin (Promega) and LysC (Wako) suspended in 20µL 50mM TEAB was added, and samples were digested for 18 hours at 37°C in a humidity chamber. After incubation, peptides were eluted with an additional 40µL of 50 mM TEAB, followed by 40µL of 0.1% trifluoroacetic acid (TFA) (Pierce) in water, and finally 40µL of 50/50 acetonitrile: water (Fisher) in 0.1% TFA. Eluates were combined and organic solvent was dried off via vacuum centrifugation. Samples were then desalted using an Oasis HLB µElution plate (30um, Waters). Wells were conditioned two times with 200µL of acetonitrile and equilibrated three times with 200µL of 0.1% TFA. Samples were applied, washed three times with 200µL 0.1% TFA, and eluted directly into autosampler vials in three increments of 65µL of 50:50 acetonitrile: water. Eluates were then dried by vacuum centrifugation and reconstituted in 0.1% TFA containing iRT

peptides (Biognosys, Schlieren, Switzerland). Peptide concentration was determined at OD280 using a Synergy H1 microplate reader (BioTek), and samples were adjusted to 400ng/µL for injection.

Mass Spectrometry Data Acquisition

Samples were randomized and analyzed on an Exploris 480 mass spectrometer (Thermo Fisher Scientific San Jose, CA) coupled with an Ultimate 3000 nano UPLC system and an EasySpray source. 5µl of sample was loaded onto an Acclaim PepMap 100 75µm x 2cm trap column (Thermo) at 5uL/min and separated by reverse phase (RP)-HPLC on a nanocapillary column, 75µm id × 50cm 2um PepMap RSLC C18 column (Thermo). Mobile phase A consisted of 0.1% formic acid and mobile phase B of 0.1% formic acid/acetonitrile. Peptides were eluted into the mass spectrometer at 300nL/min with each RP-LC run comprising a 105-minute gradient from 3% B to 45% B.

Data independent acquisition (DIA) mass spectrometer settings were as follows: one full MS scan at 120,000 resolution, with a scan range of 350-1200 m/z and normalized automatic gain control (AGC) target of 300%, and automatic maximum inject time. This was followed by variable (DIA) isolation windows, MS2 scans at 30,000 resolution, a normalized AGC target of 1000%, and automatic injection time. The default charge state was 3, the first mass was fixed at 250 m/z, and the normalized collision energy for each window was set at 27.

Quality Analysis/Quality Control (QA/QC) and System Suitability

The suitability of Exploris 480 instrument was monitored using QuiC software (Biognosys; Schlieren, Switzerland) for the analysis of the spiked-in iRT peptides. As a

measure for quality control, we injected standard E. coli protein digest in between samples (one injection after every four biological samples) and collected the data in data dependent acquisition (DDA) mode. The collected DDA data were analyzed in MaxQuant (200) and the output was subsequently visualized using the PTXQC (201) package to track the quality of the instrumentation.

Database Searching

The DIA raw files were processed using Spectronaut 18.7 in direct DIA mode (202). We utilized a RM database comprising canonical and reviewed isoforms from UniProt, supplemented with a list of 245 common protein contaminants and iRT peptides. Enzyme specificity was set to trypsin with allowance for two potential missed cleavages. Fixed modification was specified as carbamidomethyl of cysteine, while protein N-terminal acetylation and oxidation of methionine were considered variable modifications. To ensure high confidence, a false discovery rate limit of 1% was applied for precursors, peptides, and proteins identification, while the remaining search parameters were maintained at their default settings.

Bioinformatics Analysis for Proteomics

Proteomics data processing and statistical analysis were conducted in R. The MS2 intensity values generated by Spectronaut were utilized for analyzing the entire proteome dataset. The data underwent log2 transformation and normalization by subtracting the median value for each sample. To ensure data integrity, we filtered it to retain only proteins with complete values in at least one cohort. To compare proteomics data across groups, we employed a Limma paired t-test to identify proteins with differential abundance, and we

visualized the impact of these differences through volcano plots. Lists of differentially abundant proteins were generated based on criteria of P value <0.05, resulting in a prioritized list for subsequent bioinformatics analysis.

Results

Characterization of MEVs

Following differentiation, MDM express tissue macrophage marker CD68 and display typical elongated M2 morphology (203,204)(Figure 4.1A-B). MDM infection with SHIV.D resulted in production of viral RNA in the cell culture supernatant, as well as the presence of proviral DNA in the cells (Figure 4.1C). Pooled MEVs express markers CD63, ANXA5, TSG101, FLOT1, ICAM, ALIX, and CD81 at higher intensity than cellular protein control GM130 (Figure 4.1D). NTA revealed nanoparticles of appropriate size (Figure 4.1E).

MEVs are Differentially Produced During SHIV.D Infection

MEV concentration determined by NTA normalized to RM *tert* endpoint fluorescence (EPF) demonstrated a significant increase in MEV production in the SHIV+ MDM (P=0.0313, n=6) (Figure 4.2). In uninfected MDM, the average (arithmetic mean) EV concentration relative to RM tert expression was 8.77e8 EVs/mL. From SHIV.D+ RM, the average EV concentration was 1.82e9 EVs/mL. From SHIV.D+ RM, the average EV concentration was 1.82e9 EVs/mL. There was no change in EV size between SHIV.D-/+ groups (Figure 4.2). The average median MEV diameter was 128.5nm from uninfected MDM and 127.6nm from SHIV.D+ MDM. Average mean MEV diameter was 143.6nm in uninfected cells and 141.4nm in viremic cells.

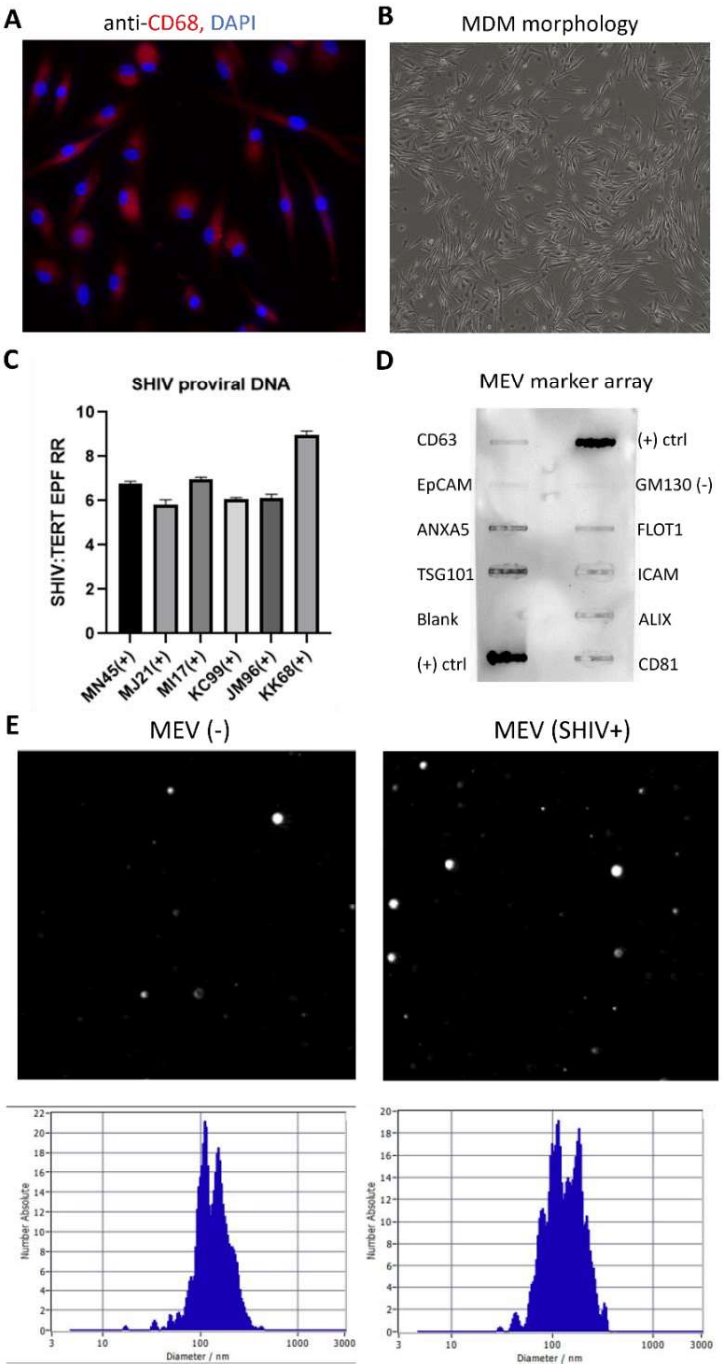

Figure 4.1: Characterization of MEVs. (A) Primary RM MDM express tissue macrophage marker CD68 (red). (B) MDM display elongated morphology *in vitro.* (C) MDM infected with SHIV.D contain proviral DNA. (D) MEV express EV markers CD63, ANXA5, TSG101, FLOT1, ICAM, ALIX, and CD81. (E) Representative images from NTA (top) and EV diameter histograms (bottom) from uninfected and infected MDM EV.

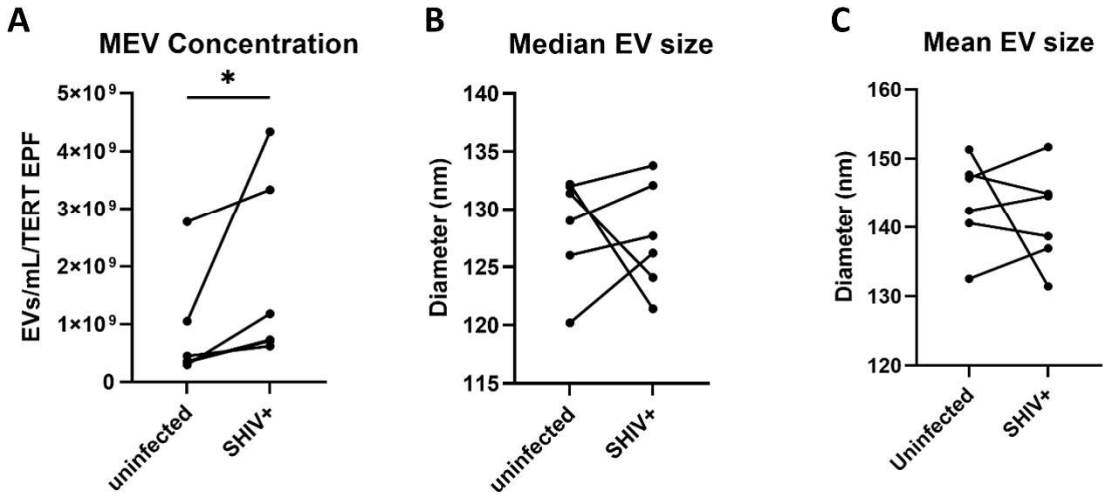

Figure 4.2. MEV production is significantly increased during SHIV.D infection. (A) MEV concentration (EVs/mL) normalized to RM TERT endpoint fluorescence (EPF) is significantly increased in SHIV.D+ MDM (Wilcoxon paired t-test, P=0.0313, N=6). There was no difference median (B) or mean (C) in EV size.

Reporter cell treatment with MEV from SHIV-/+ MDM demonstrated that EVs isolated from SHIV-infected cells do not contain competent virions and are not infectious themselves (Figure 4.3). qPCR did not detect SHIV proviral in cells treated with SHIV+ MEV, and reporter cells did not yield GFP expression above baseline (Figure 4.3).

MEV Protein Cargo is Significantly Changed With SHIV.D Infection

Primary MDM were differentiated from the PBMCs of 6 healthy RM, and half of the MDMs from each RM were infected with SHIV.D at an MOI of 1 (Table 4.2). 10mL of pooled cell culture supernatant from DPI 2-8 was harvested at the same time from SHIV.D-/+ MDM and used for EV isolation and proteomic analysis as described above. In analysis, proteins that were detected in at least 4 of the 6 replicates of at least one condition were included.

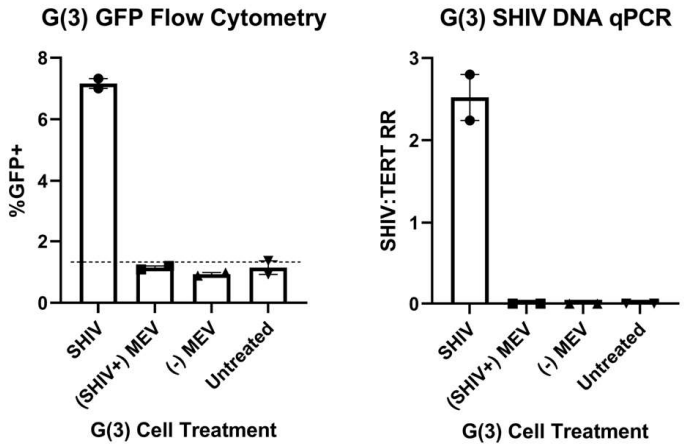

Figure 4.3. EVs isolated from SHIV.D+ MDM are not infectious. Flow cytometry for GFP indicating SHIV infection (left) indicated no GFP expression above baseline untreated expression (dotted horizontal line) in Ghost (3) (G [3]) reporter cells treated with SHIV+ MEV. Proviral SHIV DNA was absent in G (3) cells treated with SHIV+ MEV (right).

Table 4.2. Primary RM MDM for EV proteomics.

Uninfected	**SHIV.D+**
KC99- (UNINF_1)	KC99+ (SHIV_1)
MC43- (UNINF_2)	MC43+ (SHIV_2)
MM90- (UNINF_3)	MM90+ (SHIV_3)
JM96- (UNINF_4)	JM96+ (SHIV_4)
KB56- (UNINF_5)	KB56+ (SHIV_5)
MJ21- (UNINF_6)	MJ21+ (SHIV_6)

Note. RM PBMC donors, conditions, and identifiers for proteomic analysis. RM: rhesus macaque, MDM: monocyte-derived macrophage, PBMC: peripheral blood mononuclear cell, EV: extracellular vesicle, UNINF: uninfected, SHIV: simian-human immunodeficiency virus (D).

Quantification of filtered identified an average (arithmetic mean) of 1739 proteins per sample in the SHIV.D+ condition and 1907 proteins per sample in the uninfected condition (Figure 4.4A). 2094 of the total proteins identified and qualified for analysis were present

in both conditions (Figure 4.4B). 25 proteins were found only in the uninfected cohort, and 2 proteins were exclusive to the SHIV.D+ cohort (Figure 4.4B, Table 4.3).

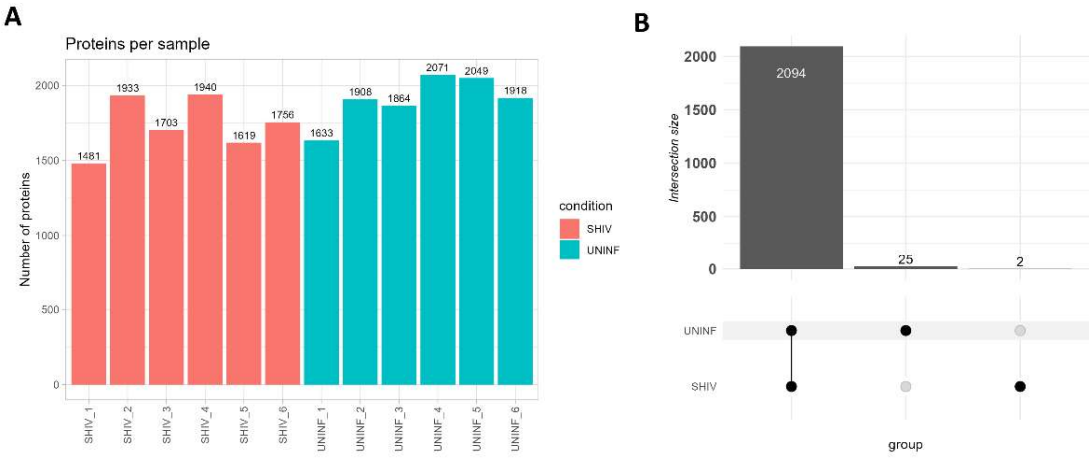

Figure 4.4. Proteins per sample and condition exclusive proteins. (A) Number of proteins detected in each sample after removal of proteins that were found in fewer than 4/6 samples per condition. (B) Number of proteins detected in 4/6 samples in both conditions (2094), UNINF only (25), and SHIV only (2).

Table 4.3. UniProt GeneID proteins exclusive to each condition.

Exclusive to UNINF	**Exclusive to UNINF (cont.)**	**Exclusive to SHIV**
AIFM1	LOXL3	HMGN3
ASPH	LYVE1	TIMD4
BAG5	MANBA	
CCDC126	MGAT4A	
CD151	SDF2L1	
CYBRD1	SIPA1	
EIF2B2	ST8SIA4	
EIF4EBP2	STAT5A	
GLDN	TMEM97	
GNPTAB	TRIM47	
GPR107	TSPAN33	
IGFBPL1	VTA1	
ITGAX.1		

Data were prepared by log2 transformation, filtering, normalization, and data imputation for correlation analysis, principal component analysis (PCA), differential abundance analysis, overrepresentation analysis, and gene set enrichment analysis (GSEA). Correlation analysis generally demonstrated stronger correlation between samples of the same condition as well as between SHIV.D-/+ samples from the same donor RM (Figure 4.5A). PCA compares the variances in peptide makeup of each sample in a two-dimensional plot of the two most significant principal components.

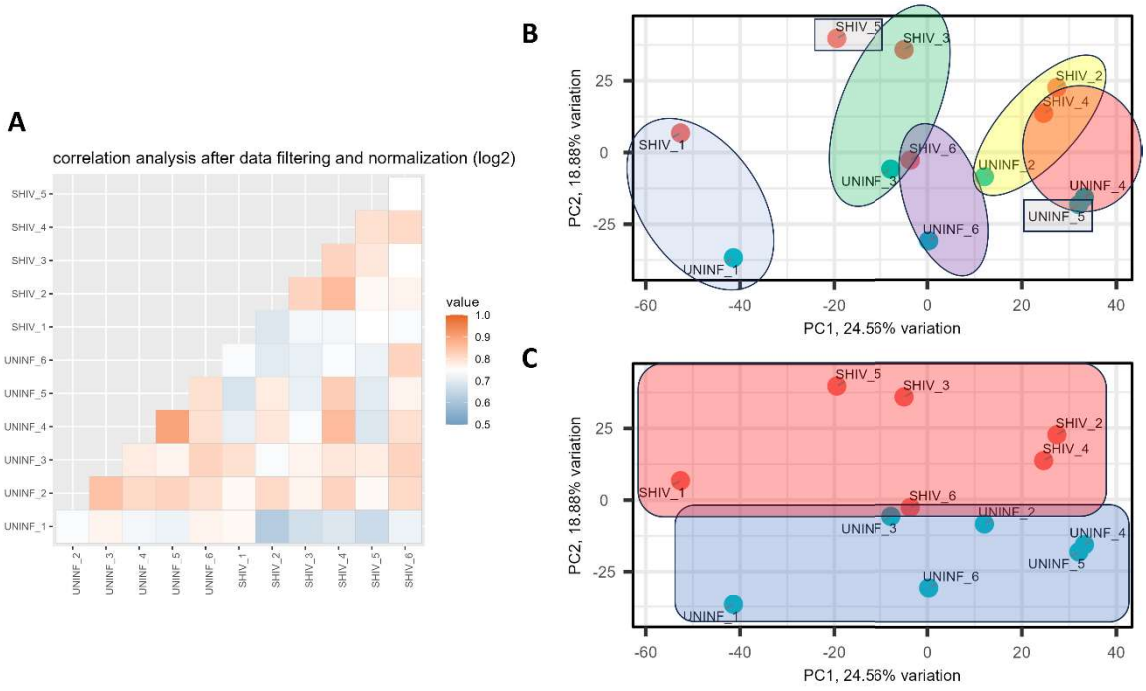

Figure 4.5. Correlation analysis and PCA. (A) Correlation between samples after data filtering and normalization. Orange tones indicate a higher level of correlation than blue tones. (B) Two-dimensional PCA plot of the first two principal components with ellipses indicating clustering between paired samples from the same RM donor. (C) PCA plot with rectangles indicating clustering between samples of the same condition. SHIV+ samples are highlighted in red, and uninfected samples are highlighted in blue.

PCA analysis shows that generally, samples from the same RM donor cluster together (Figure 4.5B), as do samples from the same condition (Figure 4.5C). Differential abundance analysis was performed as described comparing the SHIV condition to the uninfected condition (UNINF). The most significantly differentially abundant peptides are described (Table 4.4) and plotted by normalized intensity in each condition (Figure 4.6).

Table 4.4. Significantly differently abundant proteins between conditions.

Gene	logFC	AvgExpr	t	P value	adj.P value	B
LCN2	3.655438	-0.547926	9.4125355	0.0000205	0.0285549	3.287348
PLEKHB2	-3.190891	-0.8254686	-8.730479	0.0000346	0.0285549	2.8399919
MMP7	-3.363916	-0.2085002	-8.535004	0.0000404	0.0285549	2.704196
COCH	-2.635825	0.6983779	-7.866633	0.0000704	0.0307947	2.2102459
LDLR	-1.95001	2.0987059	-7.831565	0.0000726	0.0307947	2.183
SNRPA	-2.572535	-2.1176433	-7.47828	0.0000991	0.0327808	1.9006804
CD36	-2.476447	-0.4186557	-7.380335	0.0001082	0.0327808	1.8198191
CD63	-1.846775	2.2530424	-6.9303935	0.0001641	0.0404983	1.4336796
PRCP	-1.624058	0.0601066	-6.845243	0.0001781	0.0404983	1.3571346
COLEC12	-2.452713	0.7369188	-6.763647	0.0001927	0.0404983	1.2833531
RALA	-1.70828	-2.9713985	-6.675185	0.00021	0.0404983	1.2023623
ITGAX	-1.472674	2.3712421	-6.535937	0.0002409	0.0425833	1.0727348
ARRDC1	-1.769798	1.0675878	-6.249813	0.0003216	0.0471465	0.7979477
HTRA1	-1.348342	3.6647814	-6.157305	0.0003538	0.0471465	0.706618
ITGB2	-1.47168	3.6831326	-6.01934	0.0004087	0.0471465	0.5680996
HMGN3	3.866067	-2.0630072	5.949581	0.00044	0.0471465	0.4969932
WDR83OS	-4.266097	-0.9657041	-5.871243	0.0004783	0.0471465	0.4162768
LPL	-2.151474	5.357892	-5.823097	0.0005037	0.0471465	0.3662111
CD53	-1.401456	1.8475491	-5.814905	0.0005082	0.0471465	0.3576577
MRC1	-2.39218	4.6909445	-5.794167	0.0005197	0.0471465	0.3359531

Gene: UniProt GeneID, logFC: log2 fold-change, t: t-statistic, P value: raw P value, adj.P value: adjusted P value (q-value), B: log-odds that the gene is differentially expressed.

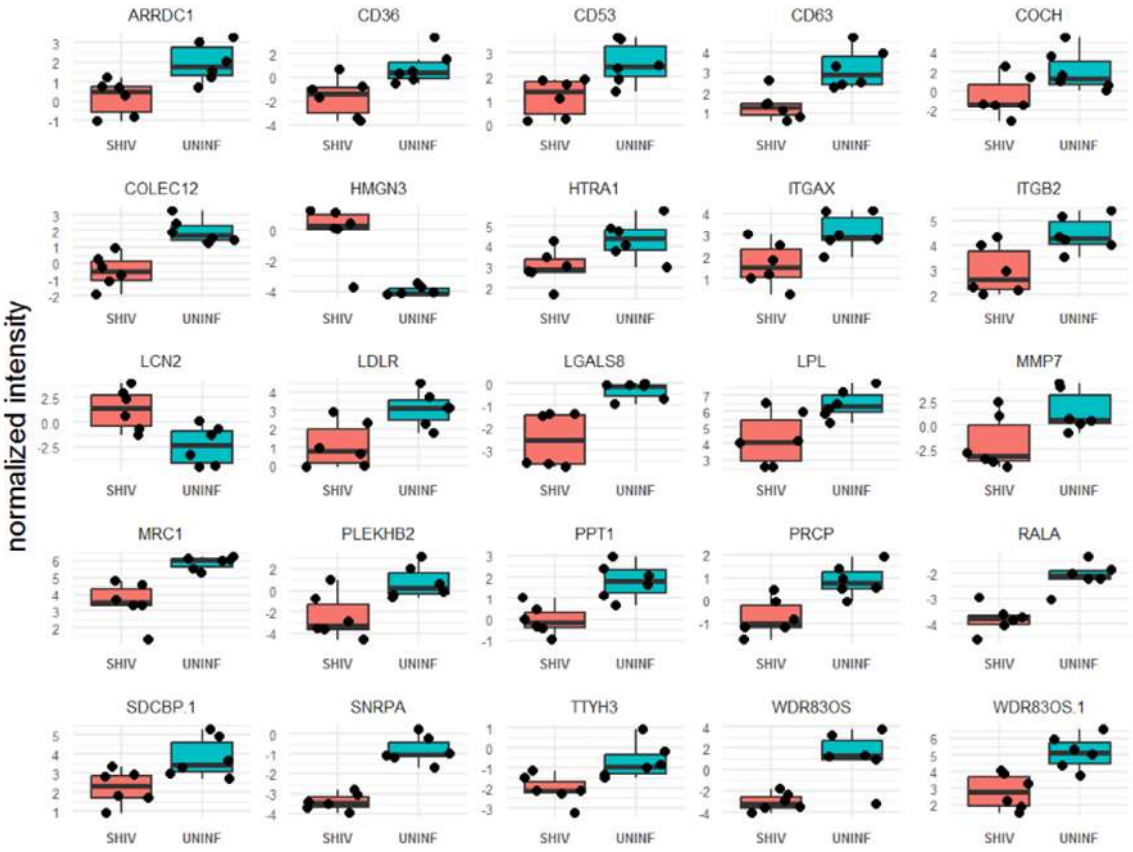

Figure 4.6: Normalized intensities of differentially abundant proteins between conditions. Normalized intensity of each significantly differentially abundant protein in each sample was plotted to compare affected proteins in UNINF (blue) and SHIV (red) conditions.

Only 2 of the 25 most significantly differentially abundant proteins were upregulated in the SHIV condition: lipocalin-2 (LCN2) and high mobility group nucleosome-binding domain-containing protein 3 (HMGN3) (Figure 4.6). A volcano plot was generated to visualize differentially abundant proteins between groups by log2 fold change and P value (Figure 4.7).

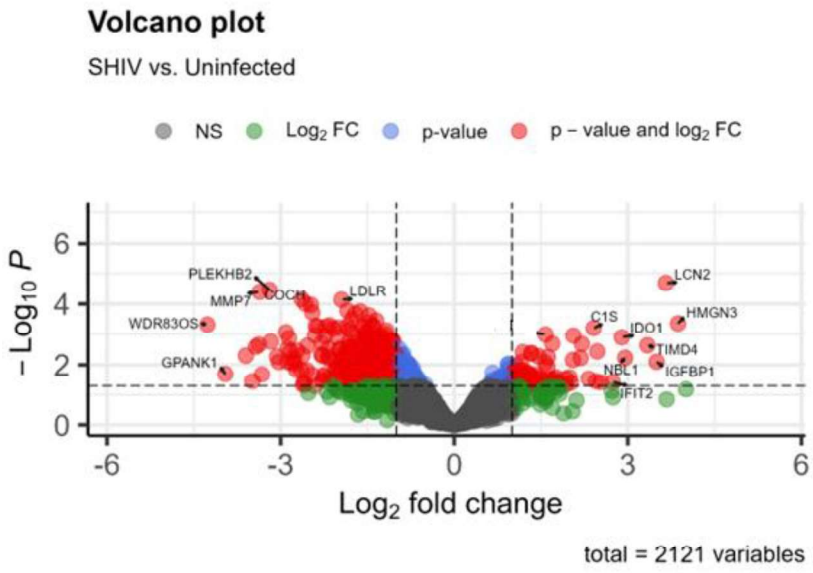

Figure 4.7. Volcano plot of differentially abundant proteins. Differentially abundant proteins are plotted by log2 fold change (FC) of SHIV vs. Uninfected conditions. Proteins that are significant by P value ($P<0.05$) and log2 FC are denoted in red. Green: log2 FC only, blue: P value only, grey: not significant (ns).

With LCN2 and HMGN3, other significantly overabundant proteins in SHIV EVs include T Cell Immunoglobulin and Mucin Domain Containing 4 (TIMD4), neuroblastoma suppressor of tumorigenicity 1 (NBL1), insulin-like growth factor binding protein 1 (IGFB1), and indoleamine 2,3-dioxygenase 1 (IDO1). Proteins with a significant negative fold change in a SHIV vs. UNINF comparison are differentially overabundant in the UNINF EVs. Differential abundance analysis identified a greater number of overrepresented proteins in the UNINF condition overall. Lastly before pathway analysis, 437 significant proteins were organized in a heatmap, where unbiased relational protein clustering was observed between SHIV and UNINF groups (Figure 4.8).

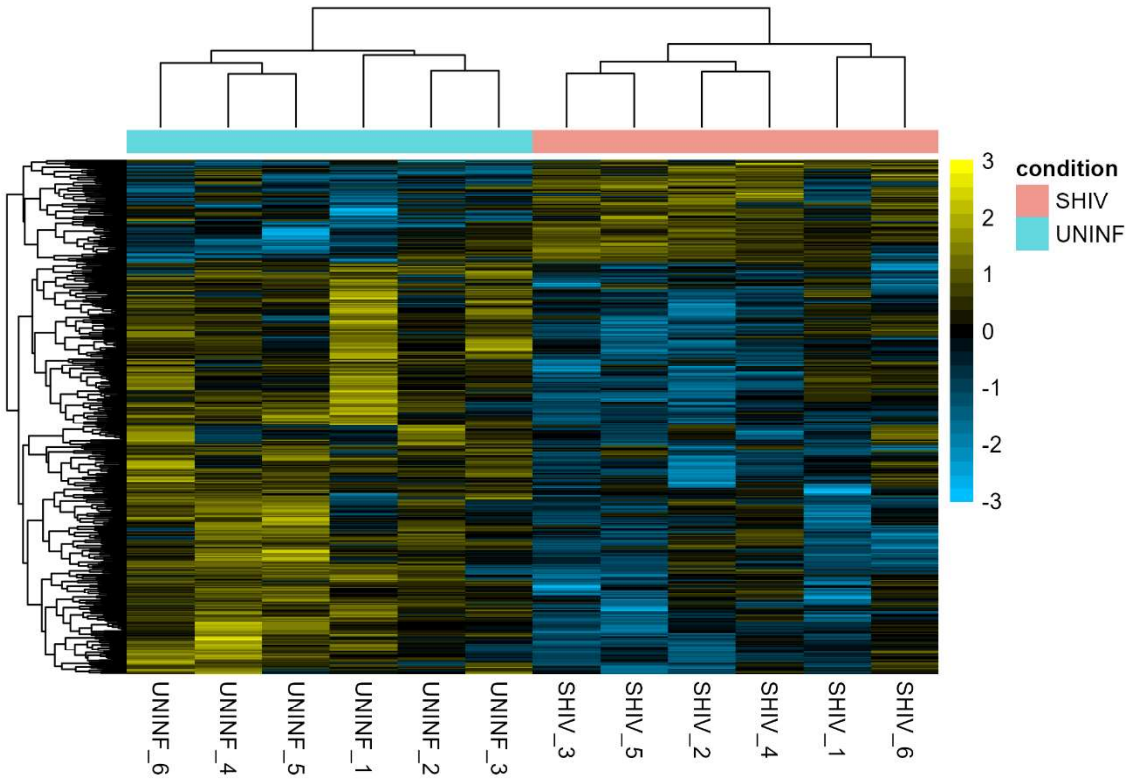

Figure 4.8. Heatmap of total significant proteins. An annotated heatmap clusters samples by fold change of significant proteins. The heatmap generated demonstrates clustering by condition.

Gene Ontology Pathway and Component Associations of EV Proteins

The proteins associated with specific biological processes (BP), cellular components (CC), and molecular functions (MF) were identified using a gene ontology database. A P value cutoff of <0.0005 was used to generate a list of genes of interest. Gene ontology analysis identified the BP, CC, and MF associated with the most significantly differentially abundant proteins between conditions (Figure 4.9). Of the BP pathways, proteins associated with vesicle-mediated transport, endocytosis, receptor-mediated endocytosis, and receptor internalization were the most abundant and most significantly

different. Proteins associated with positive regulation of reactive oxygen species (ROS) were also represented. Of CC, membrane, vacuole, and lysosome components were overrepresented. Of MF, signaling receptor binding was the most abundant pathway. Other signaling and receptor activity, cytokine activity, and cargo receptor activity were also MF pathways of proteins differentially abundant among MEVs. Proteins associated with glycosaminoglycan catabolic processes and glycosyl bond hydrolysis pathways were also overrepresented among the significant data (Figure 4.9).

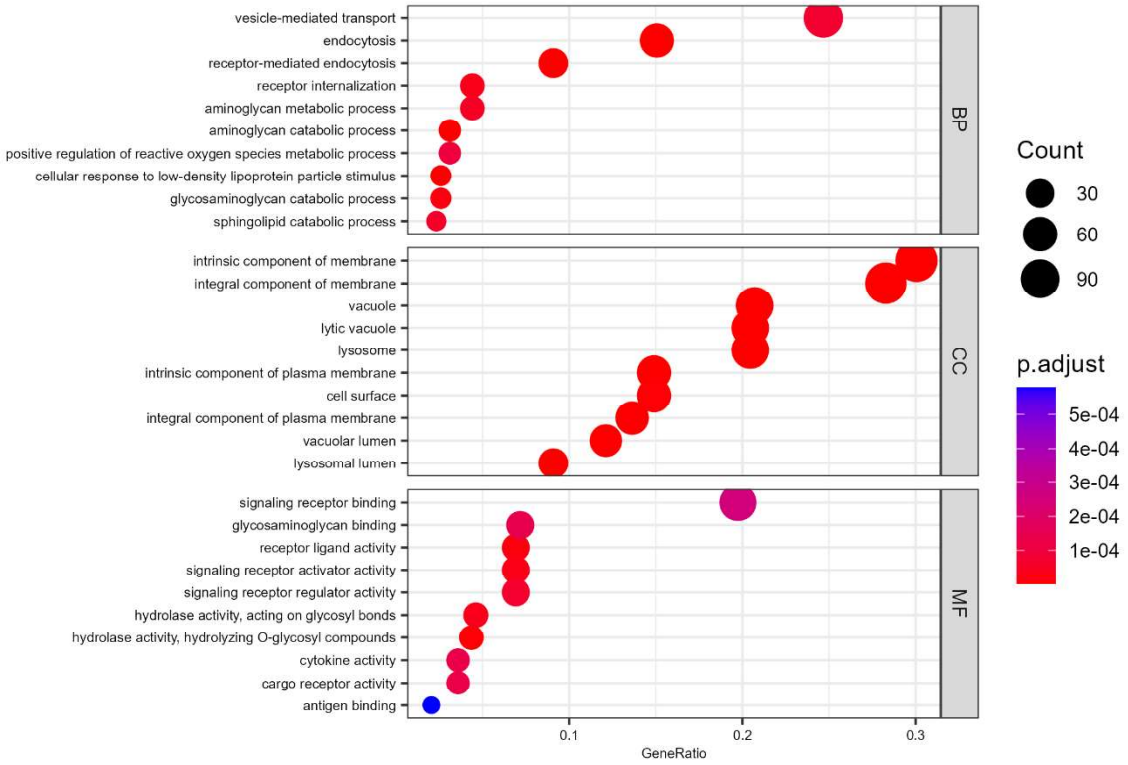

Figure 4.9. Gene ontology analysis of total overrepresented proteins. Biological processes (BP), cellular components (CC), and molecular functions (MF) with associated proteins that were overrepresented in the total data set are identified. GeneRatio: percentage of differentially abundant proteins in each GO term.

An enrichment map network was generated to visualize the fold change of proteins associated with the most significantly overrepresented gene ontology (GO) pathways (Figure 4.10). Several proteins associated with glycosaminoglycan and aminoglycan catabolic processes were downregulated in SHIV EVs compared to the UNINF condition. The pathway with the most differentially abundant proteins was endocytosis. Of the relevant proteins with the most significant negative fold change from UNINF to SHIV, several are associated with positive immune regulation and cell proliferation. The most significantly overexpressed protein in SHIV EVs associated with the endocytosis GO pathway is TIMD4, which was also one of the most significantly overrepresented proteins in the SHIV condition overall (Figure 4.10). Lastly, GSEA using human GO terms was conducted using the entire data set and plotted with the fold change of each pathway comparing the SHIV condition to the UNINF (Figure 4.11). GSEA revealed GO pathways of the entire data set (unbiased to proteins with differential abundance) are primarily downregulated in SHIV EVs compared to UNINF. The most pathways with the most significant negative fold change are largely associated with vesicle, vacuole, and plasma membranes. The only GO pathway with a significant positive fold change in the SHIV condition was negative regulation of epithelial cell proliferation (Figure 4.11).

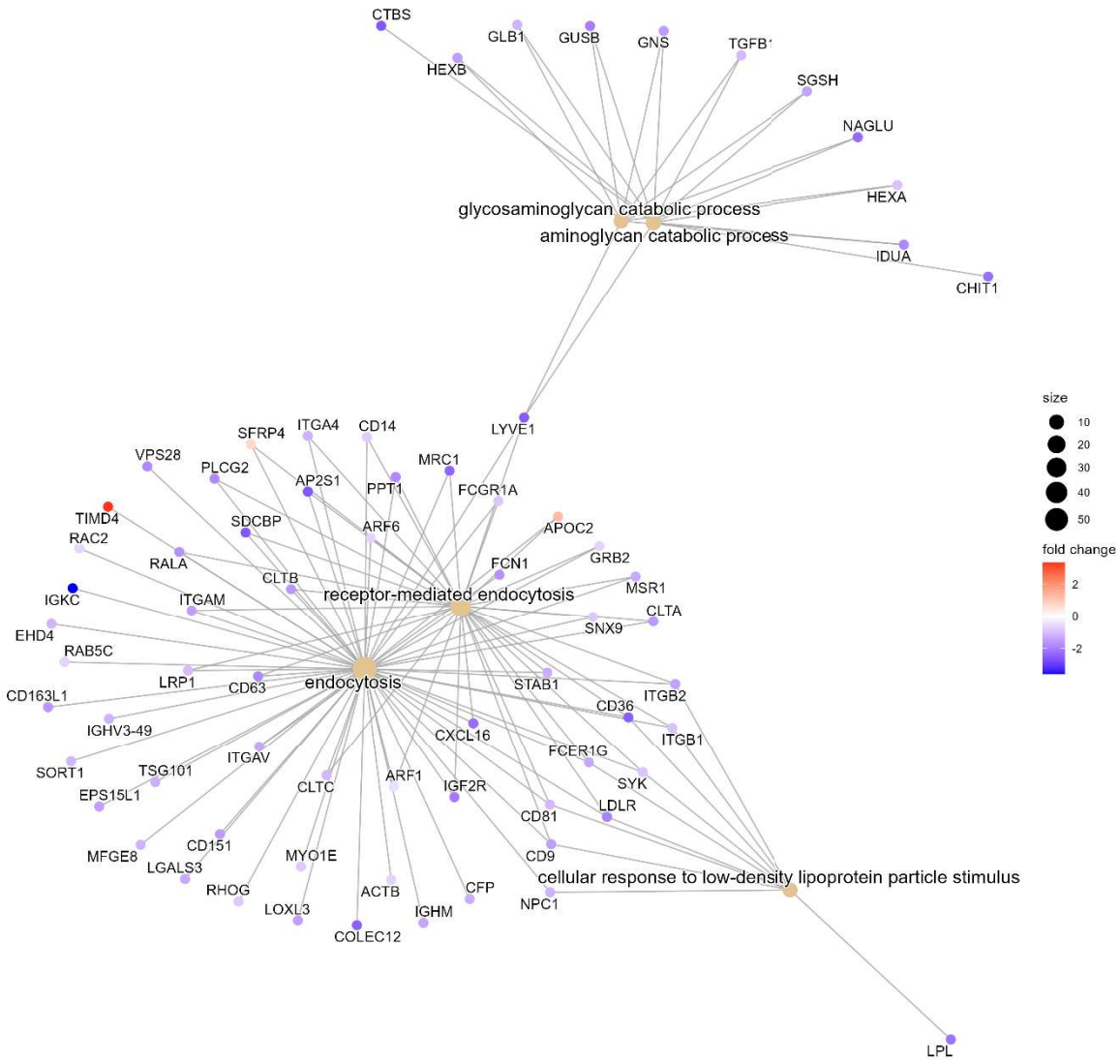

Figure 4.10. Enrichment map network of overrepresented GO pathway proteins. GO pathways with the largest number of associated proteins were plotted in a map network. Fold change of proteins associated with each GO term (SHIV vs. UNINF) are indicated by dot color. Blue: negative fold change, red: positive fold change.

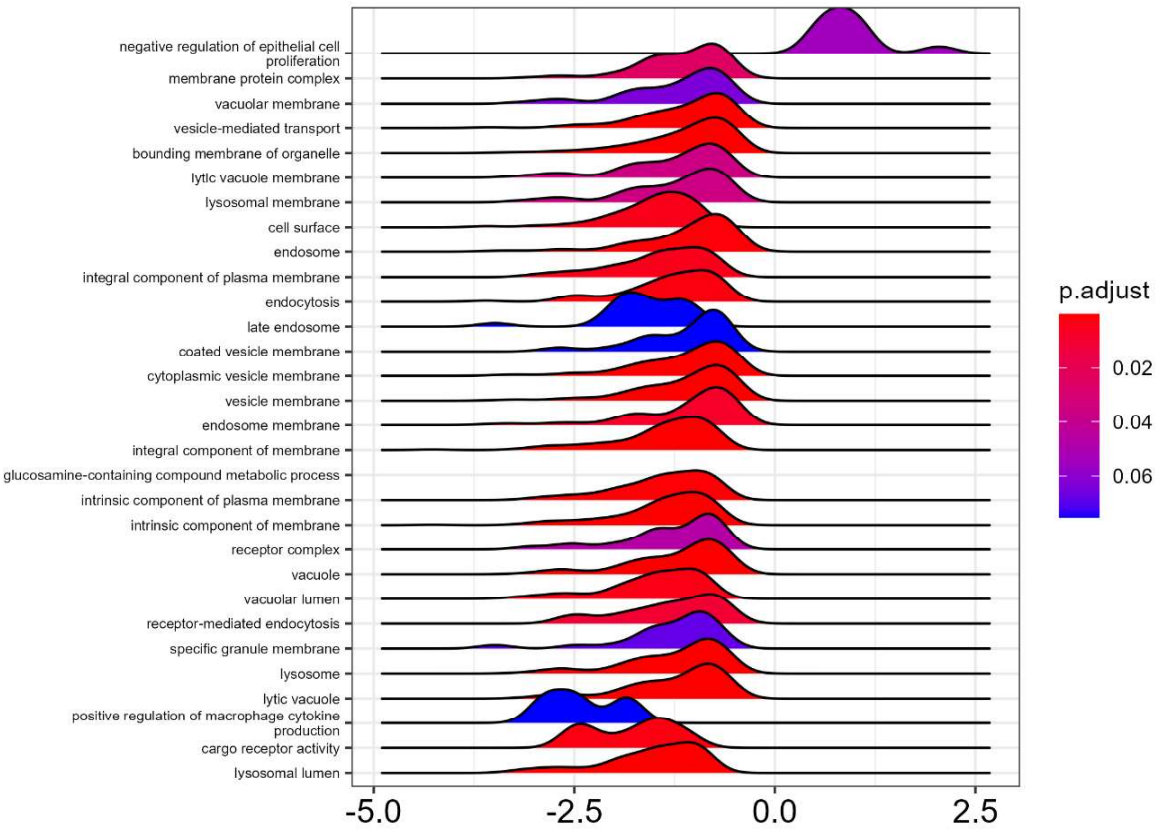

Figure 4.11. Gene set enrichment analysis of GO pathways different between conditions. GSEA was performed using human GO terms on the total protein data set without P value restrictions. Fold change of SHIV vs. UNINF is indicated on the x-axis. Red: P.adjust<0.02, purple: 0.02<P.adjust<0.06, blue: P.adjust>0.06.

Interim Discussion

Our previous findings that myeloid EVs are increased in the plasma of RM during SHIV.D infection and ART suppression necessitated further study. Using an *in vitro* primary RM myeloid cell model, we investigated EV production and protein cargo changes after SHIV.D infection. Paired SHIV.D-/+ replicates from RM donor PBMCs increased the statistical power of analyses. By nanoparticle tracking analysis, we demonstrate that myeloid cells increase EV production after SHIV.D infection. Because SHIV.D forms a

reservoir in myeloid cells in the CNS and is associated with myeloid-mediated neuropathogenesis, we hypothesized that EVs produced by SHIV-infected myeloid cells may carry protein mediators of pathogenesis as cargo.

Bioinformatics analysis of mass spectrometry proteomics data revealed valuable information about the proteomic makeup of MEVs as well as key differences between the proteins found in EVs derived from uninfected and SHIV-infected myeloid cells. First, data filtering and QC/QA demonstrated high-quality protein samples. There were 25 peptides unique to the uninfected cohort and 2 (TIMD4 and HMGN3) both unique and abundant in the SHIV+ cohort. Correlation and principal component analysis revealed appropriate clustering between conditions and samples from the same RM donor. Differential abundance analysis highlighted the top 25 most significantly differentially abundant proteins between the two groups. Of those 25, only 2 were increased in the SHIV+ EVs (HMGN3 and LCN2). Plotting the most significantly differently abundant proteins against the log fold change revealed a more complete picture of proteins that are significantly increased in SHIV+ MEVs. The most differentially abundant proteins in the SHIV condition with the highest fold change are TIMD4, HMGN3, LCN2, NBL1, IGFB1, and IDO1. Nearly all these proteins have demonstrated neuropathogenic effects or roles in HIV pathogenesis.

TIM proteins, including TIMD4, promote HIV entry into the host cell (190,205,206). One study revealed TIMD4+ EVs promote HIV entry into host cells, and blocking with anti-TIMD4 antibodies significantly impeded HIV infection (190). There is no known connection between HMGN3 and HIV or neuropathogenesis, but one report

connected elevated neuronal EV-associated levels of a different high mobility group protein, HMGB1, to neuropsychologically impaired PWH (207). LCN2 is a known mediator of neurotoxicity and neuroinflammation (187,188). A recent report found that LCN2 drives neuronal injury and behavior deficits in a humanized mouse model of HIV (189). Increased levels of plasma IGFBP1 are associated with greater levels of inflammation and more severe disease in PWH (191,192). IDO1 is a known mediator of HIV neuropathogenesis (193,194). IDO1 promotes HIV pathogenicity by inhibiting the differentiation of TH17 cells, and higher levels of plasma IDO1 are associated with larger CNS viral reservoirs (195,208). These significantly overabundant pathologic proteins in SHIV+ MEVs give insight into potential mechanisms of MEV-mediated neuroinflammation and CNS pathology.

Interestingly, one of the proteins that was downregulated in SHIV EVs compared to UNINF EVs was matrix metalloproteinase 7 (MMP7). In general, proteins in the MMP family have been associated with neuronal injury in HIV, but MMP7 specifically is shown to be inversely correlated with viral load (209). The majority of GO pathways identified in both overrepresentation analysis and GSEA that had increased abundance in the uninfected group were associated with vesicle formation, structure, release, and uptake. Further validation of these overrepresented proteins is necessary to substantiate these findings. If validated, this may indicate that EVs produced by SHIV/HIV-infected cells may be formed, released, or execute their functions differently than EVs produced by healthy cells. The only GO pathway associated with overrepresented proteins in the SHIV-infected cohort by GSEA was negative regulation of epithelial cell proliferation. This is a novel

finding that requires validation and further investigation. Other GO pathways overrepresented and more abundant in the uninfected group include proteins associated with glycosaminoglycan binding and catabolic processes. Glycosaminoglycans have been associated with HIV entry into myeloid cells (210). The finding that proteins associated with the breakdown of glycosaminoglycans are increased in uninfected EVs compared to SHIV+ MEVs demonstrates a potential connection between SHIV+ EVs and increased myeloid-SHIV virulence or pathogenesis.

There was an insignificantly greater number of total proteins in the uninfected group compared to the SHIV.D+ group. This is likely due to an increase in cell death or decrease in proliferation over the period of SHIV.D infection in MDM, as the SHIV.D+ wells visually appeared less confluent than the uninfected cell wells. However, this brings about a limitation to this study. First, the low amount of total protein in MEV samples likely excluded proteins from bioinformatics analysis simply due to low abundance. Because of the data filtering parameters, including the condition that each protein in analysis must be detected in 4/6 samples of a particular group, proteins could have been lost to filtering and normalization rules. Additionally, this could have contributed to the observation that the vast majority of differentially abundant proteins were overrepresented in the uninfected EV group. If there are more reads in the uninfected group, it is more likely that peptides would be detected in 4/6 samples. There are also inherent limitations to data imputation, which could influence fold change of proteins between groups. Finally, EV sample contamination with co-precipitated lipoproteins is a common obstacle that is difficult to avoid in EV isolation from cultured cells. Peptides derived from co-precipitated

lipoproteins may account for the prevalence of proteins associated with the cellular response to lipoprotein stimulus GO pathway (177,178).

Overall, these findings demonstrate that EVs produced by SHIV+ myeloid cells are increased in production and carry protein mediators of neuropathogenesis and neuronal injury. These data support the hypothesis that MEVs perpetuate neuropathogenesis during SHIV/HIV infection.

CHAPTER 5

DISCUSSION AND FUTURE DIRECTIONS

Summary and Key Conclusions

The aim of this dissertation is to address the roles of EVs in a novel NHP model of HIV neurological persistence and pathogenesis. We hypothesized that TF *env* SHIV.D forms a brain reservoir and causes persistent neuropathogenesis in rhesus macaques, which is mediated by myeloid-derived extracellular vesicles. Combining historical SHIV.D-infected RM FFPE brain tissue, biofluids from an ongoing cohort of SHIV.D-infected RM, and a primary RM MDM infection model, we determine 1) SHIV.D replicates in the brain, causes neuropathogenesis, and persists on ART in RM, 2) microglia- and neuron-derived EVs are increased in RM blood plasma during viremia and ART suppression, and 3) protein cargo of EVs produced by myeloid cells infected with SHIV.D are significantly changed from those produced by uninfected cells, and contain inflammatory and neuropathogenic proteins. Altogether, these findings contribute to our proposed mechanisms of myeloid EV-mediated SHIV neuropathogenesis (Figure 5.1). Infected myeloid cells, particularly microglia experiencing persistent low levels of viral replication in the brain, produce EVs which carry protein mediators of neuropathogenesis. Through interactions with recipient cells, these EVs increase BBB permeability, decrease epithelial cell proliferation, increase neuronal injury, and increase neuroinflammation.

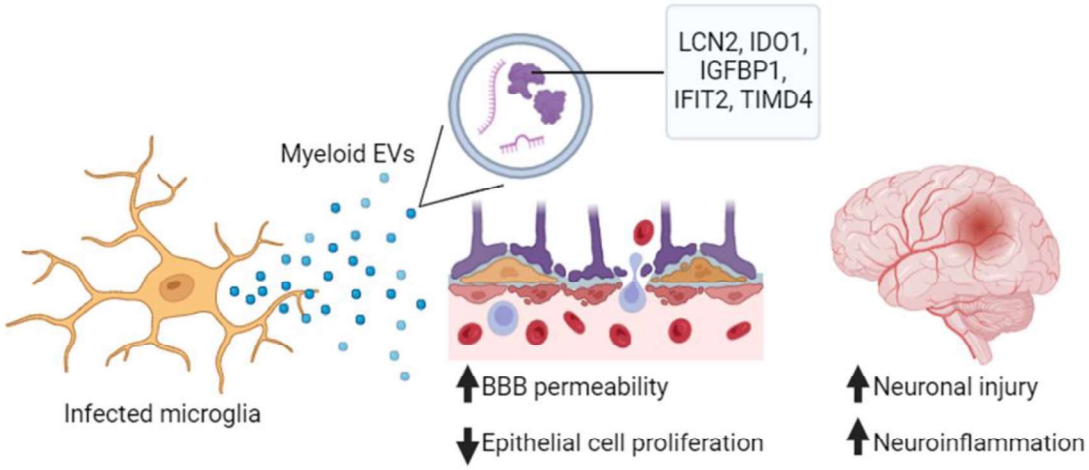

Figure 5.1. Proposed mechanisms of myeloid EV-mediated SHIV neuropathogenesis.

SHIV.D Replicates in the Brain, Causes Neuropathogenesis, and Persists on ART in RM

From a pilot study of RM necropsied while viremic, experiencing ATI, or on suppressive ART, we showed for the first time that SHIV.D replicates inside myeloid cells in the brain, forms a viral reservoir, and causes persistent myeloid-mediated inflammation on ART. These findings were further corroborated by IHC/ISH quantification data from a larger cohort of SHIV.D+ RM that experienced 6 months of continuous ART treatment. After 6 months of suppressive ART, the proviral DNA reservoir in the brain remained, and myeloid-mediated inflammation persisted.

Microglial and Neuronal Brain-Derived EVs are Increased in the Plasma of Viremic and ART-Suppressed RM

Using flow cytometry-based analysis of circulating EVs, we determined the relative amount of relevant cell-derived EV populations in the plasma in a cohort of 10 RM before infection, during SHIV viremia, and during ART-mediated viral suppression. Nanoparticle tracking showed no significant changes in gross plasma EV concentration. However, cell-

specific marker EV flow cytometry revealed that TMEM119+ microglia-derived EVs and CD171+ neuron-derived EVs are significantly increased in the plasma during viremia and ART suppression.

Protein Cargo of EVs Produced by SHIV.D+ Myeloid Cells are Significantly Changed From Those Produced by Uninfected Cells, and Contain Inflammatory and Neuropathogenic Proteins

In an *in vitro* cohort of primary RM monocyte-derived macrophages, we found that myeloid cells significantly increase EV production after SHIV.D infection. Proteomic analysis of MEVs produced by infected and uninfected cells demonstrated that EV protein content is significantly changed with SHIV infection. Notably, EVs produced by SHIV+ myeloid cells carried significantly increased levels of proteins associated with HIV cellular entry, neuroinflammation, pathogenesis, and neuronal injury.

In summary, this dissertation brings together characterization of a novel model of HIV, evidence that SHIV.D causes persistent myeloid-mediated inflammation and viral reservoir formation in the CNS, the discovery that microglial EVs are significantly increased in the plasma during ART suppression, and the recognition of several neuropathogenic proteins upregulated in EVs from SHIV-infected macrophages. Altogether, these findings solidify the belief that EVs are biologically active mediators of neuropathogenesis during SHIV/HIV infection. Our results are consistent with the literature on the roles of EVs during HIV neuropathogenesis, the identification of increased circulating TMEM119+ EVs during SHIV viremia and ART suppression add to the body of research on the behavior and roles of EVs during persistent HIV neuroinflammation. In

addition, the identification of LCN2, TIMD4, and IDO1 advance our understanding of mechanisms of EV-mediated neuropathogenesis. Finally, the identification of novel proteins upregulated in SHIV+ MEVs gives rise to targets for further investigation on new potential drivers of persistent HIV neuropathogenesis.

Unanswered Questions and Future Directions

Our novel findings and the limitations of our studies leave questions to be investigated in future studies of the roles of myeloid EVs in HIV neuropathogenesis. Key questions and proposed future directions follow:

1. Does SHIV.D continue to recapitulate HIV-1 brain reservoir formation, viral kinetics, and neuropathogenesis after years of ART suppression?

   In both the historical brain tissue samples utilized in Chapter 2 and the ongoing SHIV.D RM cohort described in Chapter 3, the longest continuous ART suppression period before necropsy was six months. After six months ART, we see a stable reservoir of proviral DNA in the brain and persistent myeloid-mediated inflammation. Five RM from the ongoing SHIV.D cohort will be maintained on ART for an additional 18 months before necropsy, allowing examination of the SHIV.D reservoir and persistent pathogenesis in the brain after two years of ART suppression. The SHIV.D viral stock used in this challenge also contains a random 10 nucleotide genetic barcode between the *vpx* and *vpr* accessory genes, which is preserved in viral progeny and will be used to track reservoir formation dynamics and viral replication in the brain over time.

2. Are brain-derived EVs overrepresented in the blood during disease due to increased production, increased trafficking out of the CNS, or increased BBB permeability? These explanations are not mutually exclusive, and all may be true. Both previous research (211–213) and our MEV production data described in Chapter 4 conclude that cells do increase EV production in response to infection, stress, or injury. There is also some evidence that circulating CNS-derived EVs may serve as a biomarker for BBB permeability (214). Elucidating the regulatory mechanism that determines how and why cells differentially produce EVs in response to these stimuli is critical to understanding EV-cell signaling and its effects. Further study to determine regulatory mechanisms of EV production and trafficking is necessary.
3. Are TMEM119+ EVs in the plasma elevated in PWH experiencing neurological symptoms?

   Previous research has demonstrated that CD171+ neuron-derived EV production is not different in PWH with and without cognitive impairment (122,172). However, levels of circulating microglia-derived EVs in PWH have not been explored. Our results suggest that abundance of plasma TMEM119+ EVs should be investigated in human samples without HIV and PWH with and without neurological symptoms.
4. How do cell-specific EV populations in the CSF change during SHIV/HIV infection and ART treatment?

   Investigating cell-specific EV populations in the CSF may yield more information on EV production behaviors during SHIV/HIV infection and ART treatment. Some

populations, such as GFAP+ astrocyte-derived EVs, may be identified in relatively greater abundance in the CSF, leading to better flow cytometry compensation and better statistical analysis. However, EV concentration in the CSF is generally low, the amount of CSF in NHP is much less than that of blood plasma, and CSF is substantially more invasive to obtain (215–217). Further studies are necessary to determine specific cell-derived EV production dynamics in the CSF during SHIV/HIV infection and ART suppression.

5. Do antiretroviral drugs alone change the release patterns or cargo of EVs?

   Several antiretroviral drugs are known to have adverse side effects, including neurotoxicity. The current front-line ART drugs, including those used in our studies, have not been found to have any adverse neurocognitive effects (218). We do not anticipate that ART alone would alter the release or cargo of EVs, though further investigation is warranted.

6. Do levels of circulating brain-derived EVs or their specific protein cargo correlate with the amount of persistent myeloid-mediated inflammation or the viral reservoir size in the brains of RM?

   To access specific populations of brain cell-derived EVs in the plasma as potential biomarkers of ongoing neuroinflammation, levels of circulating microglial and neuronal EVs must be tested for correlation with the amount of inflammatory markers in the brain tissue after necropsy. This will be possible after the ongoing SHIV.D RM study is complete, and all 10 RM have been necropsied using

quantitative IHC for markers of myeloid-mediated inflammation. Determining correlation between EV cargo proteins and degree of persistent neuroinflammation is also possible by quantification of specific proteins of interest using enzyme-linked immunosorbent assay or Quanterix Simoa assay compared with IHC results. The same comparisons can be made between circulating brain-derived EV levels of specific cargo of interest and SHIV.D DNAscope, IPDA, or digital droplet PCR to determine if those data correlate with the size of the CNS viral reservoir.

7. What is the biological significance of downregulation and exclusion of several proteins in MEVs following SHIV.D infection?

   Bioinformatics analysis of EV MS proteomics results yielded several proteins that were exclusively found in the uninfected EV cohort, and many more that were significantly downregulated in the SHIV.D+ EV cohort compared to uninfected. An initial database search determined that these exclusive and differentially abundant proteins had a variety of associated pathways. Further experiments are necessary to determine why EVs from SHIV/HIV+ myeloid cells alter their protein cargo after infection.

8. Do EVs produced during SHIV.D infection that contain protein cargo associated with inflammation, pathologic changes, or neuronal injury cause cell damage or disease?

   Due to currently unknown mechanisms of specificity, not all cells internalize or interact with all EVs. Likewise, inflammatory or pathologic EV uptake or interaction may not necessarily cause inflammation or injury in the interacting cell.

Therefore, further investigation is required to determine the pathologic effects of EVs containing potentially harmful differentially abundant proteins on different cell types in the brain, as well as their mechanisms of action.

9. Does myeloid EV cargo change during ART suppression?

   The protein content of myeloid EVs underwent significant change after SHIV.D infection. In addition to secondary validation of proteomics results and a larger study size, EVs produced by ART-treated myeloid cells must be assessed to determine what changes, if any, occur during ART suppression.

This dissertation ties together in vivo and in vitro investigations of EV responses to HIV infection in a novel, clinically relevant SHIV.D/RM model of HIV neurological persistence. We demonstrate evidence that myeloid EVs mediate pathogenesis in a SHIV.D model of HIV. By identification of microglial and neuronal EVs increased in the circulation during SHIV infection and ART suppression combined with the discovery of LCN2, TIMD4, and IDO4 overrepresentation in SHIV+ myeloid EVs, we advance our understanding of the role of myeloid EVs in HIV neuropathogenesis.

BIBLIOGRAPHY

1. Human Immunodeficiency Virus (HIV). Transfus Med Hemotherapy. 2016 May;43(3):203–22.

2. Sharp PM, Hahn BH. The evolution of HIV-1 and the origin of AIDS. Philos Trans R Soc B Biol Sci. 2010 Aug 27;365(1552):2487–94.

3. Williams A, Menon S, Crowe M, Agarwal N, Biccler J, Bbosa N, et al. Geographic and Population Distributions of Human Immunodeficiency Virus (HIV)–1 and HIV-2 Circulating Subtypes: A Systematic Literature Review and Meta-analysis (2010–2021). J Infect Dis. 2023 Dec 1;228(11):1583–91.

4. Sacktor N, Nakasujja N, Skolasky RL, Rezapour M, Robertson K, Musisi S, et al. HIV subtype D is associated with dementia, compared with subtype A, in immunosuppressed individuals at risk of cognitive impairment in Kampala, Uganda. Clin Infect Dis Off Publ Infect Dis Soc Am. 2009 Sep 1;49(5):780–6.

5. Li W, Nath A. Viral Clades: Role In Hiv Neuropathogenesis. In: Grant I, Gendelman HE, Grant I, Everall IP, Fox HS, Gelbard HA, et al., editors. The Neurology of AIDS [Internet]. Oxford University Press; 2011 [cited 2024 Apr 22]. p. 0. Available from: https://doi.org/10.1093/med/9780195399349.003.0061

6. Wang X, Xu H. Residual Proviral Reservoirs: A High Risk for HIV Persistence and Driving Forces for Viral Rebound after Analytical Treatment Interruption. Viruses. 2021 Feb 21;13(2):335.

7. Global health sector strategies on, respectively, HIV, viral hepatitis and sexually transmitted infections for the period 2022-2030 [Internet]. 2022 [cited 2023 Jun 7]. Available from: https://www.who.int/publications-detail-redirect/9789240053779

8. Sacktor N, McDermott MP, Marder K, Schifitto G, Selnes OA, McArthur JC, et al. HIV-associated cognitive impairment before and after the advent of combination therapy. J Neurovirol. 2002 Apr;8(2):136–42.

9. Gannon P, Khan MZ, Kolson DL. Current understanding of HIV-associated neurocognitive disorders pathogenesis. Curr Opin Neurol. 2011 Jun;24(3):275–83.

10. Chan P, Hellmuth J, Spudich S, Valcour V. Cognitive Impairment and Persistent CNS Injury in Treated HIV. Curr HIV/AIDS Rep. 2016 Aug;13(4):209–17.

11. Byrnes SJ, Angelovich TA, Busman-Sahay K, Cochrane CR, Roche M, Estes JD, et al. Non-Human Primate Models of HIV Brain Infection and Cognitive Disorders. Viruses. 2022 Sep;14(9):1997.

12. Hong S, Banks WA. Role of the Immune System in HIV-associated Neuroinflammation and Neurocognitive Implications. Brain Behav Immun. 2015 Mar;0:1–12.

13. Spudich S. HIV and Neurocognitive Dysfunction. Curr HIV/AIDS Rep. 2013 Sep 1;10(3):235–43.

14. Heaton RK, Clifford DB, Franklin DR, Woods SP, Ake C, Vaida F, et al. HIV-associated neurocognitive disorders persist in the era of potent antiretroviral therapy. Neurology. 2010 Dec 7;75(23):2087–96.

15. Heaton RK, Franklin DR, Ellis RJ, McCutchan JA, Letendre SL, LeBlanc S, et al. HIV-associated neurocognitive disorders before and during the era of combination antiretroviral therapy: differences in rates, nature, and predictors. J Neurovirol. 2011 Feb 1;17(1):3–16.

16. Gott C, Gates T, Dermody N, Brew BJ, Cysique LA. Cognitive change trajectories in virally suppressed HIV-infected individuals indicate high prevalence of disease activity. PLOS ONE. 2017 Mar 6;12(3):e0171887.

17. Simioni S, Cavassini M, Annoni JM, Rimbault Abraham A, Bourquin I, Schiffer V, et al. Cognitive dysfunction in HIV patients despite long-standing suppression of viremia. AIDS. 2010 Jun 1;24(9):1243.

18. McIntosh RC, Clark US, Cherner M, Cysique LA, Heaton RK, Levin J, et al. The Evolution of Assessing Central Nervous System Complications in Human Immunodeficiency Virus: Where Do We Go From Here? J Infect Dis. 2023 Mar 17;227(Suppl 1):S30–7.

19. Joseph SB, Gianella S, Burdo TH, Cinque P, Gisslen M, Letendre S, et al. Biotypes of Central Nervous System Complications in People With Human Immunodeficiency Virus: Virology, Immunology, and Neuropathology. J Infect Dis. 2023 Mar 17;227(Suppl 1):S3–15.

20. Johnson TP, Nath A. Biotypes of HIV-associated neurocognitive disorders based on viral and immune pathogenesis. Curr Opin Infect Dis. 2022 Jun 1;35(3):223–30.

21. Lu HJ, Fu YY, Wei QQ, Zhang ZJ. Neuroinflammation in HIV-Related Neuropathic Pain. Front Pharmacol. 2021 Apr 20;12:653852.

22. Vivithanaporn P, Heo G, Gamble J, Krentz HB, Hoke A, Gill MJ, et al. Neurologic disease burden in treated HIV/AIDS predicts survival. Neurology. 2010 Sep 28;75(13):1150–8.

23. Burdo TH, Lackner A, Williams KC. Monocyte/macrophages and their role in HIV neuropathogenesis. Immunol Rev. 2013 Jul;254(1):102–13.

24. Veenstra M, León-Rivera R, Li M, Gama L, Clements JE, Berman JW. Mechanisms of CNS Viral Seeding by HIV+ CD14+ CD16+ Monocytes: Establishment and Reseeding of Viral Reservoirs Contributing to HIV-Associated Neurocognitive Disorders. mBio. 2017 Oct 24;8(5):e01280-17.

25. Schnell G, Spudich S, Harrington P, Price RW, Swanstrom R. Compartmentalized human immunodeficiency virus type 1 originates from long-lived cells in some subjects with HIV-1-associated dementia. PLoS Pathog. 2009 Apr;5(4):e1000395.

26. Bednar MM, Sturdevant CB, Tompkins LA, Arrildt KT, Dukhovlinova E, Kincer LP, et al. Compartmentalization, Viral Evolution, and Viral Latency of HIV in the CNS. Curr HIV/AIDS Rep. 2015 Jun;12(2):262–71.

27. Wallet C, De Rovere M, Van Assche J, Daouad F, De Wit S, Gautier V, et al. Microglial Cells: The Main HIV-1 Reservoir in the Brain. Front Cell Infect Microbiol [Internet]. 2019 [cited 2023 Jun 7];9. Available from: https://www.frontiersin.org/articles/10.3389/fcimb.2019.00362

28. Ko A, Kang G, Hattler JB, Galadima HI, Zhang J, Li Q, et al. Macrophages but not Astrocytes Harbor HIV DNA in the Brains of HIV-1-Infected Aviremic Individuals on Suppressive Antiretroviral Therapy. J Neuroimmune Pharmacol Off J Soc NeuroImmune Pharmacol. 2019 Mar;14(1):110–9.

29. Bai R, Song C, Lv S, Chang L, Hua W, Weng W, et al. Role of microglia in HIV-1 infection. AIDS Res Ther. 2023 Mar 16;20(1):16.

30. Gisslen M, Keating SM, Spudich S, Arechiga V, Stephenson S, Zetterberg H, et al. Compartmentalization of cerebrospinal fluid inflammation across the spectrum of untreated HIV-1 infection, central nervous system injury and viral suppression. PloS One. 2021;16(5):e0250987.

31. Navia BA, Cho ES, Petito CK, Price RW. The AIDS dementia complex: II. Neuropathology. Ann Neurol. 1986 Jun;19(6):525–35.

32. Post MJD, Thurnher MM, Clifford DB, Nath A, Gonzalez RG, Gupta RK, et al. CNS-immune reconstitution inflammatory syndrome in the setting of HIV infection, part 1: overview and discussion of progressive multifocal leukoencephalopathy-immune reconstitution inflammatory syndrome and cryptococcal-immune reconstitution inflammatory syndrome. AJNR Am J Neuroradiol. 2013 Jul;34(7):1297–307.

33. Chang CC, Sheikh V, Sereti I, French MA. Immune Reconstitution Disorders in Patients With HIV Infection: From Pathogenesis to Prevention and Treatment. Curr HIV/AIDS Rep. 2014 Sep 1;11(3):223–32.

34. Miller RF, Isaacson PG, Hall-Craggs M, Lucas S, Gray F, Scaravilli F, et al. Cerebral CD8+ lymphocytosis in HIV-1 infected patients with immune restoration induced by HAART. Acta Neuropathol (Berl). 2004 Jul;108(1):17–23.

35. Luciw PA, Shaw KE, Unger RE, Planelles V, Stout MW, Lackner JE, et al. Genetic and biological comparisons of pathogenic and nonpathogenic molecular clones of simian immunodeficiency virus (SIVmac). AIDS Res Hum Retroviruses. 1992 Mar;8(3):395–402.

36. Worobey M, Telfer P, Souquière S, Hunter M, Coleman CA, Metzger MJ, et al. Island biogeography reveals the deep history of SIV. Science. 2010 Sep 17;329(5998):1487.

37. Pollom E, Dang KK, Potter EL, Gorelick RJ, Burch CL, Weeks KM, et al. Comparison of SIV and HIV-1 Genomic RNA Structures Reveals Impact of Sequence Evolution on Conserved and Non-Conserved Structural Motifs. PLoS Pathog. 2013 Apr 4;9(4):e1003294.

38. Kestler HW, Li Y, Naidu YM, Butler CV, Ochs MF, Jaenel G, et al. Comparison of simian immunodeficiency virus isolates. Nature. 1988 Feb 18;331(6157):619–22.

39. Levy JA. The value of primate models for studying human immunodeficiency virus pathogenesis. J Med Primatol. 1996;25(3):163–74.

40. McCarthy KR, Johnson WE, Kirmaier A. Phylogeny and History of the Lost SIV from Crab-Eating Macaques: SIVmfa. PLOS ONE. 2016 Jul 14;11(7):e0159281.

41. Daniel MD, Letvin NL, King NW, Kannagi M, Sehgal PK, Hunt RD, et al. Isolation of T-cell tropic HTLV-III-like retrovirus from macaques. Science. 1985 Jun 7;228(4704):1201–4.

42. Pauza CD, Emau P, Salvato MS, Trivedi P, MacKenzie D, Malkovsky M, et al. Pathogenesis of SIVmac251 after atraumatic inoculation of the rectal mucosa in rhesus monkeys. J Med Primatol. 1993;22(2–3):154–61.

43. Batten CJ, De Rose R, Wilson KM, Agy MB, Chea S, Stratov I, et al. Comparative evaluation of simian, simian-human, and human immunodeficiency virus infections in the pigtail macaque (Macaca nemestrina) model. AIDS Res Hum Retroviruses. 2006 Jun;22(6):580–8.

44. Mannioui A, Bourry O, Sellier P, Delache B, Brochard P, Andrieu T, et al. Dynamics of viral replication in blood and lymphoid tissues during SIVmac251 infection of macaques. Retrovirology. 2009 Nov 23;6:106.

45. Okamura T, Tsujimura Y, Soma S, Takahashi I, Matsuo K, Yasutomi Y. Simian immunodeficiency virus SIVmac239 infection and simian human immunodeficiency virus SHIV89.6P infection result in progression to AIDS in cynomolgus macaques of Asian origin. J Gen Virol. 2016;97(12):3413–26.

46. Obregon-Perko V, Bricker K, Chahroudi A. The Brain Retains: Nonhuman Primate Models for Pediatric HIV-1 in the CNS. Curr HIV/AIDS Rep. 2020 Aug;17(4):343–53.

47. Van Zandt AR, MacLean AG. Advances in HIV therapeutics and cure strategies: findings obtained through non-human primate studies. J Neurovirol. 2023 Aug 1;29(4):389–99.

48. Van Rompay KKA. The use of nonhuman primate models of HIV infection for the evaluation of antiviral strategies. AIDS Res Hum Retroviruses. 2012 Jan;28(1):16–35.

49. Veazey RS, Lackner AA. Nonhuman Primate Models and Understanding the Pathogenesis of HIV Infection and AIDS. ILAR J. 2017 Dec 1;58(2):160–71.

50. Del Prete GQ, Lifson JD. Considerations in the development of nonhuman primate models of combination antiretroviral therapy for studies of AIDS virus suppression, residual virus, and curative strategies. Curr Opin HIV AIDS. 2013 Jul;8(4):262.

51. Gelé T, Gouget H, Dereuddre-Bosquet N, Furlan V, Le Grand R, Lambotte O, et al. Pharmacological Validation of Long-Term Treatment with Antiretroviral Drugs in a Model of SIV-Infected Non-Human Primates. Pharmaceutics. 2022 Oct 25;14(11):2282.

52. Del Prete GQ, Smedley J, Macallister R, Jones GS, Li B, Hattersley J, et al. Short Communication: Comparative Evaluation of Coformulated Injectable Combination Antiretroviral Therapy Regimens in Simian Immunodeficiency Virus-Infected Rhesus Macaques. AIDS Res Hum Retroviruses. 2016 Feb;32(2):163–8.

53. What to Start: Initial Combination Antiretroviral Regimens | NIH [Internet]. 2022 [cited 2024 Apr 30]. Available from: https://clinicalinfo.hiv.gov/en/guidelines/hiv-clinical-guidelines-adult-and-adolescent-arv/what-start-initial-combination

54. Marcon L, Choe H, Martin KA, Farzan M, Ponath PD, Wu L, et al. Utilization of C-C chemokine receptor 5 by the envelope glycoproteins of a pathogenic simian immunodeficiency virus, SIVmac239. J Virol. 1997 Mar;71(3):2522–7.

55. Chen Z, Zhou P, Ho DD, Landau NR, Marx PA. Genetically divergent strains of simian immunodeficiency virus use CCR5 as a coreceptor for entry. J Virol. 1997 Apr;71(4):2705–14.

56. Marx PA, Chen Z. The function of simian chemokine receptors in the replication of SIV. Semin Immunol. 1998 Jun;10(3):215–23.

57. Banapour B, Marthas ML, Munn RJ, Luciw PA. In vitro macrophage tropism of pathogenic and nonpathogenic molecular clones of simian immunodeficiency virus (SIVmac). Virology. 1991 Jul;183(1):12–9.

58. Stephens EB, Liu ZQ, Zhu GW, Adany I, Joag SV, Foresman L, et al. Lymphocyte-tropic simian immunodeficiency virus causes persistent infection in the brains of rhesus monkeys. Virology. 1995 Nov 10;213(2):600–14.

59. Miller CJ, Marthas M, Greenier J, Lu D, Dailey PJ, Lu Y. In vivo replication capacity rather than in vitro macrophage tropism predicts efficiency of vaginal transmission of simian immunodeficiency virus or simian/human immunodeficiency virus in rhesus macaques. J Virol. 1998 Apr;72(4):3248–58.

60. Moeser M, Nielsen JR, Joseph SB. Macrophage Tropism in Pathogenic HIV-1 and SIV Infections. Viruses. 2020 Sep 25;12(10):1077.

61. Chakrabarti L, Hurtrel M, Maire MA, Vazeux R, Dormont D, Montagnier L, et al. Early viral replication in the brain of SIV-infected rhesus monkeys. Am J Pathol. 1991 Dec;139(6):1273–80.

62. Abreu CM, Veenhuis RT, Avalos CR, Graham S, Parrilla DR, Ferreira EA, et al. Myeloid and CD4 T Cells Comprise the Latent Reservoir in Antiretroviral Therapy-Suppressed SIVmac251-Infected Macaques. mBio. 2019 Aug 20;10(4):e01659-19.

63. Perez S, Johnson AM, Xiang S hua, Li J, Foley BT, Doyle-Meyers L, et al. Persistence of SIV in the brain of SIV-infected Chinese rhesus macaques with or without antiretroviral therapy. J Neurovirol. 2018 Feb;24(1):62–74.

64. Warfield R, Robinson JA, Podgorski RM, Miller AD, Burdo TH. Neuroinflammation in the Dorsal Root Ganglia and Dorsal Horn Contributes to Persistence of Nociceptor Sensitization in SIV-Infected Antiretroviral Therapy-Treated Macaques. Am J Pathol. 2023 Dec 1;193(12):2017–30.

65. Burdo TH, Orzechowski K, Knight HL, Miller AD, Williams K. Dorsal root ganglia damage in SIV-infected rhesus macaques: an animal model of HIV-induced sensory neuropathy. Am J Pathol. 2012 Apr;180(4):1362–9.

66. Anderson MG, Hauer D, Sharma DP, Joag SV, Narayan O, Zink MC, et al. Analysis of envelope changes acquired by SIVmac239 during neuroadaption in rhesus macaques. Virology. 1993 Aug;195(2):616–26.

67. Berman NE, Sheffield LG, Purcell J, Joag SV, Narayan O, Cheney P. Gradient of microglial activation in the brain of SIV infected macaques. J Neuro-AIDS. 1998;2(1):43–54.

68. Berman NE, Raymond LA, Warren KA, Raghavan R, Joag SV, Narayan O, et al. Fractionator analysis shows loss of neurons in the lateral geniculate nucleus of macaques infected with neurovirulent simian immunodeficiency virus. Neuropathol Appl Neurobiol. 1998 Feb;24(1):44–52.

69. Zink MC, Suryanarayana K, Mankowski JL, Shen A, Piatak M, Spelman JP, et al. High Viral Load in the Cerebrospinal Fluid and Brain Correlates with Severity of Simian Immunodeficiency Virus Encephalitis. J Virol. 1999 Dec;73(12):10480–8.

70. Mangus LM, Beck SE, Queen SE, Brill SA, Shirk EN, Metcalf Pate KA, et al. Lymphocyte-Dominant Encephalitis and Meningitis in Simian Immunodeficiency Virus–Infected Macaques Receiving Antiretroviral Therapy. Am J Pathol. 2018 Jan;188(1):125–34.

71. Zink MC, Brice AK, Kelly KM, Queen SE, Gama L, Li M, et al. SIV-infected macaques treated with highly active antiretroviral therapy (HAART) have reduced CNS virus replication and inflammation but persistence of viral DNA. J Infect Dis. 2010 Jul 1;202(1):161–70.

72. Dorsey JL, Mangus LM, Hauer P, Ebenezer GJ, Queen SE, Laast VA, et al. Persistent Peripheral Nervous System Damage in Simian Immunodeficiency Virus-Infected Macaques Receiving Antiretroviral Therapy. J Neuropathol Exp Neurol. 2015 Nov;74(11):1053–60.

73. Matsuda K, Riddick NE, Lee CA, Puryear SB, Wu F, Lafont BAP, et al. A SIV molecular clone that targets the CNS and induces neuroAIDS in rhesus macaques. PLOS Pathog. 2017 Aug 7;13(8):e1006538.

74. Lee CA, Beasley E, Sundar K, Smelkinson M, Vinton C, Deleage C, et al. Simian Immunodeficiency Virus-Infected Memory CD4+ T Cells Infiltrate to the Site of Infected Macrophages in the Neuroparenchyma of a Chronic Macaque Model of Neurological Complications of AIDS. mBio. 2020 Apr 21;11(2):e00602-20.

75. Raghavan R, Stephens EB, Joag SV, Adany I, Pinson DM, Li Z, et al. Neuropathogenesis of chimeric simian/human immunodeficiency virus infection in pig-tailed and rhesus macaques. Brain Pathol Zurich Switz. 1997 Jul;7(3):851–61.

76. Liu ZQ, Muhkerjee S, Sahni M, McCormick-Davis C, Leung K, Li Z, et al. Derivation and biological characterization of a molecular clone of SHIV(KU-2) that causes AIDS, neurological disease, and renal disease in rhesus macaques. Virology. 1999 Aug 1;260(2):295–307.

77. Xiao Q, Li J, Yu Q, Bao R, Liu J, Liu H, et al. Distinct Compartmentalization in the CNS of SHIVKU-1-Infected Chinese Rhesus Macaque Is Associated With Severe Neuropathology. JAIDS J Acquir Immune Defic Syndr. 2015 Dec 15;70(5):e168.

78. Song RJ, Chenine AL, Rasmussen RA, Ruprecht CR, Mirshahidi S, Grisson RD, et al. Molecularly Cloned SHIV-1157ipd3N4: a Highly Replication- Competent, Mucosally Transmissible R5 Simian-Human Immunodeficiency Virus Encoding HIV Clade C env. J Virol. 2006 Sep;80(17):8729–38.

79. Hsu DC, Sunyakumthorn P, Wegner M, Schuetz A, Silsorn D, Estes JD, et al. Central Nervous System Inflammation and Infection during Early, Nonaccelerated Simian-Human Immunodeficiency Virus Infection in Rhesus Macaques. J Virol. 2018 Jun 1;92(11):e00222-18.

80. Harbison C, Zhuang K, Gettie A, Blanchard J, Knight H, Didier P, et al. Giant cell encephalitis and microglial infection with mucosally transmitted simian-human immunodeficiency virus SHIVSF162P3N in rhesus macaques. J Neurovirol. 2014 Feb;20(1):62–72.

81. Li H, Wang S, Kong R, Ding W, Lee FH, Parker Z, et al. Envelope residue 375 substitutions in simian-human immunodeficiency viruses enhance CD4 binding and replication in rhesus macaques. Proc Natl Acad Sci U S A. 2016 Jun 14;113(24):E3413-3422.

82. Hawes CE, Elizaldi SR, Beckman D, Diniz GB, Shaan Lakshmanappa Y, Ott S, et al. Neuroinflammatory transcriptional programs induced in rhesus pre-frontal cortex white matter during acute SHIV infection. J Neuroinflammation. 2022 Oct 6;19:250.

83. Li J, Lord CI, Haseltine W, Letvin NL, Sodroski J. Infection of cynomolgus monkeys with a chimeric HIV-1/SIVmac virus that expresses the HIV-1 envelope glycoproteins. J Acquir Immune Defic Syndr. 1992;5(7):639–46.

84. Bauer AM, Bar KJ. Advances in simian--human immunodeficiency viruses for nonhuman primate studies of HIV prevention and cure. Curr Opin HIV AIDS. 2020 Sep;15(5):275.

85. Joag SV, Li Z, Foresman L, Pinson DM, Raghavan R, Zhuge W, et al. Characterization of the pathogenic KU-SHIV model of acquired immunodeficiency syndrome in macaques. AIDS Res Hum Retroviruses. 1997 May 20;13(8):635–45.

86. Buch SJ, Villinger F, Pinson D, Hou Y, Adany I, Li Z, et al. Innate differences between simian-human immunodeficiency virus (SHIV)(KU-2)-infected rhesus and pig-tailed macaques in development of neurological disease. Virology. 2002 Mar 30;295(1):54–62.

87. Buch S, Pinson D, Hou Y, Adany I, Li Z, Mukherjee S, et al. Neuropathogenesis of chimeric simian human immunodeficiency virus infection in rhesus macaques. J Med Primatol. 2000 Aug;29(3–4):96–106.

88. Bar KJ, Coronado E, Hensley-McBain T, O'Connor MA, Osborn JM, Miller C, et al. Simian-Human Immunodeficiency Virus SHIV.CH505 Infection of Rhesus Macaques Results in Persistent Viral Replication and Induces Intestinal Immunopathology. J Virol. 2019 Sep 15;93(18):e00372-19.

89. Bauer AM, Ziani W, Lindemuth E, Kuri-Cervantes L, Li H, Lee FH, et al. Novel Transmitted/Founder Simian-Human Immunodeficiency Viruses for Human Immunodeficiency Virus Latency and Cure Research. J Virol. 2020 Mar 31;94(8):e01659-19.

90. Li H, Wang S, Lee FH, Roark RS, Murphy AI, Smith J, et al. New SHIVs and Improved Design Strategy for Modeling HIV-1 Transmission, Immunopathogenesis, Prevention and Cure. J Virol. 2021 May 10;95(11):e00071-21, JVI.00071-21.

91. Bauer A, Lindemuth E, Marino FE, Krause R, Joy J, Docken SS, et al. Adaptation of a transmitted/founder simian-human immunodeficiency virus for enhanced replication in rhesus macaques. PLOS Pathog. 2023 Jul 3;19(7):e1011059.

92. Podgorski RM, Robinson JA, Smith MD, Mallick S, Zhao H, Veazey RS, et al. Transmitted/founder SHIV.D replicates in the brain, causes neuropathogenesis, and persists on combination antiretroviral therapy in rhesus macaques. Retrovirology. 2023 Aug 10;20(1):13.

93. Baalwa J, Wang S, Parrish NF, Decker JM, Keele BF, Learn GH, et al. Molecular identification, cloning and characterization of transmitted/founder HIV-1 subtype A, D and A/D infectious molecular clones. Virology. 2013 Feb 5;436(1):33–48.

94. Tyor W, Fritz-French C, Nath A. Effect of HIV clade differences on the onset and severity of HIV-associated neurocognitive disorders. J Neurovirol. 2013 Dec;19(6):515–22.

95. Joseph SB, Swanstrom R, Kashuba ADM, Cohen MS. Bottlenecks in HIV-1 transmission: insights from the study of founder viruses. Nat Rev Microbiol. 2015 Jul;13(7):414–25.

96. van Niel G, D'Angelo G, Raposo G. Shedding light on the cell biology of extracellular vesicles. Nat Rev Mol Cell Biol. 2018 Apr;19(4):213–28.

97. Denzer K, Kleijmeer MJ, Heijnen HFG, Stoorvogel W, Geuze HJ. Exosome: from internal vesicle of the multivesicular body to intercellular signaling device. J Cell Sci. 2000 Oct 1;113(19):3365–74.

98. Abels ER, Breakefield XO. Introduction to Extracellular Vesicles: Biogenesis, RNA Cargo Selection, Content, Release, and Uptake. Cell Mol Neurobiol. 2016 Apr;36(3):301–12.

99. Akers JC, Gonda D, Kim R, Carter BS, Chen CC. Biogenesis of extracellular vesicles (EV): exosomes, microvesicles, retrovirus-like vesicles, and apoptotic bodies. J Neurooncol. 2013 May;113(1):1–11.

100. Andreu Z, Yáñez-Mó M. Tetraspanins in Extracellular Vesicle Formation and Function. Front Immunol [Internet]. 2014 Sep 16 [cited 2024 May 2];5. Available from: https://www.frontiersin.org/journals/immunology/articles/10.3389/fimmu.2014.00442/full

101. Zou X, Lei Q, Luo X, Yin J, chen S, Hao C, et al. Advances in biological functions and applications of apoptotic vesicles. Cell Commun Signal. 2023 Sep 25;21(1):260.

102. Russell AE, Sneider A, Witwer KW, Bergese P, Bhattacharyya SN, Cocks A, et al. Biological membranes in EV biogenesis, stability, uptake, and cargo transfer: an ISEV position paper arising from the ISEV membranes and EVs workshop. J Extracell Vesicles. 2019 Nov 8;8(1):1684862.

103. Jankovičová J, Sečová P, Michalková K, Antalíková J. Tetraspanins, More than Markers of Extracellular Vesicles in Reproduction. Int J Mol Sci. 2020 Oct 14;21(20):7568.

104. Raposo G, Stoorvogel W. Extracellular vesicles: Exosomes, microvesicles, and friends. J Cell Biol. 2013 Feb 18;200(4):373–83.

105. Doyle LM, Wang MZ. Overview of Extracellular Vesicles, Their Origin, Composition, Purpose, and Methods for Exosome Isolation and Analysis. Cells. 2019 Jul 15;8(7):727.

106. Brodeur A, Migneault F, Lanoie M, Beillevaire D, Turgeon J, Karakeussian-Rimbaud A, et al. Apoptotic exosome-like vesicles transfer specific and functional mRNAs to endothelial cells by phosphatidylserine-dependent macropinocytosis. Cell Death Dis. 2023 Jul 20;14(7):1–15.

107. Liu W, Bai X, Zhang A, Huang J, Xu S, Zhang J. Role of Exosomes in Central Nervous System Diseases. Front Mol Neurosci [Internet]. 2019 Oct 4 [cited 2024 May 2];12. Available from: https://www.frontiersin.org/articles/10.3389/fnmol.2019.00240

108. Shetty AK, Upadhya R. Extracellular Vesicles in Health and Disease. Aging Dis. 2021 Sep 1;12(6):1358–62.

109. Mathieu M, Martin-Jaular L, Lavieu G, Théry C. Specificities of secretion and uptake of exosomes and other extracellular vesicles for cell-to-cell communication. Nat Cell Biol. 2019 Jan;21(1):9–17.

110. Mulcahy LA, Pink RC, Carter DRF. Routes and mechanisms of extracellular vesicle uptake. J Extracell Vesicles. 2014 Aug 4;3:10.3402/jev.v3.24641.

111. Joshi BS, de Beer MA, Giepmans BNG, Zuhorn IS. Endocytosis of Extracellular Vesicles and Release of Their Cargo from Endosomes. ACS Nano. 2020 Apr 28;14(4):4444–55.

112. Bonsergent E, Grisard E, Buchrieser J, Schwartz O, Théry C, Lavieu G. Quantitative characterization of extracellular vesicle uptake and content delivery within mammalian cells. Nat Commun. 2021 Mar 25;12(1):1864.

113. Linxweiler J, Kolbinger A, Himbert D, Zeuschner P, Saar M, Stöckle M, et al. Organ-Specific Uptake of Extracellular Vesicles Secreted by Urological Cancer Cells. Cancers. 2021 Sep 30;13(19):4937.

114. Chivet M, Javalet C, Laulagnier K, Blot B, Hemming FJ, Sadoul R. Exosomes secreted by cortical neurons upon glutamatergic synapse activation specifically interact with neurons. J Extracell Vesicles. 2014;3:24722.

115. Fevrier B, Vilette D, Archer F, Loew D, Faigle W, Vidal M, et al. Cells release prions in association with exosomes. Proc Natl Acad Sci U S A. 2004 Jun 29;101(26):9683–8.

116. Vella LJ, Sharples RA, Lawson VA, Masters CL, Cappai R, Hill AF. Packaging of prions into exosomes is associated with a novel pathway of PrP processing. J Pathol. 2007 Apr;211(5):582–90.

117. Rajendran L, Honsho M, Zahn TR, Keller P, Geiger KD, Verkade P, et al. Alzheimer's disease β-amyloid peptides are released in association with exosomes. Proc Natl Acad Sci U S A. 2006 Jul 25;103(30):11172–7.

118. Saman S, Kim W, Raya M, Visnick Y, Miro S, Saman S, et al. Exosome-associated tau is secreted in tauopathy models and is selectively phosphorylated in cerebrospinal fluid in early Alzheimer disease. J Biol Chem. 2012 Feb 3;287(6):3842–9.

119. Jiang L, Dong H, Cao H, Ji X, Luan S, Liu J. Exosomes in Pathogenesis, Diagnosis, and Treatment of Alzheimer's Disease. Med Sci Monit Int Med J Exp Clin Res. 2019 May 6;25:3329–35.

120. Pérez M, Avila J, Hernández F. Propagation of Tau via Extracellular Vesicles. Front Neurosci. 2019 Jul 2;13:698.

121. Badhwar A, Haqqani AS. Biomarker potential of brain-secreted extracellular vesicles in blood in Alzheimer's disease. Alzheimers Dement Diagn Assess Dis Monit. 2020 Mar 5;12(1):e12001.

122. Pulliam L, Sun B, Mustapic M, Chawla S, Kapogiannis D. Plasma neuronal exosomes serve as biomarkers of cognitive impairment in HIV infection and Alzheimer's Disease. J Neurovirol. 2019 Oct;25(5):702–9.

123. Winston CN, Romero HK, Ellisman M, Nauss S, Julovich DA, Conger T, et al. Assessing Neuronal and Astrocyte Derived Exosomes From Individuals With Mild Traumatic Brain Injury for Markers of Neurodegeneration and Cytotoxic Activity. Front Neurosci [Internet]. 2019 [cited 2024 Jan 12];13. Available from: https://www.frontiersin.org/articles/10.3389/fnins.2019.01005

124. Xia X, Wang Y, Zheng JC. Extracellular vesicles, from the pathogenesis to the therapy of neurodegenerative diseases. Transl Neurodegener. 2022 Dec 12;11:53.

125. Hill AF. Extracellular Vesicles and Neurodegenerative Diseases. J Neurosci. 2019 Nov 20;39(47):9269–73.

126. Crenshaw BJ, Gu L, Sims B, Matthews QL. Exosome Biogenesis and Biological Function in Response to Viral Infections. Open Virol J. 2018 Sep 28;12:134–48.

127. Saad MH, Badierah R, Redwan EM, El-Fakharany EM. A Comprehensive Insight into the Role of Exosomes in Viral Infection: Dual Faces Bearing Different Functions. Pharmaceutics. 2021 Sep;13(9):1405.

128. Hurley JH, Cada AK. Inside Job: How the ESCRTs release HIV-1 from infected cells. Biochem Soc Trans. 2018 Oct 19;46(5):1029–36.

129. Usami Y, Popov S, Popova E, Inoue M, Weissenhorn W, G Göttlinger H. The ESCRT pathway and HIV-1 budding. Biochem Soc Trans. 2009 Feb;37(Pt 1):181–4.

130. Sami Saribas A, Cicalese S, Ahooyi TM, Khalili K, Amini S, Sariyer IK. HIV-1 Nef is released in extracellular vesicles derived from astrocytes: evidence for Nef-mediated neurotoxicity. Cell Death Dis. 2017 Jan;8(1):e2542.

131. Kadiu I, Narayanasamy P, Dash PK, Zhang W, Gendelman HE. Biochemical and Biologic Characterization of Exosomes and Microvesicles as Facilitators of HIV-1 Infection in Macrophages. J Immunol. 2012 Jul 15;189(2):744–54.

132. Chen J, Li C, Li R, Chen H, Chen D, Li W. Exosomes in HIV infection. Curr Opin HIV AIDS. 2021 Sep;16(5):262.

133. Falasca K, Lanuti P, Ucciferri C, Pieragostino D, Cufaro MC, Bologna G, et al. Circulating extracellular vesicles as new inflammation marker in HIV infection. AIDS. 2021 Mar 15;35(4):595.

134. Pulliam L, Liston M, Sun B, Narvid J. Using neuronal extracellular vesicles and machine learning to predict cognitive deficits in HIV. J Neurovirol. 2020 Dec;26(6):880–7.

135. Sun B, Fernandes N, Pulliam L. Profile of neuronal exosomes in HIV cognitive impairment exposes sex differences. AIDS Lond Engl. 2019 Sep 1;33(11):1683–92.

136. Guha D, Lorenz DR, Misra V, Chettimada S, Morgello S, Gabuzda D. Proteomic analysis of cerebrospinal fluid extracellular vesicles reveals synaptic injury, inflammation, and stress response markers in HIV patients with cognitive impairment. J Neuroinflammation. 2019 Dec 5;16:254.

137. Hu G, Yao H, Chaudhuri AD, Duan M, Yelamanchili SV, Wen H, et al. Exosome-mediated shuttling of microRNA-29 regulates HIV Tat and morphine-mediated Neuronal dysfunction. Cell Death Dis. 2012 Aug;3(8):e381.

138. Hubert A, Subra C, Jenabian MA, Tremblay Labrecque PF, Tremblay C, Laffont B, et al. Elevated Abundance, Size, and MicroRNA Content of Plasma Extracellular Vesicles in Viremic HIV-1+ Patients: Correlations With Known Markers of Disease Progression. J Acquir Immune Defic Syndr 1999. 2015 Nov 1;70(3):219–27.

139. Lee JH, Wittki S, Bräu T, Dreyer FS, Krätzel K, Dindorf J, et al. HIV Nef, paxillin, and Pak1/2 regulate activation and secretion of TACE/ADAM10 proteases. Mol Cell. 2013 Feb 21;49(4):668–79.

140. Bernard MA, Zhao H, Yue SC, Anandaiah A, Koziel H, Tachado SD. Novel HIV-1 MiRNAs Stimulate TNFα Release in Human Macrophages via TLR8 Signaling Pathway. PLoS ONE. 2014 Sep 5;9(9):e106006.

141. Pérez PS, Romaniuk MA, Duette GA, Zhao Z, Huang Y, Martin-Jaular L, et al. Extracellular vesicles and chronic inflammation during HIV infection. J Extracell Vesicles. 2019 Nov 6;8(1):1687275.

142. Castro-Gonzalez S, Colomer-Lluch M, Serra-Moreno R. Barriers for HIV Cure: The Latent Reservoir. AIDS Res Hum Retroviruses. 2018 Sep;34(9):739–59.

143. Koenig S, Gendelman HE, Orenstein JM, Dal Canto MC, Pezeshkpour GH, Yungbluth M, et al. Detection of AIDS virus in macrophages in brain tissue from AIDS patients with encephalopathy. Science. 1986 Sep 5;233(4768):1089–93.

144. Coleman CM, Wu L. HIV interactions with monocytes and dendritic cells: viral latency and reservoirs. Retrovirology. 2009 Jun 1;6:51.

145. Kumar A, Abbas W, Herbein G. HIV-1 latency in monocytes/macrophages. Viruses. 2014 Apr 22;6(4):1837–60.

146. Moretti S, Virtuoso S, Sernicola L, Farcomeni S, Maggiorella MT, Borsetti A. Advances in SIV/SHIV Non-Human Primate Models of NeuroAIDS. Pathog Basel Switz. 2021 Aug 12;10(8):1018.

147. Humbert M, Rasmussen RA, Song R, Ong H, Sharma P, Chenine AL, et al. SHIV-1157i and passaged progeny viruses encoding R5 HIV-1 clade C env cause AIDS in rhesus monkeys. Retrovirology. 2008 Oct 17;5:94.

148. Zhuang K, Leda AR, Tsai L, Knight H, Harbison C, Gettie A, et al. Emergence of CD4 independence envelopes and astrocyte infection in R5 simian-human immunodeficiency virus model of encephalitis. J Virol. 2014 Aug;88(15):8407–20.

149. Buch S, Sui Y, Dhillon N, Potula R, Zien C, Pinson D, et al. Investigations on four host response factors whose expression is enhanced in X4 SHIV encephalitis. J Neuroimmunol. 2004 Dec;157(1–2):71–80.

150. Deleage C, Chan CN, Busman-Sahay K, Estes JD. Next-generation in situ hybridization approaches to define and quantify HIV and SIV reservoirs in tissue microenvironments. Retrovirology. 2018 Jan 9;15(1):4.

151. Roark RS, Li H, Williams WB, Chug H, Mason RD, Gorman J, et al. Recapitulation of HIV-1 Env-antibody coevolution in macaques leading to neutralization breadth. Science. 2021 Jan 8;371(6525):eabd2638.

152. Cenker JJ, Stultz RD, McDonald D. Brain Microglial Cells Are Highly Susceptible to HIV-1 Infection and Spread. AIDS Res Hum Retroviruses. 2017 Nov;33(11):1155–65.

153. Borrajo A, Spuch C, Penedo MA, Olivares JM, Agís-Balboa RC. Important role of microglia in HIV-1 associated neurocognitive disorders and the molecular pathways implicated in its pathogenesis. Ann Med. 2021 Dec;53(1):43–69.

154. Burdo TH. Editor's Commentary for Special Issue: "The Role of Macrophages in HIV Persistence." J Neuroimmune Pharmacol Off J Soc NeuroImmune Pharmacol. 2019 Mar;14(1):2–5.

155. Llewellyn GN, Alvarez-Carbonell D, Chateau M, Karn J, Cannon PM. HIV-1 infection of microglial cells in a reconstituted humanized mouse model and identification of compounds that selectively reverse HIV latency. J Neurovirol. 2018 Apr;24(2):192–203.

156. Zhang YL, Ouyang YB, Liu LG, Chen DX. Blood-brain barrier and neuro-AIDS. Eur Rev Med Pharmacol Sci. 2015 Dec;19(24):4927–39.

157. Gisslén M, Price RW, Nilsson S. The definition of HIV-associated neurocognitive disorders: are we overestimating the real prevalence? BMC Infect Dis. 2011 Dec 28;11:356.

158. Bhaskaran K, Mussini C, Antinori A, Walker AS, Dorrucci M, Sabin C, et al. Changes in the incidence and predictors of human immunodeficiency virus-associated dementia in the era of highly active antiretroviral therapy. Ann Neurol. 2008 Feb;63(2):213–21.

159. Finzi D, Hermankova M, Pierson T, Carruth LM, Buck C, Chaisson RE, et al. Identification of a reservoir for HIV-1 in patients on highly active antiretroviral therapy. Science. 1997 Nov 14;278(5341):1295–300.

160. Finzi A, Pacheco B, Xiang SH, Pancera M, Herschhorn A, Wang L, et al. Lineage-specific differences between human and simian immunodeficiency virus regulation of gp120 trimer association and CD4 binding. J Virol. 2012 Sep;86(17):8974–86.

161. Shah R, Patel T, Freedman JE. Circulating Extracellular Vesicles in Human Disease. N Engl J Med. 2018 Sep 6;379(10):958–66.

162. Cano A, Ettcheto M, Bernuz M, Puerta R, Esteban de Antonio E, Sánchez-López E, et al. Extracellular vesicles, the emerging mirrors of brain physiopathology. Int J Biol Sci. 2023 Jan 1;19(3):721–43.

163. Guedes VA, Mithani S, Williams C, Sass D, Smith EG, Vorn R, et al. Extracellular Vesicle Levels of Nervous System Injury Biomarkers in Critically Ill Trauma Patients with and without Traumatic Brain Injury. Neurotrauma Rep. 2022 Dec 19;3(1):545–53.

164. Puffer RC, Cumba Garcia LM, Himes BT, Jung MY, Meyer FB, Okonkwo DO, et al. Plasma extracellular vesicles as a source of biomarkers in traumatic brain injury. J Neurosurg. 2020 Jul 24;134(6):1921–8.

165. McNamara RP, Dittmer DP. Extracellular Vesicles in Virus Infection and Pathogenesis. Curr Opin Virol. 2020 Oct;44:129–38.

166. Welsh JA, Van Der Pol E, Arkesteijn GJA, Bremer M, Brisson A, Coumans F, et al. MIFlowCyt-EV: a framework for standardized reporting of extracellular vesicle flow cytometry experiments. J Extracell Vesicles. 9(1):1713526.

167. Welsh JA, Arkesteijn GJA, Bremer M, Cimorelli M, Dignat-George F, Giebel B, et al. A compendium of single extracellular vesicle flow cytometry. J Extracell Vesicles. 2023 Feb;12(2):e12299.

168. Tian Y, Gong M, Hu Y, Liu H, Zhang W, Zhang M, et al. Quality and efficiency assessment of six extracellular vesicle isolation methods by nano-flow cytometry. J Extracell Vesicles. 2020 Jan 1;9(1):1697028.

169. GraphPad Prism 10 Statistics Guide - Choosing a normality test [Internet]. [cited 2024 May 3]. Available from: https://www.graphpad.com/guides/prism/latest/statistics/stat_choosing_a_normality_test.htm

170. Théry C, Witwer KW, Aikawa E, Alcaraz MJ, Anderson JD, Andriantsitohaina R, et al. Minimal information for studies of extracellular vesicles 2018 (MISEV2018): a position statement of the International Society for Extracellular Vesicles and update of the MISEV2014 guidelines. J Extracell Vesicles. 2018 Nov 23;7(1):1535750.

171. Marchisio M, Simeone P, Bologna G, Ercolino E, Pierdomenico L, Pieragostino D, et al. Flow Cytometry Analysis of Circulating Extracellular Vesicle Subtypes from Fresh Peripheral Blood Samples. Int J Mol Sci. 2020 Dec 23;22(1):48.

172. Pulliam L, Sun B, McCafferty E, Soper SA, Witek MA, Hu M, et al. Microfluidic Isolation of Neuronal-Enriched Extracellular Vesicles Shows Distinct and Common Neurological Proteins in Long COVID, HIV Infection and Alzheimer's Disease. Int J Mol Sci. 2024 Mar 29;25(7):3830.

173. Roseborough AD, Myers SJ, Khazaee R, Zhu Y, Zhao L, Iorio E, et al. Plasma derived extracellular vesicle biomarkers of microglia activation in an experimental stroke model. J Neuroinflammation. 2023 Jan 31;20(1):20.

174. Brennan K, Martin K, FitzGerald SP, O'Sullivan J, Wu Y, Blanco A, et al. A comparison of methods for the isolation and separation of extracellular vesicles from protein and lipid particles in human serum. Sci Rep. 2020 Jan 23;10(1):1039.

175. Giovanazzi A, van Herwijnen MJC, Kleinjan M, van der Meulen GN, Wauben MHM. Surface protein profiling of milk and serum extracellular vesicles unveils body fluid-specific signatures. Sci Rep. 2023 May 30;13:8758.

176. Okada-Tsuchioka M, Kajitani N, Omori W, Kurashige T, Boku S, Takebayashi M. Tetraspanin heterogeneity of small extracellular vesicles in human biofluids and brain tissue. Biochem Biophys Res Commun. 2022 Oct 30;627:146–51.

177. Sódar BW, Kittel Á, Pálóczi K, Vukman KV, Osteikoetxea X, Szabó-Taylor K, et al. Low-density lipoprotein mimics blood plasma-derived exosomes and microvesicles during isolation and detection. Sci Rep. 2016 Apr 18;6(1):24316.

178. Stam J, Bartel S, Bischoff R, Wolters JC. Isolation of extracellular vesicles with combined enrichment methods. J Chromatogr B. 2021 Apr 15;1169:122604.

179. Hatton IA, Galbraith ED, Merleau NSC, Miettinen TP, Smith BM, Shander JA. The human cell count and size distribution. Proc Natl Acad Sci U S A [Internet]. 2023 Sep 9 [cited 2024 Jan 17];120(39). Available from: https://www.ncbi.nlm.nih.gov/pmc/articles/PMC10523466/

180. Stoner SA, Duggan E, Condello D, Guerrero A, Turk JR, Narayanan PK, et al. High sensitivity flow cytometry of membrane vesicles. Cytometry A. 2016;89(2):196–206.

181. Welsh JA, Holloway JA, Wilkinson JS, Englyst NA. Extracellular Vesicle Flow Cytometry Analysis and Standardization. Front Cell Dev Biol. 2017 Aug 30;5:78.

182. Kuiper M, van de Nes A, Nieuwland R, Varga Z, van der Pol E. Reliable measurements of extracellular vesicles by clinical flow cytometry. Am J Reprod Immunol. 2021 Feb;85(2):e13350.

183. Giebel B, Helmbrecht C. Methods to Analyze EVs. In: Hill AF, editor. Exosomes and Microvesicles: Methods and Protocols [Internet]. New York, NY: Springer; 2017 [cited 2024 Jan 17]. p. 1–20. (Methods in Molecular Biology). Available from: https://doi.org/10.1007/978-1-4939-6728-5_1

184. Morales-Kastresana A, Jones JC. Flow Cytometric Analysis of Extracellular Vesicles. Methods Mol Biol Clifton NJ. 2017;1545:215–25.

185. Mizenko RR, Brostoff T, Rojalin T, Koster HJ, Swindell HS, Leiserowitz GS, et al. Tetraspanins are unevenly distributed across single extracellular vesicles and bias sensitivity to multiplexed cancer biomarkers. J Nanobiotechnology. 2021 Aug 21;19(1):250.

186. Karimi N, Dalirfardouei R, Dias T, Lötvall J, Lässer C. Tetraspanins distinguish separate extracellular vesicle subpopulations in human serum and plasma – Contributions of platelet extracellular vesicles in plasma samples. J Extracell Vesicles. 2022 May;11(5):e12213.

187. Mondal A, Bose D, Saha P, Sarkar S, Seth R, Kimono D, et al. Lipocalin 2 induces neuroinflammation and blood-brain barrier dysfunction through liver-brain axis in murine model of nonalcoholic steatohepatitis. J Neuroinflammation. 2020 Jul 4;17(1):201.

188. Kim JH, Kang RJ, Hyeon SJ, Ryu H, Joo H, Bu Y, et al. Lipocalin-2 Is a Key Regulator of Neuroinflammation in Secondary Traumatic and Ischemic Brain Injury. Neurother J Am Soc Exp Neurother. 2023 Apr;20(3):803–21.

189. Ojeda-Juárez D, Shah R, Fields JA, Harahap-Carrillo I, Koury J, Maung R, et al. Lipocalin-2 Mediates HIV-1 Induced Neuronal Injury and Behavioral Deficits by Overriding CCR5-dependent Protection. Brain Behav Immun. 2020 Oct;89:184–99.

190. Sims B, Farrow AL, Williams SD, Bansal A, Krendelchtchikov A, Gu L, et al. Role of TIM-4 in exosome-dependent entry of HIV-1 into human immune cells. Int J Nanomedicine. 2017 Jul 6;12:4823–33.

191. Suh HS, Lo Y, Choi N, Letendre S, Lee SC. Insulin-like growth factors and related proteins in plasma and cerebrospinal fluids of HIV-positive individuals. J Neuroinflammation. 2015 Apr 15;12(1):72.

192. Mynarcik DC, Frost RA, Lang CH, DeCristofaro K, McNurlan MA, Garlick PJ, et al. Insulin-like growth factor system in patients with HIV infection: Effect of exogenous growth hormone administration. J Acquir Immune Defic Syndr Hum Retrovirol. 1999 Sep 1;22(1):49–55.

193. Baer SL, Colombo RE, Johnson MH, Wakade S, Pacholczyk G, Newman-Whitlow C, et al. Indoleamine 2,3 dioxygenase, age, and immune activation in people living with HIV. J Investig Med Off Publ Am Fed Clin Res. 2021 Aug;69(6):1238–44.

194. Potula R, Poluektova L, Knipe B, Chrastil J, Heilman D, Dou H, et al. Inhibition of indoleamine 2,3-dioxygenase (IDO) enhances elimination of virus-infected

macrophages in an animal model of HIV-1 encephalitis. Blood. 2005 Oct 1;106(7):2382–90.

195. Chen J, Xun J, Yang J, Ji Y, Liu L, Qi T, et al. Plasma Indoleamine 2,3-Dioxygenase Activity Is Associated With the Size of the Human Immunodeficiency Virus Reservoir in Patients Receiving Antiretroviral Therapy. Clin Infect Dis. 2019 Apr 8;68(8):1274–81.

196. Fennessey CM, Pinkevych M, Immonen TT, Reynaldi A, Venturi V, Nadella P, et al. Genetically-barcoded SIV facilitates enumeration of rebound variants and estimation of reactivation rates in nonhuman primates following interruption of suppressive antiretroviral therapy. PLoS Pathog [Internet]. 2017 May [cited 2024 May 3];13(5). Available from: https://www.ncbi.nlm.nih.gov/pmc/articles/PMC5433785/

197. Vödrös D, Fenyö EM. Quantitative Evaluation of HIV and SIV Co-Receptor Use With GHOST(3) Cell Assay. In: Zhu T, editor. Human Retrovirus Protocols: Virology and Molecular Biology [Internet]. Totowa, NJ: Humana Press; 2005 [cited 2024 May 4]. p. 333–42. Available from: https://doi.org/10.1385/1-59259-907-9:333

198. Royo F, Théry C, Falcón-Pérez JM, Nieuwland R, Witwer KW. Methods for Separation and Characterization of Extracellular Vesicles: Results of a Worldwide Survey Performed by the ISEV Rigor and Standardization Subcommittee. Cells. 2020 Aug 25;9(9):1955.

199. Zougman A, Selby PJ, Banks RE. Suspension trapping (STrap) sample preparation method for bottom-up proteomics analysis. Proteomics. 2014 May;14(9):1006–1000.

200. Tyanova S, Temu T, Cox J. The MaxQuant computational platform for mass spectrometry-based shotgun proteomics. Nat Protoc. 2016 Dec;11(12):2301–19.

201. Bielow C, Mastrobuoni G, Kempa S. Proteomics Quality Control: Quality Control Software for MaxQuant Results. J Proteome Res. 2016 Mar 4;15(3):777–87.

202. Bruderer R, Bernhardt OM, Gandhi T, Miladinović SM, Cheng LY, Messner S, et al. Extending the limits of quantitative proteome profiling with data-independent acquisition and application to acetaminophen-treated three-dimensional liver microtissues. Mol Cell Proteomics MCP. 2015 May;14(5):1400–10.

203. Menzyanova NG, Pyatina SA, Shabanov AV, Nemtsev IV, Stolyarov DP, Dryganov DB, et al. The Morphology and Phenotype of Monocyte-Macrophages When Cultured on Bionanofilms Substrates with Different Surface Relief Profiles. Biomolecules. 2020 Jan;10(1):65.

204. Lee HS, Stachelek SJ, Tomczyk N, Finley MJ, Composto RJ, Eckmann DM. Correlating macrophage morphology and cytokine production resulting from biomaterial contact. J Biomed Mater Res A. 2013 Jan;101(1):203–12.

205. Vlach J, Saad JS. HIV: a vicTIM. Trends Microbiol. 2014 Nov 1;22(11):603–4.

206. Wang Z, Chen C, Su Y, Ke N. Function and characteristics of TIM-4 in immune regulation and disease (Review). Int J Mol Med. 2023 Feb 1;51(2):1–16.

207. Sun B, Dalvi P, Abadjian L, Tang N, Pulliam L. Blood neuron-derived exosomes as biomarkers of cognitive impairment in HIV. AIDS Lond Engl. 2017 Sep 10;31(14):F9–17.

208. Favre D, Mold J, Hunt PW, Kanwar B, Loke P, Seu L, et al. Tryptophan Catabolism by Indoleamine 2,3-Dioxygenase 1 Alters the Balance of TH17 to Regulatory T Cells in HIV Disease. Sci Transl Med. 2010 May 19;2(32):32ra36.

209. Li S, Wu Y, Keating SM, Du H, Sammet CL, Zadikoff C, et al. Matrix metalloproteinase levels in early HIV infection and relation to in vivo brain status. J Neurovirol. 2013 Oct;19(5):10.1007/s13365-013-0197–3.

210. Evans DJ. Viral Receptors. In: Mahy BWJ, Van Regenmortel MHV, editors. Encyclopedia of Virology (Third Edition) [Internet]. Oxford: Academic Press; 2008 [cited 2024 May 7]. p. 319–24. Available from: https://www.sciencedirect.com/science/article/pii/B9780123744104005318

211. Yang X, Chatterjee V, Zheng E, Reynolds A, Ma Y, Villalba N, et al. Burn Injury-Induced Extracellular Vesicle Production and Characteristics. Shock Augusta Ga. 2022 Jun 1;57(6):228–42.

212. Debbi L, Guo S, Safina D, Levenberg S. Boosting extracellular vesicle secretion. Biotechnol Adv. 2022 Oct;59:107983.

213. Moulin C, Crupi MJF, Ilkow CS, Bell JC, Boulton S. Extracellular Vesicles and Viruses: Two Intertwined Entities. Int J Mol Sci. 2023 Jan 5;24(2):1036.

214. Mazzucco M, Mannheim W, Shetty SV, Linden JR. CNS endothelial derived extracellular vesicles are biomarkers of active disease in multiple sclerosis. Fluids Barriers CNS. 2022 Feb 8;19(1):13.

215. Longobardi A, Nicsanu R, Bellini S, Squitti R, Catania M, Tiraboschi P, et al. Cerebrospinal Fluid EV Concentration and Size Are Altered in Alzheimer's Disease and Dementia with Lewy Bodies. Cells. 2022 Jan 28;11(3):462.

216. Kupcova Skalnikova H, Bohuslavova B, Turnovcova K, Juhasova J, Juhas S, Rodinova M, et al. Isolation and Characterization of Small Extracellular Vesicles from Porcine Blood Plasma, Cerebrospinal Fluid, and Seminal Plasma. Proteomes. 2019 Jun;7(2):17.

217. Sandau US, Magaña SM, Costa J, Nolan JP, Ikezu T, Vella LJ, et al. Recommendations for reproducibility of cerebrospinal fluid extracellular vesicle studies. J Extracell Vesicles. 2024;13(1):12397.

218. Lanman T, Letendre S, Ma Q, Bang A, Ellis R. CNS Neurotoxicity of Antiretrovirals. J Neuroimmune Pharmacol Off J Soc NeuroImmune Pharmacol. 2021 Mar;16(1):130–43.